Computational Analysis of the Impact of Urbanization on the Local Climate of Shanghai

LUCEN LI, BEng.

Thesis submitted to the University of Nottingham for the degree of Doctor of Philosophy
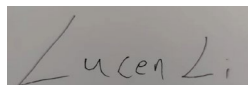
DECEMBER 2021

AUTHOR'S DECLARATION

I hereby declare that I am the sole author of this thesis and have performed all of the work presented herein. I also declare that this work has not been submitted in any form for another degree at any other university or institution of tertiary education.

All information derived from published or unpublished works of others have been duly acknowledged in the text and provided in the list of references.

Lucen Li

Signature   Date: 20 December 2021

Abstract

Urbanization brings physical changes to land surfaces of Shanghai and consequently impacts its local climate. Studies of urbanization effect on urban climate for Shanghai area using numerical modelling is insufficient. The purpose of this research is to narrow the gap by coupling the Weather Research and Forecasting model with the NOAH land surface model and the Urban Canopy Model - WRF/NOAH/UCM to examine the urban climatology of Shanghai since 21st century.

The model is first validated against a network of meteorological observations in the region to determine its suitability for urban climate investigations. Climatological variables (near-surface temperature, relative humidity, and wind speed) along with land use and land cover changes, planetary boundary layer height, and urban heat island intensity of the area are also investigated. The model evaluation shows good performance over the region. Land use and land cover change demonstrates strong influence in thermal climatology variations.

The results shows that the average heat island intensity in Shanghai increased by 1.08°C from 2000 to 2017, with the highest heat island intensity reaching 3.41°C. Torrid area (Thermohydrometric Index > 30) also improved by 11%. Other climatological variables varied accordingly with the urbanization processes.

The simulation of climate prediction for Shanghai in 2030 shows that the development under representative concentration pathway 8.5 will face the worst thermal condition, and the intensity of heat island effect will be further increased by about 2°C compared with the current situation. Among them, 63% and 37% are from the background of global warming and urbanization, respectively.

List of publications

Numerical study of urbanization in Shanghai and its impact on local climate, still in progress of manuscript writing

Projection of urban climate in the 2030s of Shanghai under different scenarios and development pathways, still in progress of manuscript writing

Acknowledgment

List of Figures

List of Tables

Contents

List of Abbreviations

The following table describes the significance of various abbreviations and acronyms used throughout the these.

Abbreviations	Meaning
AH	Anthropogenic heat
ARW	Advanced Research WRF
ETI	Effective temperature index
FNL	NCEP Final operational global analysis and forecast data
HIR	High intensity residential area
GDAS	Global Data Assimilation System
GFS	Global Forecast System
GIS	Geographic Information System
GRIB	General regularly-distributed information in binary form
GTS	Global Telecommunications System
IOA	Index of agreement
IPCC	Intergovernmental Panel for Climate Change
IPCC AR5	The fifth assessment report of the IPCC
LH	Latent heat flux
LIR	Low intensity residential area
LULC	Land use and land cover
MODIS	Moderate-Resolution Imaging Spectroradiometer
MAE	Mean absolute error
MBE	Mean bias error

Abbreviations	Meaning
NCAR	National Center for Atmospheric Research
NCEP	National Centers for Environmental Prediction
NCL	NCAR Command Language
Ncview	a visual browser for netCDF format files
NetCDF	Network Common Data Form
NMM	Non-hydrostatic Mesoscale Model
Noah LSM	The Noah Land Surface Model
PBL	Planet Boundary Layer
PBLH	Planetary Boundary Layer Height
R^2	Coefficient of determination
RCP	Representative Concentration Pathway
RH	Relative Humidity
RMSE	Root Mean Square Error
RSI	Relative Strain Index
SH	Sensible heat flux
T2m	2-m Temperature
THI	Temperature Humidity Index
UHII	Urban Heat Island Intensity
UCM	Urban Canopy Model
USGS	United States Geological Survey
WPS	WRF Pre-processing System
WRF	Weather Research and Forecasting
WS10m	10-m wind speed

1 Introduction

1.1 Background

Since the late 1970s, global climate change has undoubtedly been an environmental issue of great concern at home and abroad. The Intergovernmental Panel for Climate Change (IPCC) has conducted five assessments of the science, impacts, adaptation, and mitigation of global climate change, all of which have shown very clearly that human activities have a significant impact on global warming (IPCC, 2013). The fifth assessment report of the IPCC (IPCC AR5) has found clear evidence for the direct and indirect impact of anthropogenic activities on the climate system. As an important member of the climate system, human beings are influenced by various natural processes in the climate system on the one hand. On the other hand, with the progress of human society and economic development, the impact of human activities on climate change is becoming more and more significant. In the IPCC AR5, it was clearly stated that global warming due to human activities is continuing to increase and that there is a high degree of certainty (over 95% probability of occurrence) that human activities have contributed to climate change over the last 50 years, with global warming as the main feature (IPCC, 2019; Brasseur et al., 2012).

There are three main ways in which human activity influence the climate. Firstly, the burning of fossil fuels from industrial production and greenhouse gases emission from agricultural activities, increases the atmospheric concentration of carbon dioxide and other greenhouse gases. Secondly, the smoke and industrial dust produced by human activities lead to changes in the concentration of aerosol particles in the atmosphere. Finally, human social and economic development and progress inevitably bring about changes in land use patterns and the nature of the subsurface (Brasseur et

al., 2012). All these activities directly or indirectly influence the Earth's radiation balance, and the climate system responds directly to the changes in the radiation balance, while amplifying or reducing them through feedback mechanisms (Li et al., 2010).

The main impact of land use and land cover on climate change is that underlying surface directly cause the change of land surface physical characteristics, altering the surface albedo and the exchange of energy and materials between the land surface and the atmosphere, affecting the energy balance of the land surface and thus the regional climate characteristics. Besides, changes in vegetation type, density and soil characteristics also change the climate through other mechanisms. For instance, the terrestrial carbon storage and fluxes, which in turn cause changes in atmospheric greenhouse gas levels (Goldewijk et al., 2001).

The rise and expansion of cities has replaced the natural surface with dense buildings and impervious surfaces. As a result, the surface roughness increases, while the surface wind speed and air humidity decrease correspondingly, thus speeding up the diameter. On the other hand, the decrease of surface albedo and the change of heat conduction and heat capacity lead to the increase of turbulence. All these alter the relative size of the heat and water budgets in the exchange of matter and energy between the surface and the atmosphere (Kalnay, 2003).

With the acceleration of urbanization, urban surface and structural layout have become more comprehensive, complex, and diversified, especially in megacities where there are many high-density living areas. This special underlying surface has a significant impact on local climate. In addition, industrial production and residential life in the city release a large amount of anthropogenic heat and exhaust gas, resulting in the city temperature being significantly higher than the surrounding suburbs: a phenomenon often referred to as the "urban heat island effect. "Urban heat island" is

one of the most typical features of urban climate. Investigation of the urban climate of large and medium-sized cities such as Beijing, Shanghai, and other coastal cities, found that both the winter and annual average temperature of urban areas is significantly higher than that of surrounding suburban and rural areas, and the intensity of the urban heat island correlates with the city scale (Peng et al., 2012).

Ever since 1978, China's urbanization process has progressed rapidly, leading to the formation of three large urban agglomerations: the Yangtze River Delta, the Pearl River Delta, and Beijing-Tianjin-Hebei region. As one of the world's six major urban agglomerations - the Yangtze River Delta region is the most representative area, with a total area of 11.31 x 10 km^2. Its population density is more than 800 people/km^2, six times the national average, and its GDP per capita is about \$4,000, which is three times the national average (National Statistics Bureau, 2020). As the economic centre of the Yangtze River Delta region, Shanghai covers an administrative area of about 6341 km^2, with a population of 24.9 million and a GDP of 387 million yuan.

With the rapid urbanization and economic development of Shanghai, its land coverage is also undergoing great changes, especially urban expansion. The high intensity human of activities aggravates the contradiction between natural environment protection and human development, also restricts the sustainable economic development of the city. Therefore, an in-depth study of the impact of Shanghai's urban expansion on its atmospheric environment and a scientific assessment of the degree of the impact is of great significance. Such study can help reduce the negative effects of urbanization, coordinate the sustainable development of human and natural environment, and ensure the sustainable development of urban society and economy.

1.2   Objectives

To computationally investigate the urban climatology of Shanghai, its urbanization, and its consequent impact on regional climate.

1. To examine the performance of Weather Research and Forecasting (WRF) model coupled with Noah land surface model and urban canopy model

2. To study the urban climate of Shanghai using WRF

3. To investigate environmental changes accompanying the Shanghai's urbanization since 21st century and its impact on local climate.

4. To study the microclimate of Shanghai and investigate the sensitivity of urban heat island and human comfort

5. To explore the future urban climate of Shanghai with different RCP scenarios under the background of continued urbanization in the future.

6. To evaluate possible ways to mitigate thermal conditions associated with urbanization of Shanghai in the future context.

1.3   Significance of the study

1. Compared with statistical data and statistical analysis at observation sites that has the inherent limitation of its discrete distribution, using WRF/UCM can reduce research costs and design ideal experiments with different parameterizations to meet more customized research needs.

2. The results of this research will help urban planners, designers, ecologists, environmental scientists, government, and non-governmental organizations to make appropriate plans, update existing guidelines and design methods to build sustainable and liveable city.

3. Knowledge of the distribution of heat island intensity in Shanghai has a

predictive effect on urban construction.

4. The results can be used as a platform for future climate simulation in Shanghai, or even other cities.

5. Although this research mainly discusses meteorological factors, spatial and temporal variations of temperature distribution, planetary boundary layer height and wind field have a huge impact on pollution dispersion. The research conclusions are able to provide a theoretical basis for the subsequent study of air pollutant distribution in Shanghai.

6. Findings of this study will help in filling the research gap about the development paths and corresponding urban climate projections of Shanghai in the future. and provides an analysis basis for policy makers in response to sustainable development and mitigation of urbanization induced problems.

1.4 Thesis Outline

This thesis is divided into seven independent yet interwoven chapters, in which the first chapter introduces the research background and objectives, followed by the second chapter summarizes the latest research progress in the current academic circle, and the third chapter introduces the research tools needed throughout the whole thesis. Chapter 4, Chapter 5 and Chapter 6 answer the research questions raised at the beginning of chapter1, with an introduction the research methodologies independently in each chapter (chapter 4 5 6). Finally, chapter 7 summarizes and reviews the whole thesis, and puts forward the prospect of future research direction (Figure 1.1).
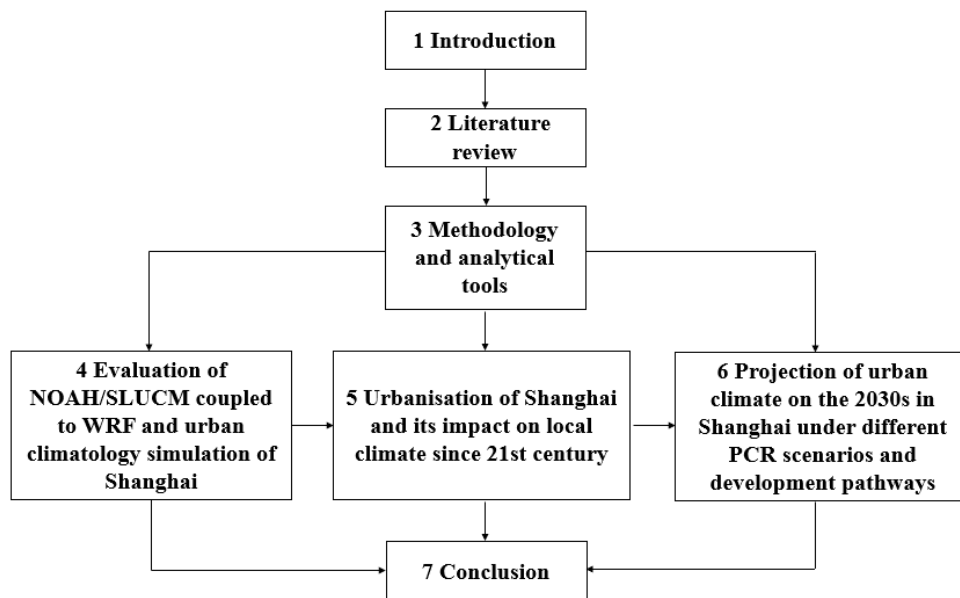
Figure 1.1 Thesis flowchart

The first two chapters introduce the background of the research and summarize relevant literature in the field. Starting from the concept of urbanization, chapter 2 reviews the urbanization world widely and the impact of urbanization on the local climate. And narrows down to the area of interests in this thesis – Shanghai.

Chapter 3 introduces the different numerical models (WRF/Noah LSM/UCM) that

are studied in combination. In addition, statistical and other tools used in this study are introduced. Chapter 3 summarizes a brief description of the research materials and input data.

In chapter 4, the setup of coupled WRF/Noah/UCM is introduced in detail, and the reliability of the coupled model after replacing the underlying surface data set and other simulation parameters is verified by comparing the experimental and observation data. Furthermore, the climate of Shanghai is analysed according to the simulation results. This chapter is concluded by summarising the different investigation conducted herein.

In chapter 5, four ideal simulation experiments are designed with 4 different urban underlying surface datasets in different year to represent the urbanization process of Shanghai. The influence of urbanization on local climate of Shanghai is comparatively analysed, and the sensitivity of heat island effect and residents' comfort to urbanization is also analysed.

Based on chapter 5, the sixth chapter simulates the urban environment of Shanghai in 2030. Different scenarios are proposed by predicting the future development of Shanghai and through two different RCP development scenarios identified by IPCC. By comparing the simulation results, the influence of urbanization and global warming on local climate in Shanghai is analysed, and effective countermeasures are proposed.

Finally, Chapter 7 concludes the different conclusions of each chapter and proposes some suggestions on possible future studies.

2 Literature review: Impact of Urbanization on Urban Climatology

To gain a comprehensive background on the impact of urbanization as well as its interaction with global-scale climate change on the urban climate, this chapter starts by reviewing the concept of urbanization and trends of urbanization in China were discussed in section 2.1. Section 2.2 discusses the impact of urbanization on urban climatology with a focus on urban heat island (UHI), anthropogenic heat flux, air quality, precipitation, and human comfort. Section 2.2.5 discusses the relationship between urban climate and global-scale climate change while section 2.2.6 presents mitigation and adaptation strategies to address the heat stress and health related impact of urbanization now and in the future. As Shanghai is the focus and study area of this Ph.D. thesis, section 2.3 discusses previous studies on the effect of urbanization of Shanghai's climate. Section 2.4 presents the challenges of observation-based approach based meteorological data for studying the impact of urbanization and discusses the advantages of numerical modelling approach not only for studying historical impacts of urbanization but also for predicting future occurrence of extreme events and providing strategies for mitigation and adaptation.

2.1 Urbanization

Urbanization is a developmental process, which is usually characterized by an increase in the built-up areas and human population and the growth of rural communities into cities and urban centres (Ren, 2015; Mark, 2014). The earliest history of urbanization could be arguably traced to the ancient Mesopotamia in the Uruk region between the period 4300 – 3100 BCE (Mark, 2014). The world has witnessed a rapid rate of urbanization over the past decades. From less than one third urban settlers in the 1950s, for the first time in 2007, the world's urban population exceeded its rural population, and has predominantly remained urban ever since (United Nations, 2014).

By 2015, an estimated 54% of the global population lived in urban cities and this number is projected to reach 60% by 2030 and 66% by 2050 (United Nations, 2014; Onyango, 2018).

Not only would the increasing trend in urbanization continue but also the number of mega-cities accommodating more than 10 million dwellers is projected to increase. For instance, in 1990, the world has only 10 mega-cities and the number significantly increased to 28 in 2014 and by 2030 the number of mega-cities accommodating more than 10 million inhabitants is projected to be 41(United Nations, 2014). Since the highest percentage of the global population is projected to live in urban cities, it is important to understand how the process of urbanization affect urban climates, and how previous and future urbanization would affect urban climate both at local and regional levels. In addition, this would provide policymakers and urban planners with invaluable information on how to plan future urbanization and urban cities to improve the quality of life of urban dwellers.

2.1.1 Urbanization in China

Although the history of China spans dynasties over a millennia, the history of modern China can be divided into the pre-reform era (1949 – 1978) and the post-reform era (1978 – date) (Farrell and Westlund, 2018). Since 1978, China has experienced a remarkable and unprecedented urbanization, which is attributed to rapid economic growth occasioned by the Chinese economic reform (Zhang and Song, 2003). A distinguishing feature of China's urbanization is in its pace and scale. From 11.8% in 1950, the level of urbanization in China dramatically increased to a staggering 49.2% in 2010, which corresponds to addition of over 605 million urban dwellers. This number is projected to reach 75.8% by 2050, corresponding to an addition of 380 million urban

inhabitants compared to the 2010 level (United Nations, 2014). It is noteworthy to state that, in China, the process of land urbanization has been faster than population urbanization, leading to rapid urban spatial expansion (Yao and Zhen, 2012). This provides an indication of the rapid impact of urbanization on change of land-use structures. Although there is spatial rate of urbanization and differences in land-use structure across China, it was demonstrated that, at national level, residential and industrial land accounted for the highest proportion of urban land use followed by public facilities and roads. However, in large-scale urban cities, the proportion of industrial land exceeds that of residential land and the land-use for roads and squares surpassed the proportion of green lands (Lin et al., 2015). This goes to indicate that industrialization, real estate development and traffic construction are main drivers of land urbanization process in China. This is relevant to this study as the type of land use/land cover (LULC) changes significantly contribute to the impact of urbanization on the urban climate.

Based on the statistics from the United Nations data booklet (United Nations, 2019), as of 2018, China alone accounts for six of the world's thirty-three mega-cities (cities with a population of ten million above) and has ten large cities with a population between five to ten million. Of all the cities in China, Shanghai, according to the recently concluded 2021 census (Xinhua, 2021), is the most populated urban city with a population of more than 24.87 million, of which 89.3% live in the urban area. Over the past two decades, Shanghai has witnessed a rapid economic growth and an unrivalled degree of urbanization, since the decision of the Chinese authorities to transform Shanghai into a global centre for finance, trade, and economy (J. Li et al., 2013). The rapid pace and scale of the urbanization intensity and spatial spread of Shanghai makes it an ideal case-study for examining the impact of urbanization on

urban climate.

2.2 Effect of Urbanization on Urban Climatology

Global environmental and climate change is mostly driven by the rapid growth in human population and the disproportionate share of resources consumed by urban residents (Grimmond, 2007). The key focus here is not on global-scale climate but the impact of urban cities on local and regional-scale climate. It is obvious that the surface climate within an urban city is different from that of surrounding suburban and rural areas (Oke, 1981). This unique climate of urban cities is referred to as urban climate and is distinguished by relatively higher surface air temperatures, and lower relative humidity and wind speed compared to surrounding suburbs (Oke, 1981).

Urbanization is the most obvious case of the land-use change and modification of the earth's environment. This modification significantly changes the physical, thermal, radiative, and aerodynamic properties of earth's surfaces, leading to alteration of the surface climate of urban areas (Oke, 1981; Ren, 2015). The ensued change from the modification of urban surfaces is central to the formation and evolution of urban climate. These changes are associated with the construction and functioning of cities. The introduction of new materials for infrastructure construction coupled with changes to surface morphology and anthropogenic heating, significantly modify the exchange of water and energy and airflow between the surface and atmosphere (Du et al., 2016), leading to the modification of urban climate.

At local and regional levels, the changes in urban form and cities affect urban air quality, water quality, wind and precipitation, urban heat island, urban boundary layer, and thermal heat budget (Han et al., 2014; J. Wang et al., 2008; K. Zhang et al., 2010; Cui and Shi, 2012). These effects are discussed in detail in the following subsections.

2.2.1 Urban Heat Island

Urban cities tend to have higher air and surface temperatures compared to surrounding rural areas. This phenomenon is known as the urban heat island. It is perhaps the most indicative factor of how urbanization and LULC change affect local and regional climate. A link has been established between UHI and temperature extreme heat-waves, leading to increased heat stress and mortality in urban areas (Johnson et al., 2005; Koomen and Diogo, 2017). The degree of urban warming occasioned by surface modification varies spatially with space and time and can range from $1 - 3°C$, but given the appropriate meteorological conditions (under calm and cloudless), urban air can be up to 10°C warmer than surrounding rural areas (Oke, 1981). The total heat generated and retained in an urban area is given by the surface energy balance equation (Oke, 1981; K. Zhang et al., 2010).

$$Q^* + Q_F = Q_H + Q_E + \Delta Q_S + \Delta Q_A \dots\dots\dots\dots\dots. (1)$$

Where Q* represents the net surface radiation, Q_F is the anthropogenic heat, Q_H stands for turbulent sensible heat flux, Q_E represents the latent heat flux, while $\Box Q_S$ and $\Box Q_A$ stand for sensible heat storage and net heat advection, respectively.

Grimmond (2007) has outlined to the underlying causes of UHI to include increased urban surface area (leading to increase in shortwave radiation absorption, reduced wind speed, and decreased heat transport); surface materials (thermal properties: higher heat capacity, surface heat storage, and conductivity); moisture characteristics (resulting in decreased latent heat flux, large impervious surface areas, increased surface run-off); anthropogenic heating (heating and cooling, fuel combustion for transportation and

industrial activities); and air pollution (due to emission of pollutants and dust resulting to greenhouse effect). The difference in the water permeability and thermal properties of urban and rural surfaces is one of the major drivers of UHI. Urban surfaces have higher absorption rate for solar radiation, they are composed of materials with high heat capacity and conductivity and can more amount of heat compared to suburban and rural surfaces (Jin et al., 2011). In addition, the morphology of a city (in terms of sky view factor, and buildings' height and density) affects its cooling rate by increasing the reflection of long-wave between walls, rising the absorption and retention of solar radiation during the day, and decreasing the wind speed and airflow at street level (Grimmond, 2007; Kalnay and Cai, 2003). Other factors include meteorological conditions, anthropogenic heating, land cover type, and urban morphology (Du et al., 2016; Grimmond, 2007).

A correlation between urbanization and UHI has been established for many cities and regions around the world. (Du et al., 2016) studied the impact of various factors including urban area on surface UHI in the Yangtze River Delta Urban Agglomeration using remote sensing, statistical, and meteorological data. Results indicated that surface UHI intensity varies temporally with the time of the day and the season of the year. The highest UHI intensity was observed in the summer (0.84°C) followed by autumn (0.81°C) then spring (0.78°C) with the less intensity observed in winter (0.53°C). In addition, it was observed that UHI is higher during the daytime (0.98°C) compared to night-time (0.50°C). Using the meteorological data of Shanghai from 1978 to 2007, (K. Zhang et al., 2010) observed that an annual increase in UHI compared to suburban and rural areas, which correlates with increase in urban densities over the observed period. An increase in mean temperature rate of 0.75°C per decade was observed, and the variability of the UHI intensity was highest in autumn and weakest in the winter, with

night-time UHI being higher than daytime UHI. Similar variations were observed with expanding urban areas in Beijing from 1989 to 2000, with more compacted urban areas displaying higher UHI intensities, which was attributed to rapid transition from suburban lands to urban lands (Qiao et al., 2014). In another study, (Bian et al., 2017) examined the effect of urbanization on the UHI of Shijiazhuang using meteorological data for 1965 – 2012. A significant warming of the urban boundary later of up to 0.23°C per decade was observed and the observed UHI for spring and autumn were more significant than the other seasons. Survey of temperatures in London reveals that the UHI is more intense in the city centre, during night-time, under stable weather conditions in the summer (Wilby, 2003). This effect was observed to reduce with distance from the city centre under windier conditions during the daytime. It was also noted that dense urban structures obstruct airflow and tend to reduce wind speed while reducing the overall convective heat losses from buildings (Wilby, 2003).

González-Aparicio (2014) simulated and studied the effect of urbanization of Bilbao on the atmospheric boundary layer. They demonstrated a direct correlation between city expansion and UHI intensity. Compared to the baseline case, an UHI intensity of 2.2°C and 3°C were observed when the city doubled and trebled in size, respectively. Using ensemble numerical study approach, Li (2016) studied the impact of various urbanization patterns on the local climate of Singapore, specifically the canopy layer UHI intensity. Their results indicated that the pattern of urbanization has little impact on UHI intensity, with the impact of asymmetric urbanization pattern being mildly than that of symmetric urbanization due to closely linked urban area distribution in the former. Adachi (2012) estimated the impact of urbanization over a period of 70 years on the summertime local climate of Tokyo metropolitan area. They predicted a rise in the surface air temperature of 0.5°C and an average of UHI intensity of 1.5°C.

Overall, the above studies have demonstrated that direct correlation between the process of urbanization and increasing UHI intensity, with the type of land cover change, urban morphology, and urban area density being critical factors that impact the intensity of UHI. Variation in anthropogenic heat flux in urban area is another factor of significant importance that influence UHI.

2.2.1.1 Anthropogenic heating

Anthropogenic heating resulting from human activities is another significant factor that contributes to the UHI effect experienced by urban areas. The main sources of anthropogenic heating release include buildings, transportation, and industries (Shahmohamadi et al., 2011; Sailor, 2011). It should be noted that anthropogenic heat release is often accompanied by moisture release, which affects the urban long-wave radiation budget (Sailor, 2011). Anthropogenic heating can raise the urban air temperature by as much as 1°C in summer and 3°C in the winter (Sailor, 2011). Other studies suggest that it can raise the urban heat island temperature by as much as 4°C and contribute to increasing heat stress on urban residents (Chapmanet al., 2016). The impact of anthropogenic heat emission on urban thermal environment is more pronounced in the densest part of the city and in winter when shortwave radiation is weak and the reverse is the case for winter (Ichinose et al., 1999; Chapmanet al., 2016).

As such, anthropogenic heat emission should be considered and incorporated into urban climate models (Bian et al., 2017; Chapman et al., 2016). In most modelling studies, anthropogenic heat values are used as default, constant values, or adjusted based upon urban scenario and climate (Chapman et al., 2017). However, considering the role of anthropogenic heating to UHI intensity, it is important to estimate the anthropogenic heat flux, especially for simulation studies on the impact of future

urbanization on urban areas. The techniques used to estimate anthropogenic heat release are based on urban energy budget, urban growth, or building energy models (Adachi et al., 2012; Hamdi et al., 2014; Sailor, 2011). Chapman, Watson, and McAlpine (2016) used the population census data, the inventory of hourly traffic volume, and the electricity and gas consumption data of buildings to estimate the anthropogenic heat emission and its ensuing effect on the urban heat island of four Australian cities.

Although anthropogenic heat flux was demonstrated to have significant effect on UHI intensity, its effect is not as significant as city expansion (González-Aparicio et al., 2014). They found that doubling the anthropogenic heat flux has similar effect on the UHI as doubling the city size but over different urban areas (270 km^2 for doubled anthropogenic heating vs 550 km^2 doubled urban area). X. Li (2016) indicated that for the same urbanization pattern of Singapore, the amount of anthropogenic heat released into the urban area has significant impact on the UHI intensity, with its impact being more obvious during the night-time than the daytime.

In another work, Bohnenstengel (2014) studied the impact of anthropogenic heat flux on the urban heat island of London, in spring and winter, by estimating the varying anthropogenic heat fluxes based on the energy-demand data of London. Their results indicated that including the anthropogenic heat emission significantly improves the simulation of the screen-level temperatures and that its impact is more prominent in winter compared to spring. This is because, in winter, anthropogenic heat emission accounts for a large percentage of the urban heat and the boundary layer is shallower, while during spring, the share of anthropogenic heat emission is small relative to the incoming solar energy. This agrees with the observations of Ichinose et al, 1999. Omitting the contribution of anthropogenic heating risk underestimating the impact of urban heat island on temperature (Chapman et al., 2016) and missing opportunities in

addressing the impact of rising urban temperatures and associated risks of heat stress.

2.2.2 Urbanization and Ambient Air Quality

The atmospheric air in urban cities is known to contain high levels of air pollutants mostly anthropogenic by source. Urban air pollution is mostly caused by transportation, and industrial and building energy consumption. Rapid urbanization, increasing population and industrialization are main drivers and contributors to air pollution (Tecer and Tagil, 2014). As highlighted earlier in section 2.2 changes in urban form and urban surfaces, which are driven by urbanization, have a significant effect on the meteorological conditions of urban cities. Variation in the meteorological conditions due to urbanization has a direct impact on the atmospheric concentration of pollutants including oxides of nitrogen (NOx), ozone (O_3), aerosols, and particulate matter (Y. Li et al., 2019). It a well-known fact that air pollution has adverse effect on human health causing respiratory diseases and, in some cases, leading to increased hospitalization and mortality. The World Health Organization's report on the global assessment of exposure and burden of diseases estimates that three million people died from exposure to ambient air population in 2012 alone (World Health Organization, 2016). As such, understanding the relationship between urbanization and air quality is relevant to effective planning, long term sustainability of urban cities, and protecting the health and wellbeing of urban dwellers.

Several studies have investigated the impact of urbanization on urban air quality. The relationship between urbanization and air quality exists mainly due to increase in human population and associated social and economic activities, which leads to higher demand for fossil-based energy and emission of pollutants (S. Wang et al., 2020). The effect of megacities on urban agglomerations could basically from the concept of 'urban

metabolism' (Baklanov et al., 2016), where urban cities consume huge amount of material resources and energy and excrete products while at the same time emitting gaseous pollutants, particulate matter, and aerosols into the atmosphere. The local effect of such emissions is evident within the boundaries of megacities, even though it can be transported over long distances and contribute to hemispheric background pollution (Baklanov et al., 2016).

Given the health impact of particulate matter (PM2.5), it is considered one of the air pollutants of concern in urban cities (S. Wang et al., 2020). The increased demand for energy for socioeconomic activities in urban cities is considered one of the main reasons that aggravated the regional atmospheric concentration of PM2.5 (Zhou et al., 2018). Han (2014) established a close link between the main indicators of urbanization (population, industrialization) with the atmospheric concentration of PM2.5, with the concentration in 85 urban cities in China being higher than those of surrounding areas. S. Wang (2020) constructed an urbanization index system which combined the social, demographic, economic and spatial components of urbanization to study the heterogeneity effect of urbanization on the atmospheric concentration of PM2.5 of 190 countries between the period 1998 to 2014. Their results should a strong correlation between level of urbanization and economic activities in middle-high income countries with elevated atmospheric concentration of PM2.5. A study by (Fang et al., 2015) which investigated the impact of urbanization on air quality index in 289 Chinese and showed that the population and vehicle density, urbanization rate, and the number of secondary industries in a city significantly impact spatially affect air quality. Shen (2021) used the 2020 covid-19 lockdown in China as a metric for evaluating the impact of urbanization on the air quality in Yangtze River Delta. Results from satellite and ground-based data showed a significant reduction in the surface concentration of particulate matter (PM10

and PM2.5), NO_2, SO_2, and CO in major cities, while the level of ozone (O_3) increases in the same period.

A host of urban activities such as transportation and industrial production generates aerosols and other gaseous pollutants whose concentration is higher in urban areas compared to rural areas (Pataki et al., 2007). Aerosol's impact regional climate through the scattering, reflection, or adsorption of solar radiation. The resulting effect of aerosols on the climate (either cooling or warming) depends on the type of aerosol: sulphate-based aerosols produced a cooling effect whereas the carbon-based generate warming effect (Seto et al., 2013). Air stagnation, a process in which air stays in an area for an extended period, is another problem experienced in urban cities due to the impact of urbanization. Z. Li (2019) studied the impact of urbanization by comparing the 6 hourly air stagnation cases of Shenzhen in 1979 and 2010. They identified the complex mechanism through which urbanization process induce air stagnation through changes in surface wind speed and temperature inversion.

In view of the above studies which directly link the deterioration of urban air quality and its health associated impacts to urbanization process, it is important for policymakers and urban planners to consider the influence of urbanization amongst other factors while addressing the issues of urban air quality.

2.2.3 Urbanization and Precipitation

There is sufficient evidence that suggest urbanization or major urban areas influence cloud and the variability of precipitation, a phenomenon known as "urban rainfall effect" (Shem and Shepherd, 2009; Changnon, 1979). There are a number of urban area characteristics which might affect the precipitation level (the so-called urban rainfall

effect), which include: high surface roughness and its resulting impact on convergence; UHI and its effect on atmospheric boundary layers and downstream generation of convective clouds; aerosols which serve as nuclei sources for cloud condensation; and the impact of urban canopy processes on precipitation system (Solecki and Marcotullio, 2013). Regardless of the mechanism involved in 'urban rainfall effect', urban areas and those directly downwind experience more precipitation and heavier rainfall than rural and upwind areas within the same region (Changnon, 1979).

Shi et al. (2017) showed that large scale urbanization (secondary industries, average haze days, and urban population), which is linked to land-use change and air pollution is the main contributing factor to the observed decadal increase and shifting spatio-temporal patterns of heavy regional rainfall in China, but not climatic factors (western Pacific Subtropical High, El Nino-Southern Oscillation, Atlantic Multi-decadal Oscillation, and Antarctic Oscillation). Kishtawal et al. (2010) examined the impact of urbanization on Indian monsoon rainfall changes using in situ and satellite-based precipitation and population data. Their results showed increased trend in intense precipitation in the urban areas compared to non-urban areas of the Indian monsoon region. Using simulation studies (Shimadera et al., 2015) demonstrated the impact of urbanization on the summertime precipitation of Osaka by comparing the case of present land-use with no urban land-use case. Their results showed that in addition to increasing the mean air temperature by 2.1°C, a decrease in mean humidity due to decrease in latent heat flux was observed. The observed increase in precipitation in the urban area compared to surrounding areas was attributed to the increase in the formation of convective clouds due to increase in sensible heat flux because of urbanization. This led to changes in the spatio-temporal distribution pattern of precipitation in and around urban areas. Similarly, X. L. Yang et al. (2012) demonstrated a correlation between

urbanization process and the increasing trend in annual precipitation, rain fall days, and flood season precipitation in the urban areas compared to sub-urban areas of Qinhuai River of Eastern China within the period 1961 – 2006.

The above studies and many other studies (Souch and Grimmond, 2006) have demonstrated a shift and increase in precipitation in urban areas compared to non-urban areas. For rapidly growing and industrializing urban cities to effectively reduce the risks of flooding and waterlogging, they need to control the impact of urbanization on air pollution and regional climate due to their impact on extreme rainfall events (Shi et al., 2017).

2.2.4 Urbanization and Human Comfort

Urban warming has serious consequence on people's comfort and their healthy wellbeing. Human thermal comfort is a condition of the mind, which articulates one's satisfaction or otherwise with his surrounding environment. Environmental factors such as air temperature, radiant temperature, humidity, and wind velocity, when combined with personal factors: clothing insulation and metabolic heat, affect human thermal comfort (Health and Safety Executive, 2021). Frequent and prolonged exposure to heated environments could lead to decreased thermal comfort and increase the risks heat related illness (Y. Y. Lee et al., 2017), such as heat stress. It should be noted that the environmental factors highlighted above are all influenced by factors such as UHI (section 2.2.1) anthropogenic heat flux (section 2.2.1.1), which are manifest impact of urbanization process on urban areas.

Mahmoud and Gan (2018) investigated the historical impact of rapid urbanization on temperature humidity index, effective temperature index, and relative strain index

in Cairo between 1973 and 2017, which are the main indices for evaluating thermal comfort. Besides, increase in air temperature, relative humidity, and vapour pressure, a remarkable increasing trend in temperature humidity index (TRH: 0.33°C/decade), effective temperature index (ETI: 0.29°C/decade), and relative strain index (RSI: 0.06/decade) was observed since 1994, which corresponds to rapid land-use change and increase in impervious surface areas due to rapid urbanization. Moreover, severe heat stress emerged and persist since 1994 and the highest thermal discomfort was identified in urban areas with less impact in new cities with high vegetation cover. Similar results were observed and reported elsewhere for pre- and post-urbanized Cairo (Robaa, 2011). In the contrary, (Doan et al., 2016) showed that while land-use change and anthropogenic heat flux led to increase in the surface air temperature of Ho Chi Minh city (0.22°C in established urban areas and 0.41°C in newly urbanized areas), it didn't translate into significant change in human comfort due to negative influence of urbanization on relative humidity. However, in another study, Yang et al. (2019) demonstrated that the negative effect of relative humidity on thermal comfort is compensated for by the added effect of anthropogenic heat emitted. They further showed that the total thermal discomfort hours in Yangtze River Delta area increases by 27% due to urbanization and that anthropogenic heat and land-use change exerted similar contribution to human thermal comfort. As such, special consideration should be given to the influence of urbanization on human thermal comfort, especially in the built environment, when planning and designing developmental projects.

2.2.5 Urban Climate and Global-Scale Climate Change

As highlighted earlier, the impact of urbanization is mostly on local and regional climate. Nonetheless the process of urbanization has a significant impact on the global-

scale climate change. The relationship between urbanization and global-scale climate change is intricate. Cities, regardless of their trivial spatial extend, exert an influence on global-scale climate change (Masson et al., 2020). Urban areas are the main contributors to anthropogenic sources of greenhouse gases emission, mostly emanating from the use of fossil fuels for heating and cooling, industrial processes, and transportation (Grimmond, 2007). It was suggested that more than 90% of anthropogenic carbon emission emanate from urban cities, and this includes the reduction of global carbon sink through land-use change and deforestation and the clearing of land for cities and roads construction (Svirejeva-Hopkins et al., 2004). Urbanization-induced climate change, as noted by Ren (2015), is an integral part of urban climate change and is influenced by both global and regional climate change occasioned by large-scale man-made and natural forcing and by natural climate variability. The anthropogenic forcings include greenhouse gases emission, land use and land cover (LULC) change, and aerosols emission, while the natural forcings comprise of solar activities and volcanic eruptions (Ren, 2015). On the other hand, global-scale climate change would lead to an evolution of local and regional climate, resulting to occurrence and increased intensity of extreme events (Masson et al., 2020). A recent study (Darmanto et al., 2019) suggests that future projection of urban climates, especially in tropical and rapidly urbanizing megacities, cannot entirely rely on the global climate change and effect of emission scenarios, as the impact of urbanization on urban climate can reach the extent of the effect of global climate change.

Changes in UHI presents a good indication of how urban and rural areas respond to climate change (Oleson, 2012). Due to the different impact of UHI on urban and surrounding rural areas, the two are likely to be impacted differently by climate change (Chapman et al., 2017). The local effect of UHI on urban climate could likely

exacerbate the impact of climate change on urban areas compared to rural areas (Darmanto et al., 2019). As discussed earlier, urban climate is influenced by factors such as anthropogenic heat, wind speed, cloud cover, land cover, etc., as such urban and rural areas would likely respond differently to the influence of climate change. These conditions strongly affect the intensity of UHI and any changes to conditions, especially wind speed and cloud cover (Oke, 1981), occasioned by global-scale climate change could affect the frequency and intensity of UHI. The response of UHI to climate change depends on changes on how changes in temperature, occasioned by climate change, affect the heating and cooling demands by urban residents and its associated anthropogenic heat release (Oleson, 2012). An analysis of the studies conducted on the response of UHI to climate change showed a large variability, which could be explained by changes in the factors that lead to the formation of (Chapman et al., 2017).

As low wind speed results in low heat advection and increased trapping of heat in the urban canyon and cloud cover opens the sky resulting in longwave radiation reaching the surface, if climate changes lead to decrease in cloud cover and wind speed, a responding rise in the UHI would be experienced and vice-versa (Chapman et al., 2017; T.R Oke et al., 1991). Numerous studies have examined the impact of climate change on the UHI at city-scale. For instance, a study by S. E. Lee and Levermore (2012) showed an increase in the UHI of 4K leading to a corresponding rise in indoor temperature by 3K at night in Manchester. Argüeso et al. (2014) modelled the combined effect of future urbanization and climate change on the local climate of Sydney. They demonstrated that projected reduced evapotranspiration and increased urban heat storage would increase the nocturnal temperature (minimum temperature) in urban areas throughout the year with more increase in winter and spring, leading to warmer nights and high risks of heat stress and sleep disorders. Climate change is predicted to

intensify the UHI in Chicago metropolitan area, leading to decreased comfort and increased energy consumption (Conry et al., 2015). Similar observations were reported for the Yangtze River Delta area where combined effect of global warming and UHI intensity were projected to lead to a regional mean surface air temperature of 18.5°C (2070 – 2100) compared to 15.4°C (1961 – 1990) based on the IPCC Special Report on Emission A2 Scenario. This increment is notably higher than the isolated impact of climate change on mean surface air temperature (15.4°C for the period 1961 – 1990 vs 17.9°C due to climate change alone for the period 2070 – 2100).

On the contrary, an investigation by Lauwaet et al. (2016) showed a decreasing effect of global warming on UHI, even though they noted the risks of increased extreme heat events occasioned by climate change. It should be noted though that their simulation study did not account for the impact of future urban growth on the projected UHI, which typically increases the temperature difference between urban and rural areas. Similarly, Kusaka et al. (2012) showed no future variation in UHI intensity of Osaka, Nagoya, and Tokyo due to climate change. It should also be noted that the projected CO_2 emission through 2070 was kept constant (compared to 2011 levels) and that the study focuses on summer months, while another study by Argüeso et al. (2014) demonstrated that the impact of climate change on UHI intensity is more pronounced in colder periods of the year (winter and spring). In Hamburg, it was projected that the weather conditions that intensify UHI would not change with changes in weather pattern due to climate change, as such climate change would not have a considerable effect on the UHI intensity (Hoffmann and Schlünzen, 2013). For the city of London, while Wilby (2003) showed increase in UHI with climate change, no relative changes in UHI were observed at the regional level. In a different study by Mccarthy et al. (2012), however, they noted that while the influence of global-scale climate on the is similar

on both the urban and rural areas, the effects of urbanization would increase the frequency of extreme high temperature and further exacerbate the impact of climate change in urban areas of the UK.

Overall, estimating the impact of climate change on local and regional climate without considering the contribution of urbanization on UHI risks underestimating future extreme temperatures and occurrence and frequency of heat stress related events in urban areas (Chapman et al., 2017). While in general, the impact of climate change on soil dryness would lead to decrease in UHI, its impact on anthropogenic heating and by extension on UHI varies depending on the heating and cooling requirements (Oleson, 2012). Identifying the individual and combined effect of climate change and urbanization would provide opportunities for effective planning of urban adaptation strategies to curb the future impact of climate change and urbanization on urban areas.

2.2.6 Urban Adaptation Strategies

As the process of urbanization continues and the climate continues to warm, the risk, frequency, and intensity of UHI would continue to increase. This would further exacerbate the urban heat stress occasioned by climate change (see section 2.2.5 for the combined effect of urbanization and climate change on urban cities). Besides, the effect of urbanization on local and regional climate is greater in magnitude than the impact of global-scale climate change and would increase the vulnerability of urban residents to future climate change (Grimmond, 2007). As such, to effectively mitigate and adapt to higher heat stress, we must consider the contributing effect of urbanization and rethink how we design and manage our cities.

In addition to other impacts, UHI and or rising urban temperatures is the main manifestation of the effect of urbanization on urban climate. One promising strategy of moderating UHI and its heat stress associated impact is the modification of urban foam

(Oke, 1981). A numerical study on the effect of urban foam (compact-city vs dispersed-city) indicated that while dispersed-city model led to increase in surface air temperature, the compact-city scenario led to temperature reduction (Adachi et al., 2014). Although the authors noted that to achieve effective mitigation, compact-city model needs to be combined with other strategies. In addition, other strategies mainly proposed for mitigating UHI effect include using cool pavement, cool roofs, enhancing vegetation cover, and reducing waste heat. Although the effectiveness of these strategies varies depending on the baseline climate, size, and the layout of the city (Larsen, 2015). Others include increasing surface and roof albedo, greening building surfaces and parking lots, and changing pavement and building materials (Takebayashi and Moriyama, 2012). Details of the main causes and mitigation strategies of UHI is detailed elsewhere (Grimmond, 2007).

Larsen (2015) suggested that mitigation of microclimate must go beyond exterior level strategies to explore land-use planning and passive cooling strategies. For instance, Gill et al. (2007) investigated the impact of green infrastructure on the current and projected temperature and precipitation of Greater Manchester. Results of their energy-balance model showed that replacing 10% of impervious surface with green cover in high-density residential area, resulted in keeping temperature below the baseline temperature (1960-1990). Similar effect was observed with greening roofs in areas with high density of buildings. In another study, using numerical studies, (Papangelis et al., 2012) showed that replacing a commercial area with a green park in Athens led a cooling effect of up to 5°C at night time and induced a cooling effect ranging from 0.5 to 1.2°C in the surrounding area. Stone et al. (2014) investigated the impact of changes to vegetative cover and surface albedo on future (2050) heat-related deaths in 3 US metropolitan cities: Atlanta, Philadelphia, and Phoenix. While a combination of

enhancing surface albedo and vegetation led to an offset of the project heat-related mortality by 40 to 99% in the three cities, each city responds separately to surface modification. Green infrastructure is a promising option for mitigating rising urban temperature, as it generates evapotranspiration while simultaneously reducing surface heat storage capacity (Lemonsu et al., 2015).

Studies such as that by Stone et al., (2014) indicate that there is no universal approach to mitigating rising urban temperatures, but the biophysical and settlement pattern of each city must be considered to determine the most effective mitigation and adaptation strategies.

2.3   Studies on Urbanization and its Impact on Shanghai

Shanghai is a coastal megacity situated in the Yangtze River Delta in East China. It covers a total land area of 6340.5 km^2, a total population of 2428.14 million residents, and a population density of 3830 people/km^2 (Shanghai Municipal People's Government, 2020). Since the economic reform of late 1970s, Shanghai, which is the most populous city in China, has experienced rapid and unprecedented urbanization and economic development. The urban expansion pattern of Shanghai was meticulously studied by (Zhao et al., 2016). The period between 1980 to 2014 witnessed rapid expansion in the city. The pattern of expansion of the urbanized area was initially rapidly outward around the downtown area followed by a slower expansion rate by in filling. The urbanized land area in Shanghai increased threefold during the investigated time at a rate of 10.74%, with the greatest expansion taking place between 2000 to 2004. The maximum expansion rate took place in the north-west, west, southwest, east, and southeast directions. The urban sprawl experienced over the past three decades has resulted in significant environmental and ecological concerns (Zhao et al., 2006). Many

studies have noted and documented the impact of rapid urbanization on the local climate of Shanghai.

Considering the importance of UHI as an indicator of the impact of urbanization on urban climate, there have been many studies, since 1980s on Shanghai's UHI. Studies have attributed the observed increasing trend in Shanghai's UHI to rapid urbanization and economic development (Zhao et al., 2016; Zhou and Wu, 1987; Zhou and Zhang., 1982). Cui and Shi (2012) investigated the impact of population and land-use and land cover change on the evolution of the local climate and ecology of Shanghai. With increasing floating population and urban sprawl, cultivated land has been repurposed for buildings, which has been accompanied by increase in air temperature and reduction in relative humidity, wind speed and vegetation. Moreover, the observed growth in the UHI in Shanghai is mostly influenced by increase in impervious surface and anthropogenic heat emission from transportation and buildings. By replacing natural vegetation cover with impervious surfaces, the surface albedo and surface emissivity of Shanghai was observed to decrease drastically, providing favourable conditions for urban heat island effect (M. S. Jin et al., 2011).

Zhang et al. (2010) studied the annual, seasonal, fixed annual, and the spatio-temporal distribution of UHI intensity of Shanghai using meteorological data from 11 stations for the period 1978 to 2007. UHI was observed to be more intense in autumn and weakest in summer and the general intensity trend conforms to trends to population and the gross domestic product of the city. Tan et al. (2010) studied the relationship between urbanization with UHI and the frequency and intensity of heat wave in Shanghai using meteorological record from 11 stations (in urban, suburban and rural areas) from 1975 to 2004. Their results indicated that variation in the surface warming of urban and surrounding areas showed an increasing trend in UHI effect, which led to

more hot days and increased frequency in heat waves in urban areas. Moreover, a survey of the summer heat-related mortality showed more mortality in urban areas compared to surrounding areas.

Using an integrated approach based on geographic information system (GIS) and remote sensing, Li et al. (2009) quantitatively studied the recent pattern of UHI in Shanghai metropolitan area between 1997 to 2004. While newly developed and highly vegetated remote island exhibit a cooling effect, the rapidly expanding urbanized areas with their characteristic impervious surfaces remarkably increased the extend and scale of hot spots in the city. This coupled with rapid changes in land use and land cover in urban fringes exacerbated the UHI in Shanghai metropolitan area. Studies of the interaction between urban expansion (urban foam) and UHI effect of Shanghai (between 1984 to 2014) showed the urban foam has a direct impact on the city's UHI intensity (Zhao et al., 2016). The urban compactness ratio affects the range of influence and intensity of UHI. When the compactness ratio is less than 0.15, a compact urban design can control the influence and intensity of the UHI, above the value of 0.15, a compact design would worsen the UHI effect.

Data from the Shanghai Environmental Monitoring Centre showed that the air quality index of the city is directly related with the level of urbanization in the city within the period 1983 to 2005, and a spatial pattern of air quality was observed between the urban, suburban, and rural areas, with the urban areas having the worst air quality (Xia et al., 2014). Similar pattern of deteriorating water quality was observed, with the most severe pollution taking place in urban areas (Zhao et al., 2006). Analysis of the historic degradation of water quality in Shanghai, between 1947 to 1996, suggests that 94% of the variability in water quality classification is attributed to urbanization, specifically industrial land use (Ren et al., 2003).

Over the last century, meteorological records showed an increasing trend in the intensity of hourly precipitation, with the frequency of heavy precipitation being significantly higher within the period 1981 to 2014, which coincided with rapid urbanization in Shanghai. The observed extreme precipitation was due to regional warming and increased atmospheric water vapour content and moisture flux. Moreover, the long-term spatial distribution of total precipitation intensity showed an urban rain island feature, with heavy precipitation increasingly concentrated in the urban and suburban areas of Shanghai (Liang and Ding, 2017). High load of atmospheric aerosol load over Shanghai could directly scatter or absorb solar radiation leading to reduced surface isolation and a cooling effect on urban surface. Meanwhile, the aerosols serve as nuclei for cloud condensation and influence the microphysical properties of the cloud (aerosol's indirect effect), which leads to urban areas having different cloud characteristics from surrounding rural areas (M. S. Jin et al., 2011).

2.4 Modelling Approach for Estimating and Predicting the Impact of Urbanization on Urban Climate

It should however be noted that most of the studies on the effect of urbanization on the microclimate of Shanghai (section 2.3) are based on historical observation of meteorological records. As already discussed in section 2.2.5, urbanization, especially rising urban temperatures would exacerbate the heat-related stress and mortality in urban areas. As such it is reasonable to develop metrics to quantify the contribution of urbanization to local and regional climates, while at the same time predicting future impacts to provide policy directions planning future urbanization and effective mitigation of rising temperature and its related heat-stress and mortality impacts.

While greenhouse gas emission and land-use change are the main driving anthropogenic causes of global-scale climate change, it has been demonstrated by many studies (section 2.2) that modification to land-use and land-cover due to urbanization is one of the main driving factors leading to rising UHI, precipitation, wind speed, humidity, and air quality of urban areas. However, is difficult to separate the warming effect of these factors. Besides, the impact of urbanization is mostly measured by comparing the differences in observation between urban and rural areas, but different results are obtained depending on whether population data or satellite measurement of night lights are used to classifying urban and surrounding rural areas (Kalnay and Cai, 2003). Another issue is the possibility of some weather monitoring stations (especially those situated in suburban/rural areas and those downwind of urban areas) being affected by urbanization (Philandras et al., 1999). For urban planning and decision purposes, detailed information is needed that cannot be easily obtained from observation networks (Hamdi et al., 2020).

Another strategy of measuring the impact of urbanization is to analyse temperature time series stations that are were previously classified rural but currently considered urban due to urban sprawl (Philandras et al., 1999). But one challenge with this approach is the unavailability of comprehensive pre-urban records for comparison in most areas. A more viable approach used by (Kalnay and Cai, 2003) is to compare trend in surface temperature, which is sensitive to changes in land-use, and trends in reconstructed surface area from the reanalysis of global weather, which is independent on surface observations to estimate and quantify the impact of land-use change on urban climate. Another approach is using satellite to identify land use changes which can then be correlated with meteorological temperature record and satellite thermal data (Romero et al., 1999).

Considering the above discussed factors, it is rather challenging to measure and evaluate the impact of urbanization on temperature based on comparison of observed data. Besides, the collective effect of global-scale climate change and rapid urbanization would likely make urban dwellers susceptible to various environmental challenges including extreme weather events, poor air quality, heat stress, and poor water quality. It is therefore essential to understand and estimate the future effect of climate change and urbanization on local and regional climate and to develop robust mitigation and adaptation strategies (Chen et al., 2011). Numerical modelling is another promising tool and a viable approach for investigating the historical effect of urbanization on local and regional climate. One of the advantages of the modelling approach is the possibility to eradicate the influence of climate variability and non-stationarity (Thompson, 2009).

Various numerical modelling studies have been conducted to investigate and predict future individual and combined effect or climate change and rapid urban growth on the climate of many urban cities across the world. For instance, (Li et al., 2009) used the WRF model with 5 one-way domains to study the impact of urbanization and its pattern on the UHI and rainfall pattern of Singapore. Adachi et al. (2014) used the WRF model to study the effect of urban form on the moderation of UHI in Tokyo Metropolitan area and for the prediction of the best model for further urban growth planning. Yang et al. (2016) conducted numerical experiments based on regional atmospheric model coupled with single layer urban canopy model and the future climate forcing to investigate the impact of urban foam (compact-city vs dispersed city) on the future thermal environment of Beijing. By coupling the WRF model with the Urban Canopy Model, H. Li et al. (2019) study the intensity of the UHI in Berlin, which was due to the difference in the sensible heat flux between impervious and vegetation surfaces. Similar

model was used to simulate and study UHI in Hangzhou during long-lasting heat wave (Chen et al., 2014). Moreover, numerical modelling approach has been utilized to study hypothetical urban growth models to develop strategies for the mitigation and adaption to the individual and combined effect of climate change and urbanization on urban climate (see section 2.2.6). As such, numerical modelling approach provides with opportunity not only to study the historical effect of urbanization but also predict future effect of urban growth on urban climate and plan mitigation and adaptation strategies.

For the reminder of this thesis, numerical modelling approach using the WRF model coupled with the urban canopy model and NOAH model would be used to study the impact of future urban growth on the climate of Shanghai. Details of the methodology used in data collection and model set up are presented in chapter 3.

3 Methodology and analytical tools

3.1 WRF Pre-processing System (WPS)

The WPS program is mainly used for real data simulation. Its functions include 1) defining the simulation domain; 2) Interpolate land data (such as topography, land use and soil type) into the simulation domain; and 3) Extracting and inserting meteorological data from another model into the simulation domain.

WPS is a set of three programs whose combined function is to prepare inputs for real programs that simulate real data. Each program performs a preparatory phase: *geogrid.exe* defines the model domain and inserts static geographic data into the grid; *ungirb.exe* extracts weather fields from general regularly-distributed information in binary form (GRIB) files; And *metgrid.exe* horizontally interpolates the meteorological field extracted by *ungrib.exe* into the model grid defined by *geogrid.exe.*
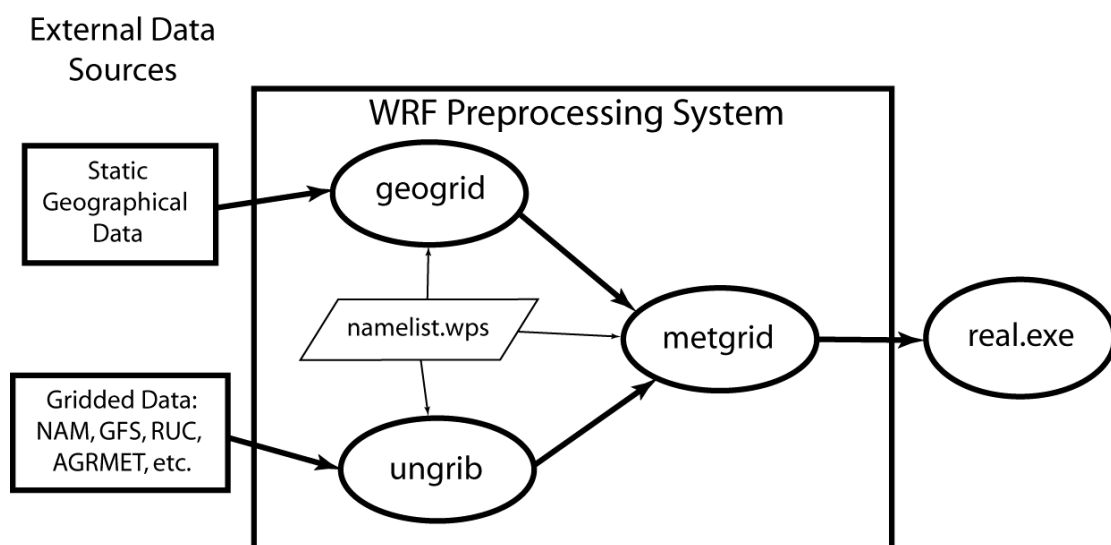
Figure 3.1 WPS flowchart (Morris 2016)

The data flow between WPS programs is shown in the Fig 3.1 above. Each WPS program reads the parameters from a common name list file – *namelist.wps*, as shown in the figure. This name list file has a separate name list record for each program and a

shared name list record that defines parameters used by multiple WPS programs.

3.1.1 geogrid.exe

The purpose of *geogrid.exe* is to identify simulated areas and interpolate various terrain data sets onto pattern grid points. The simulation region is determined by setting the parameters related to "geogrid" in the *namelist.wps* file. In addition to calculating latitude and longitude and scaling factors for each grid point on the map, *geogrid.exe* interpolates default values for soil type, land use type, terrain height, annual mean deep soil temperature, roof vegetation cover, roof albedo, maximum snow albedo, and slope categories. The global dataset of these fields can be downloaded from the WRF website, and the data can be viewed as constant over time, so it only needs to be done once.

In addition to interpolating the default static data, the *geogrid.exe* program can also interpolate more continuous and different types of terrain into the simulated area. It is able to interpolate new or additional data sets into the simulated region by applying the table file - *GEOGRID.TBL*. The *GEOGRID.TBL* file defines all terrain fields that can be generated by *geogrid.exe*. It describes the method needed to interpolate a terrain site and the exact location of the required data.

Domain Configuration
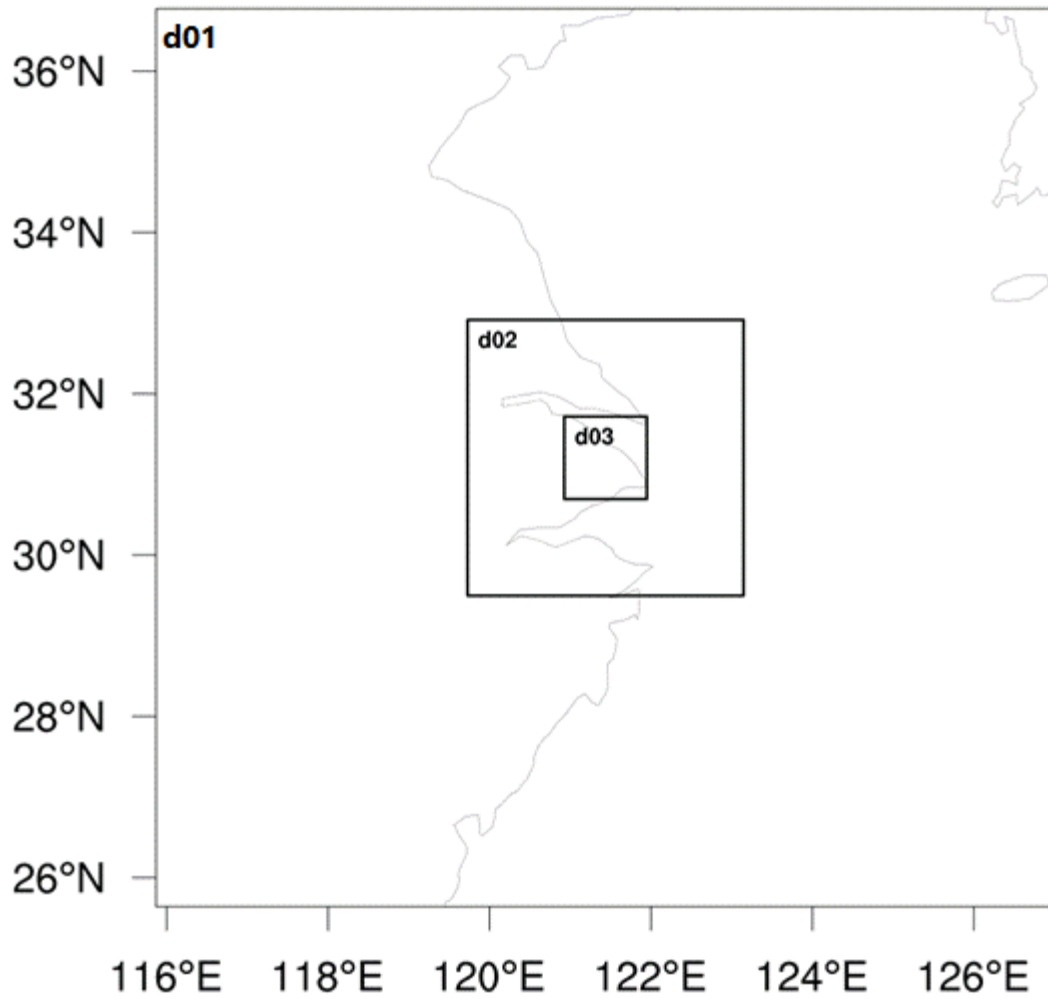
Figure 3.2 Examples of configuration of domains (nested domain: D01, D02 and D03)

The files generated by *geogrid.exe* are in WRF I/O API format, Network Common Data Form（NetCDF）output files can be generated in NetCDF I/O format, which is easier to use some external software - NCView, NCL to visualize (draw topographic maps).

3.1.2 ungrib.exe

The *ungrib.exe* program reads GRIB files, "extracting" the data, and writes it out in an intermediate format that is able to be read by *metgrid.exe*. GRIB files contain weather element fields that change over time and are derived from other regional or global models, such as National Centers for Environmental Prediction (NCEP) 's Global Forecast System (GFS) models. The GRIB file contains more factor fields than are needed to start WRF, thus the *Vtable* file (see Appendix for example of the *Vtable*) defines which fields from the numerous fields of the GRIB files that are to be extracted and then write into the intermediate file format understood by the *metgrid.exe* program. Detail descriptions of the fields in the *Vtable* can be found on the WRF-ARW User's Guide V3, "creating and editing Vtable" section (Wang et al., 2012).

3.1.3 metgrid.exe

The function of *metgrid.exe* program is to horizontally interpolate the meteorological element fields extracted by *ungrib.exe* program into the simulated area determined by *geogrid.exe*. The interpolated data can be recognized and absorbed by WRF's *real.exe* program. The time periods for those interpolated by *metgrid.exe* can be adjusted by setting the share record section in *namelist.wps*, and the time is set separately for each simulated region (outermost and nested). Like the *ungrib.exe* program, *metgrid.exe* processes data that changes over time, *metgrid.exe* program is needed to be performed every time with a new simulation.

The *METGRID.TBL* file provides control over how each meteorological field is interpolated. As with the *GEOGRID.TBL* file, the *METGRID.TBL* file has a section for each field, and within each section, it is possible to specify options such as the interpolation methods to be used, the field that will act as the mask for masked interpolations, and the staggering to which a field will be interpolated (Moris, 2016).

3.2 WRF model

WRF is a new high resolution mesoscale meteorological Model and data assimilation system. The model project is founded in the late 1990s by the National Centre for Atmospheric Research, the Centre for Environmental Prediction, the Weather Prediction Systems Laboratory, the Air Force Weather Service, the Naval Research Laboratory and the Oklahoma University Centre for Storm Analysis and Prediction. WRF models can provide researchers with simulations based on actual atmospheric conditions (derived from observations and analyses) or ideal conditions (Wang et al., 2012). WRF provides a flexible and efficient platform for forecasting and reflects the latest advances in physics, numerical and data assimilation provided by a wide range of research teams. As a new generation of fully compressible non-static model, WRF has the characteristics of being portable, easy to maintain, expandable, efficient, and capable of parallel computing (Wang et al., 2012). At present, this model system has been greatly promoted by many research institutions and universities constantly using and improving the model, making the model simulation effect more accurate.

WRF model has two dynamic cores, a data assimilation system and a software architecture that supports parallel computing and system scalability. The model is suitable for a variety of meteorological applications ranging from tens of meters to thousands of kilometres. WRF model mainly has two dynamic cores, which are NMM (non-hydrostatic Mesoscale Model) mainly applied and operational forecasting; and the ARW (Advanced Research WRF) model for advanced research (mainly provided to researchers for original Research). The WRF-ARW dynamic core is chosen in this study due of its widespread use in several fields of research and real-time forecasting worldwide (Morris et al., 2015b; Martins et al., 2015; Li et al., 2016).

Fig 3.3 depicts the major components and a flowchart illustrating the functionality of the WRF modelling system's components. The software framework offers infrastructure for dynamic solvers, physics packages that interface with the solver, initialization routines, and other model-related software components (Skamarock et al., 2008).
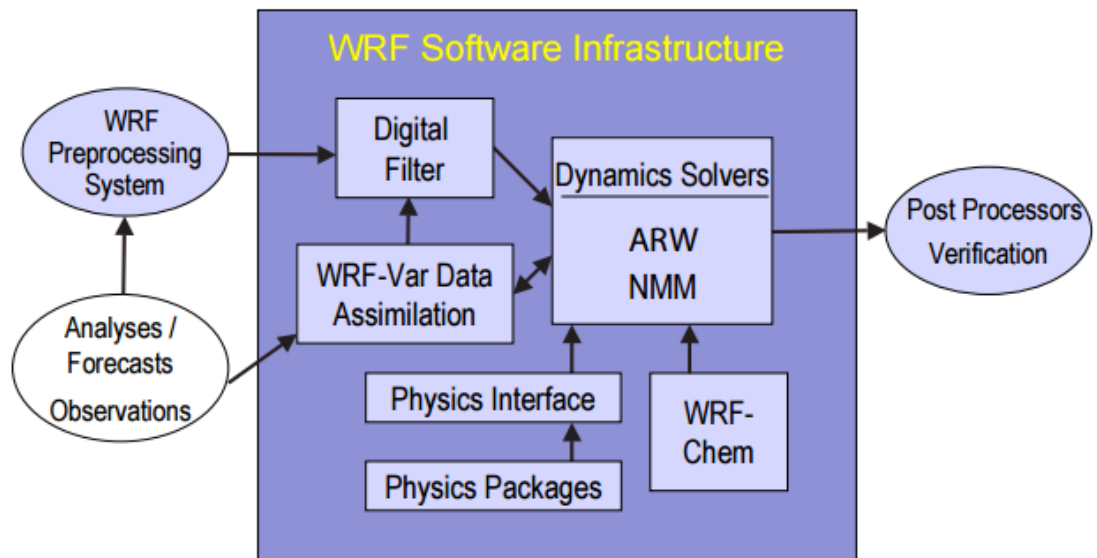
Figure 3.3 WRF software infrastructure (Skamarock et al., 2008)

3.2.1 WRF-ARW model

ARW is a completely compressible, Eulerian mass coordinate non-hydrostatic model with a run-time hydrostatic option that solves conservative equations of mass, momentum, and energy using terrain-following coordinates and with the possibility of multiple layering to increase precision across the area of interest (Skamarock et al., 2008). It is a numerical weather forecast model of the next generation with enhanced dynamics, physics, and numeric methods. Horizontal discretization is accomplished using Arakawa C-grid. For scalar variables, the model equations are conservative. Additionally, the model incorporates a time-split third order Runge-Kutta integration scheme for model integration (Skamarock and Klemp, 2008) with higher order advection methods, comprehensive Coriolis, curvature, and mapping terms. The model is commonly used in hydrology and meteorology in metropolitan areas (Chen et al., 2011; Li et al., 2013). Additional details regarding the model and its several governing equations are available in the NCAR ARW Technical Note (Skamarock et al., 2008).

As with the WPS, the ARW generates two critical executable files during the model installation process (*real.exe* and *wrf.exe*). The *real.exe* program is responsible for handling real-world input and model initialization, whereas the *wrf.exe* software is responsible for simulation integration and computation of all provided physics and dynamics settings.

The *real.exe* program is a real-data initialization and pre-processor for the WRF model (*wrf.exe*). It processes pre-processed data from the WPS program and generates the initial and boundary conditions for later use. *Real.exe* is to ensure that the data has been interpolated horizontally to the right grid-point spacing for each variable and that the winds have been rotated correctly to the WRF model map projection. Also, *real.exe* gathers the 3D data like pressure, wind speed, temperature, relative humidity,

geopotential height, soil temperature, soil moisture, soil liquid from WPS and import to WRF. Other meteorological data from the WPS are also handled by *real.exe* like sea level pressure, surface pressure, surface wind seed, surface temperature, surface relative humidity, input elevation and so on. For regional predictions, multiple time periods must be processed by *real.exe* in order to provide the model with a lateral boundary file.

ARW.exe then processes the numerical integration of the model and calculates the different physical and dynamic options using the initial and boundary conditions generated by the *real.exe* program. The program runs the model simulation using the run-time selected *namelist.input* options (such as physical selection, time step, simulation length, and nested type) and outputs history and restart files that can be used to start the program later. A simplified flowchart for WPS and WRF interactions and dependencies is shown in Fig 3.4
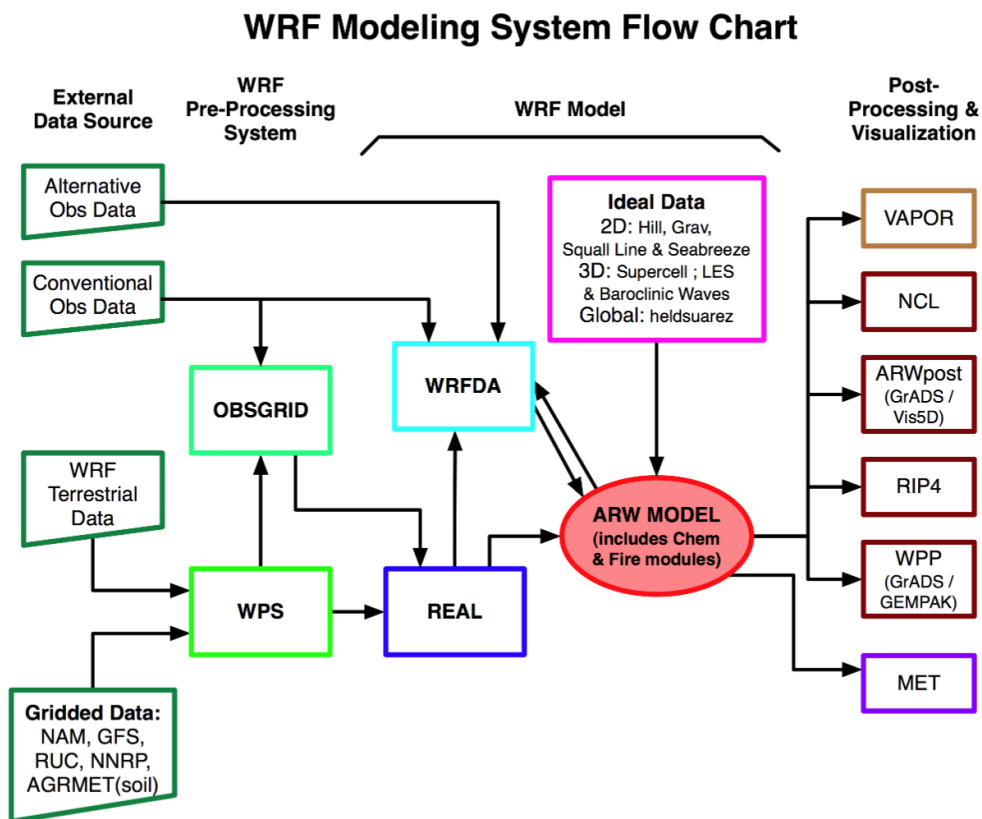
Figure 3.4 WRF modelling system flow chart (MMM, 2015)

3.2.2 Noah Land Surface Model

Noah LSM is a land model of WRF, which has been widely used. As a coupled atmospheric model for lower boundary layer conditions, Noah LSM has a basic function of providing surface sensible heat, latent heat flux and surface temperature. Its model is based on diurnal varying Penman potential evaporation approach; a multi-layer soil model, surface hydrology, frozen ground physics and a modestly complex canopy resistance parameterization (Chen et al., 1996; Chen et al., 1997; Chen and Dudhia, 2001; Ek, 2003). predictive variables include liquid water, ice, temperature of soil layer, water amount stored in the plant canopy and snow stored on the ground (Chen and Dudhia, 2001). The main objective is to provide surface sensible and latent heat fluxes, as well as surface skin temperature, as lower boundary conditions for linked atmospheric models.

For simulation area without an urban canopy model employed (i.e., Outer nested region like D01 and D02), the urban areas parameters are approximated by a universal urban parameter in Noah LSM. The following parameter values are used to represent the zero-order influence of urban surface (Liu et al., 2006): (1) roughness length is 0.8m, representing the turbulence caused by building drag or rough elements; (2) Surface albedo as 0.15, representing short-wave transmission in urban blocks; (3) The volumetric heat capacity of urban surfaces (walls, roofs and roads) is $3.0 Jm^{-3}K^{-1}$, assuming surface as concrete or asphalt; (4) Soil thermal conductivity 3.24 W $m^{-3}K^{-1}$, representing the large heat capacity of urban buildings and roads; (5) The decrease of the greening rate in urban areas leads to the decrease of evaporation. This method has been successfully applied in real-time weather forecasting (Liu et al., 2006) and in studying the impact of urbanization on land and sea breeze circulation (Lo et al., 2007).
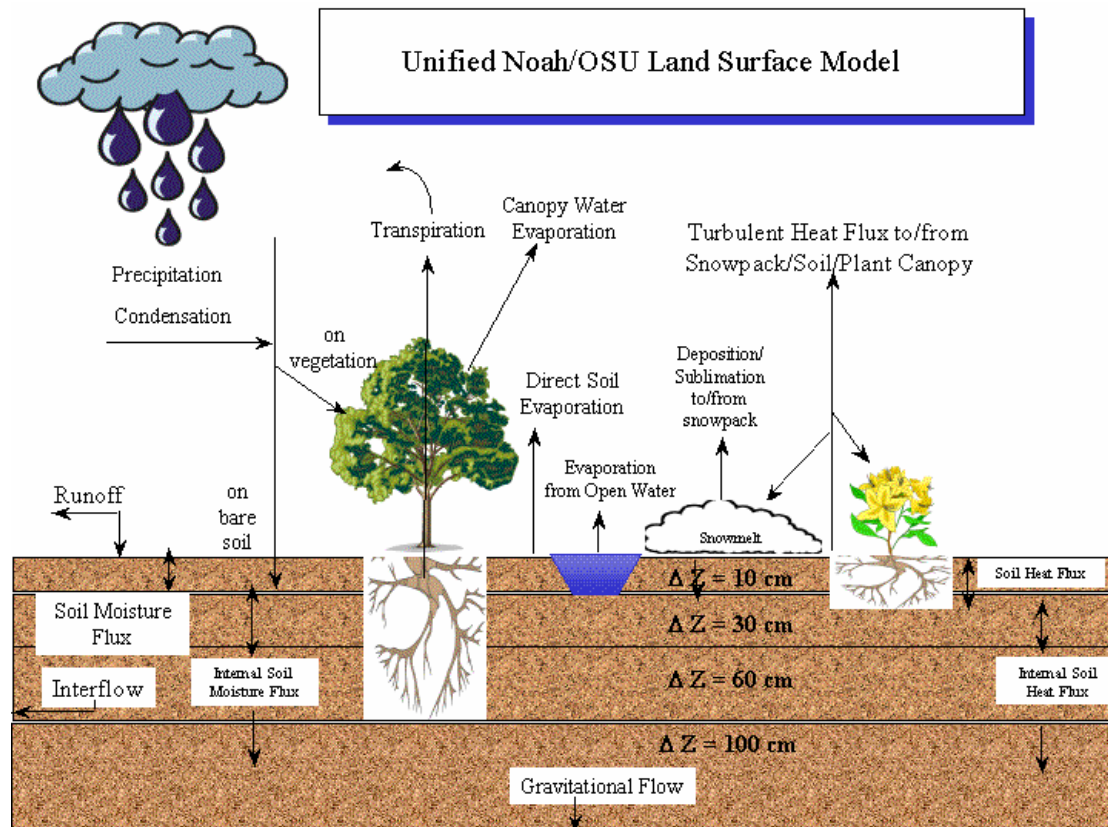
Figure 3.5 WRF/Noah LSM model (Kusaka, 2004)

3.2.3 Urban Canopy Model

The single-layer urban canopy model was invented by Kusaka (2004). The model assumes that street canyons are infinitely long and thus represent the geometry of the city. UCM can recognize the three-dimensional surface of the city. At Street Canyon, UCM considers the effects of shadow, reflection and capture on radiation and prescribes an additional wind profile description document. Predictive variables include roof, wall, and road surface temperatures (calculated from the surface energy balance) and temperature profiles (calculated from the heat conduction equation). The surface sensible heat flux of each surface was calculated by Monin-Obukhhov similarity theory and Jurges formula. The total sensible heat flux of roof, wall, road and city block is transferred to WRF-Noah model. The total momentum flux is calculated in a similar manner. UCM calculates canyon drag coefficients and frictional velocities using a

44

stability similarity function of momentum. The total friction velocities of converged urban and non-urban surfaces are transmitted to the WRF boundary layer scheme. Anthropogenic heat and its diurnal variation need to be added to the sensible heat flux output by the urban canopy model. In UCM, about 20 physical parameters are considered

When UCM is coupled with Noah LSM in WRF model, the cumulative sensible heat flux of the grid can be estimated by the following formula as:

$$Q_h = F_v \times Q_{hv} + F_u \times Q_{hu}$$

Where Q_h represents the total sensible heat flux of a certain grid simulated. F_u represents the percentage of urban underlying surface, such as cement, asphalt, and other impermeable underlying surface; while F_v represents the percentage of natural surface, such as urban grassland, bushes, crops, and trees. Q_{hu} is the sensible heat flux of artificial surface (including artificial heat) calculated by UCM, while Q_{hv} is the sensible heat flux of natural surface calculated by Noah LSM (Chen et al., 2011).

Similarly, latent heat flux, upward long-wave radiation flux, albedo and emissivity are estimated in a similar way (Chen et al., 2011).

3.3   Other analysis tools

3.3.1 ArcGIS

ArcGIS is a world leader for the design and development of Geographic Information Systems software developed by Environmental Systems Research Institute, Inc. GIS technology through this software allows the organization, manipulation, analysis, and visualization of spatial data, often revealing relationships, patterns, and trends (Scott, 2009).

In this study, ArcGis10 is used mainly for making maps of underlying surface distribution, adding shapefile, reclassifying land use data, reprojection and splicing of

raster data, and converting data into ASCII format for further WPS processing.

3.3.2 NCAR Command Language

The NCAR Command Language, developed by the National Centre for Atmospheric Research's Computational & Information Systems Laboratory and funded by the National Science Foundation, is a free interpreted language optimized for scientific data processing and visualization (NCAR, 2015).

In this study, all WRF simulation results were displayed after reading and graphically processing with NCL script. Figure 3.6 shows the average spatial distribution of planetary boundary layer height in the simulated region.
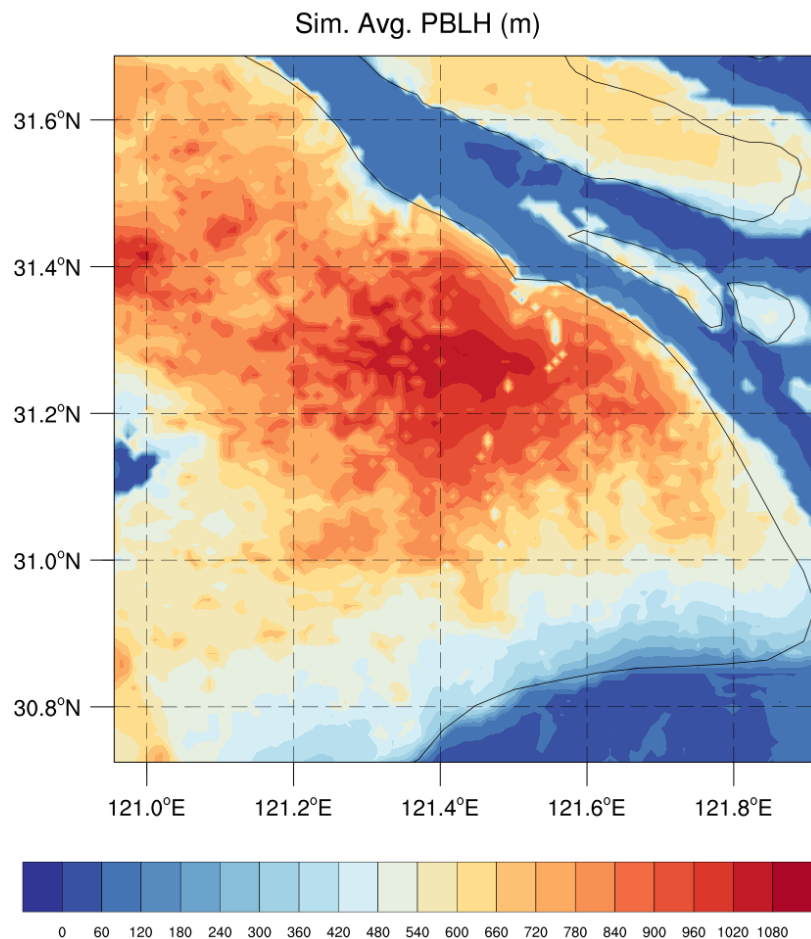
Figure 3.6 Averaged planetary boundary layer height distribution of Shanghai area during simulation

3.3.3 OriginPro

OriginPro is a proprietary computer program for scientific graphing and data analysis on an interactive basis. It is licensed and produced by OriginLab Corporation and operate on Microsoft Windows platforms. Statistics, curve fitting, signal processing, and peak analysis are all included in the software's data analysis functionality. OrginPro can read files in a variety of formats, including Excel and NetCDF, and to produce plotted graphs in a variety of image file formats (Origin Lab 2013).

In this study, OriginPro is used to process discrete data results and output them as line charts that change over time to intuitively show the logic behind the simulation results.

3.3.4 MATLAB

MATLAB is a proprietary multi-paradigm programming language and numeric computing environment developed by MathWorks inc. MATLAB can be used to do matrix operation, function and data drawing, algorithm implementation, the creation of user interface and program interface written in other languages (Tranquillo, 2011).

MATLAB 2020b is used in this study to process a large number of observational data and the data matrix of WRF simulation results and compare the simulation results to obtain the fitting effect.

3.4   NCEP Final analysis (FNL) data

The NCEP FNL Operational Global Analysis data set consists of (0.25° x 0.25°) grids that are prepared operationally every six hours. This FNL comes from the Global Data Assimilation System (GDAS), which gathers observational data from the Global Telecommunications System (GTS) and other sources on a continuous basis for the purpose of conducting different analyses (NCEP et al., 2000). The FNLs are modelled using the NCEP-used Global Forecast System, however they are created approximately

an hour after the GFS is initialized. The FNLs are postponed allowing for the inclusion of more observational data. The GFS is run early to accommodate time-sensitive forecast requirements and initializes with the FNL from the previous 6-hour cycle.

The analyses are provided on the surface, at 32 obligatory and non-mandated pressure levels ranging from 1000 millibars to 10 millibars, in the surface boundary layer and other sigma layers. Surface pressure, sea level pressure, geopotential height, temperature, sea surface temperature, soil temperatures, ice cover, relative humidity, u- and v-winds, vertical motion, vorticity, and ozone are all included as parameters (NCEP et al., 2000).

3.5   Conclusion

This part of the Thesis details the different techniques and tools used to achieve the stated goals and objectives of this research. These include weather research and forecasting model, NOAH land surface model, and urban canopy model, as the main tools that this research relies on to analyse the impact of urbanization on local climate of Shanghai. Other tools such as ArcGIS, NCL and MATLAB are used to process the simulation results generated by WRF to present intuitive images for subsequent analysis and conclusions.

In addition, FNL data provided all the side boundary conditions for this study to drive the dynamic downscaling simulation of WRF, and hourly observation data from 11 observation stations in Shanghai provided a strong argument for the simulation validation of this study.

4 Evaluation of NOAH/SLUCM coupled to WRF and urban climatology simulation of Shanghai

4.1 Introduction

The rapid development of urbanization in China has changed the physical properties and surface morphology of the underlying surface, thus affecting the weather and climate characteristics. Studies show that in the process of urbanization, the temperature (Kalnay and Cai, 2003), wind speed (Tao et al., 2018), sunshine (Wu et al., 2015) and precipitation (Wang et al., 2007) of the city are all affected by land use change to a certain extent. Due to the interaction between land use data and local meteorological elements, the accuracy of weather and climate simulation results is also affected by the degree of matching between land use data used in the model and the actual situation (Madala et al., 2019).

Currently, in the WRF Model, the default data set is relatively out of date. One is the United States Geological Survey (USGS) data, updated in 1993 and divided into 24 categories. The other is the moderate-Resolution Imaging Spectroradiometer (MODIS) data, which was updated in 2001 and divided into 20 categories, with only one land category representing cities. Studies have shown that more precise and accurate land use data can improve the simulation effect of the model (Cao et al., 2015), so it is usually necessary to optimize and update the land use data before the operation of the model.

The change of land use caused by urban development is reflected in the continuous outward expansion of urban outer contour and the increasing complexity of urban inner spatial structure on the other hand. Therefore, the update of land use data in WRF model is mainly about the correction of urban land use area and the refinement of urban inner

classification. In terms of urban area correction, Chang Ming et al., (2014) reclassified existing local land cover data according to USGS classification standards to generate new land use data. Because the updated data are more consistent with the actual land use, the simulation effect of WRF model on temperature, wind speed and water vapor pressure are improved. In terms of refinement of the classification of inner cities, WRF/UCM supports researchers to further subdivide urban built-up areas into low-intensity residential areas, high-intensity residential areas, industrial and commercial areas, and transportation areas (or called "low-density areas", "medium-density areas", and "high-density areas"). Studies show that urban heterogeneity has a certain impact on meteorological elements and their distribution characteristics (Song et al., 2014), so it is necessary to consider the fine classification of cities in the model.

In this chapter, a land use and land cover dataset from the Mega-Cities Project (Murayama et al, 2015; Gong et al., 2017) is used. The dataset is generated by collecting high spatial resolution satellite imageries with geometrically corrected. A supervised classification method with maximum likelihood algorithm is used to the classification. Using this data set, the urban non-uniformity is fully considered, and the urban built-up area is subdivided into 2 more categories. On the other hand, the anthropogenic heat input is estimated according to the data of Shanghai statistical yearbook (Shanghai Statistics Bureau, 2020), also the daily variation curve is corrected. The simulation results using updated urban canopy model is compared with the default data set of WRF, and the influence of different land use data optimization schemes on the simulation process is studied, which verifies the ability of WRF/Noah/UCM model to simulate local weather in Shanghai. The model is validated against a network of observation, followed by a discussion of simulation results.

4.2   Methodology

4.2.1 Study region

Shanghai is located in the eastern part of China, at the lower reaches of the Yangtze River, with its global positioning system coordinates of 31° 13' 27.6996" N and 121° 28' 9.0120" E, with a total area of 6,340 km^2. As a part of the Yangtze River Delta impact plain, Shanghai is densely covered with rivers that has rich water systems. The terrain of Shanghai area is generally broad and flat as average elevation of Shanghai being only 2.19 meters. Its highest point is located on Dajinshan Island in Jinshan District of an altitude of 103.7 meters.

Shanghai has been one of the largest metropolises in China ever since 1843, when ports were opened, and the development of the hinterland trade began. Due to its unique geographical and climatic advantages, the city has been endowed with unlimited development potential and opportunities, gradually replacing Guangzhou as the centre of foreign trade. According to the data in 2019 (Shanghai Statistics Bureau, 2019), more than one-third of the city's Year-end Resident population are 'floating people', and the rapid growth of the floating population and many immigrants indicates that a trend of increase in the total population of Shanghai. The high intensity of human activities has greatly influenced the land use types in Shanghai. Since 1990, a large amount of arable land was occupied by building land, which has resulted in the total area of construction land in Shanghai being tripled compared to 30 years ago. Now, the total construction land of this city is as high as 46% of the land area, far more than Tokyo, Paris and other international metropolises (Shanghai Statistics Bureau, 2019).

Due to the early urban development of Shanghai, its urban morphology and land use situation is complex which makes it a good sample for the study of urban development and its impact on regional climate. At the same time, with the rapid

development of Shanghai, the city is still in constant change, so it is necessary to study the updating of urban land use data. Shanghai is the representative of the urban agglomeration in the Yangtze River Delta, and its study can also serve as a reference for other cities in the Yangtze River Delta. Therefore, this study has chosen Shanghai as its region of study.

4.2.2 Model and experimental design

The key to understanding local climate research first comes from the analysis of meteorology data, which can be recorded by 11 in-situ observation stations located in Shanghai. However, the discrete location of each station is not able to provide a whole picture of the local climatic characteristics, therefore, a spatio-temporal continuous analysis performed by a proven numerical simulation tool is needed.

In this study, ARW dynamic core coupled with NOAH land surface model (Chen and Dudhia, 2001; Tewari et al., 2007) and the single layer urban canopy model (Kusaka and Kimura, 2001; Chen et al., 2011) is used to conduct the simulation. The version of WRF is 3.8.1, renowned to be a next-generation mesoscale weather and climate simulation tool (Skamarock et al., 2008). The combination of these models makes WRF even able to connect the land surface, urban canopy and the overlying atmosphere and process taking place among them (Chen et al., 2014). The ability to capture and reflect impacts of urbanization on near surface meteorological process is also an advantage of the combination (Miao et al., 2009; Chen et al., 2011). As a simulation tool, user-defined land use and land cover data can be input as replacement of default dataset provide better performance in urban effect assessment. Figure 4.1 illustrates the domain configuration of the model and the terrain of the whole area of interest. A three one-way nested domain with a horizontal resolution of 9×9 km, 3×3 km, and 1×1 km, for d01, d02 and d03, are respectively configured to handle the

numerical simulation of the area.
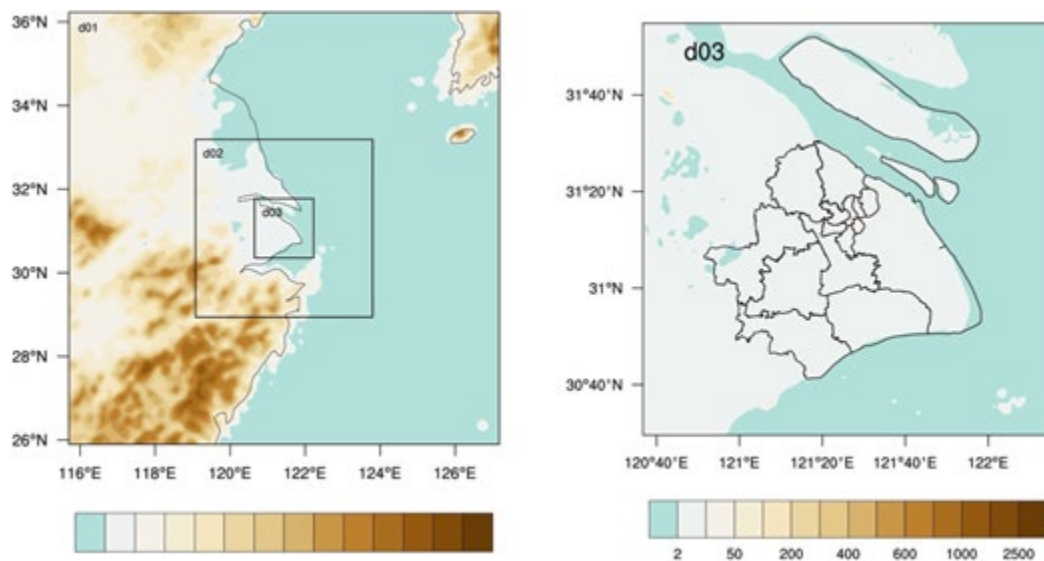
Figure 4.1 Domain setting of the simulation and terrain height of simulation area

There are 128 × 128 grids for D01, which covers most areas in Southeast China. D02 with 118 × 118 grids are mainly Yangtze River Delta, while D03 covers only the whole central area as our main study interest. For the vertical setting, there are 34 hydrostatic-pressure levels to resolve vertical layers for all domains, with 15 of the levels are reserved below 850 hPa to further resolve turbulence and frequent changes of atmospheric variables within the lower planet boundary layer (PBL) and top at 100hpa. Additionally, these lower levels would be helpful in illustrating the small-scale feature near Earth's surface (Morris et al., 2016)

Land Use and Land Cover
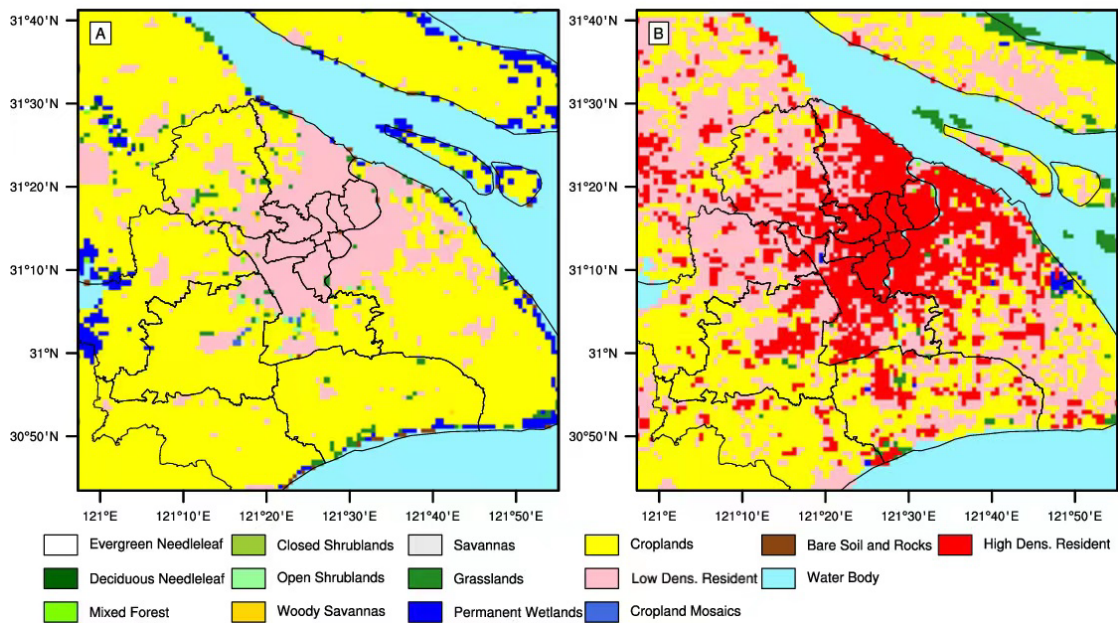
Figure 4.2 Land use and Land cover map for (a) Default as MODIS, and (b) Updated urban land surface using Mega-cities Project data

Default Land use and Land cover dataset in WRF uses MODIS 2001 data, which is out of date in its classification of LULC type but still has a relatively high accuracy of classification when the gird scale is large enough. To save on more computational costs, both d01 and d02 are still using the default MODIS dataset. For d03, there are 4 cases designed in different surface dataset scenarios to evaluate the performance and to conduct further analysis: (a)MODIS, (b)URB, (c)URB_noAH, (d)CONTROL. Case a MODIS represents the default simulation setting and physical characteristic of the land surface in d03. The default data in WRF has not been updated since 2001. The resolution for this dataset is 1km. Case b as URB is using the updated land use and land cover dataset from the Mega-cities Project led by University of Tsukuba (Murayama et al, 2015; Gong et al., 2017) to replace all grids within Shanghai area. The land cover type for urban area is single in MODIS dataset as in 'Low intensity residential area', while there are 2 sub-classes in this updated dataset: Low intensity residential area (LIR) and High intensity residential area (HIR). This data would be useful in explaining the

54

variation in development density and provides more details in further simulations. Case c as URB_noAH represents urban surface land cover without anthropogenic heat emission as a representative of heat source from human activities in the simulation settings, which evaluates the contribution of AH in urban area. Finally, for the CONTROL case, all the urban surfaces are removed and replaced with natural vegetation as in rural space. The no-urban (case d CONTROL) method of evaluating UHI can largely remove effects like sea-land breezes, heatwaves and other advections that may have an influence on the results other than purely urbanization process (Li et al., 2011; Bohnenstengel et al., 2011). This approach has proved to be a reliable way to successfully evaluate urbanization effects (Wang et al., 2014).

Table 4.1 Main Physical parameterization setting

	D01	D02	D03
Microphysics Scheme	single-moment six-class (WSM-6) microphysics scheme	single-moment six-class (WSM-6) microphysics scheme	single-moment six-class (WSM-6) microphysics scheme
Longwave Radiation Scheme	Long-wave Rapid Radiative Transfer Model (RRTM)	Long-wave Rapid Radiative Transfer Model (RRTM)	Long-wave Rapid Radiative Transfer Model (RRTM)
Shortwave Radiation scheme	Dudhia cloud radiation scheme	Dudhia cloud radiation scheme	Dudhia cloud radiation scheme
Surface-layer Scheme	Monin-Obukhov similarity theory	Monin-Obukhov similarity theory	Monin-Obukhov similarity theory
Planetary Boundary scheme	Yonsei University (YSU) scheme	Yonsei University (YSU) scheme	Yonsei University (YSU) scheme
Convective Cumulus Parameterization Scheme	Kain-Fritsch convective cumulus parameterisation	Kain-Fritsch convective cumulus parameterisation	N/A
Urban Canopy Model	N/A	N/A	SLUCM

Physical parameterizations used are listed in table 4.2, including the microphysics scheme of single-moment six-class (WSM-6) microphysics scheme (Hong and Lim 2006; Dudhia et al., 2008), and a surface-layer scheme based on the Monin-Obukhov similarity theory. For radiation, the Dudhia shortwave radiation scheme (Dudhia 1989), and the RRTM longwave scheme (Mlawer et al., 1997) was used. On the D01 and D02, the Kain-Fritsch convective cumulus parameterization scheme (Kain 2001) was applied. D03 does not need any cumulus parameterization as it is able to resolve updrafts and downdrafts in such a sufficiently refined resolution.

The UCM as single layer urban canopy model was used to consider the effects of

urban geometry on surface energy balance and wind shear for urban regions (Kusaka et al., 2001; Kusakaand Kimura，2001).This model includes shadows from buildings，canyon orientation，diurnal variation of azimuth angle, reflection of short and long wave radiation, wind profiler in the canopy layer, anthropogenic heating associated with energy consumption by human activities and multi-layer heat transfer equation for surfaces.(Chen et al., 2011)

Table 4.2 SLUCM parameters settings for MODIS case and URB case

Urban Parameters	LIR	HIR	MODIS
Mean Building height (m)	5	27.5	7.5
Standard deviation of building height (m)	1	8	3
Building roof width (m)	8.3	24	9.4
Road width (m)	8.3	16	9.4
Maximum Anthropogenic heat (W m^{-2})	20	120	0
Urban Fraction	0.5	0.9	0.9
Volumetric heat capacity of roof (MJ m-3 K-1)	1.20	1.20	1.2
Volumetric heat capacity of building wall (MJ m-3 K-1)	1.40	1.40	1.40
Volumetric heat capacity of ground (road) (MJ m-3 K-1)	1.68	1.68	1.68
Thermal conductivity of roof (W m-1 K-1)	0.67	0.67	0.67
Thermal conductivity of building wall (W m-1 K-1)	0.8	0.8	0.8
thermal conductivity of ground (road) (W m-1 K-1)	1.32	1.32	1.32
Surface albedo of roof	0.2	0.15	0.2
surface albedo of building wall	0.2	0.15	0.2
surface albedo of ground (road)	0.11	0.11	0.11
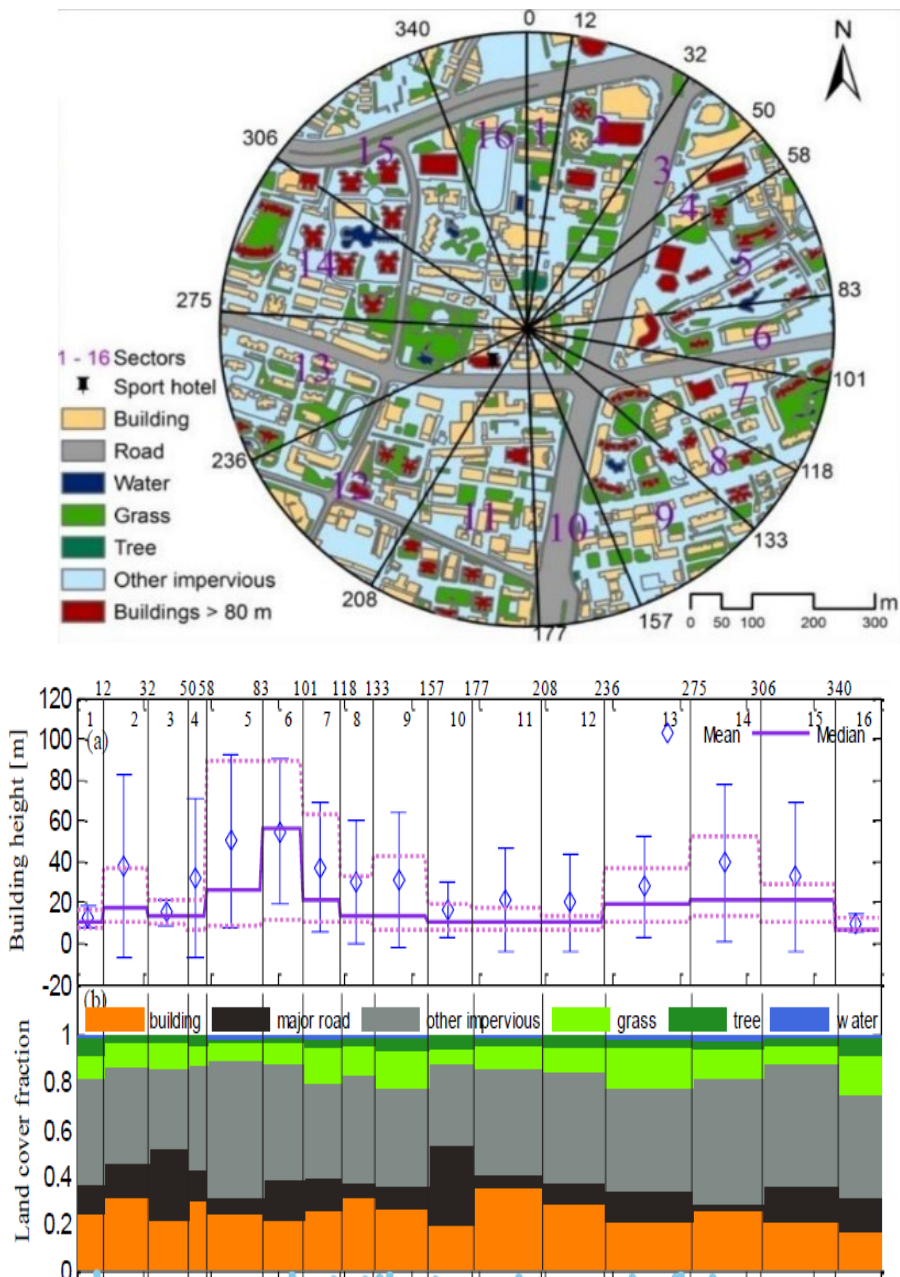
Figure 4.3 Building Radial distribution in 500m from Shanghai Meteorological Bureau (Tan et al., 2016)

There are insufficient resources available to obtain all the building height and distribution information in Shanghai, and therefore, a SLUCM is used in parameterize Shanghai area. Tan and Grimond published a paper about Shanghai's Urban Integrated Meteorological Observation Network in 2015 by digitalized an $80000m^2$ building height in shanghai downtown area as is seen in Figure 4.3. It must be taken into account

that the LULC scheme is not only used in the core city, which means it is not only the core city being characterized as High-density residential area in this simulation. Therefore, some parameters should also be adjusted to fit more in our simulation. Table 4.1 lists most important Urban surface parameters used, including other key parameters such as Mean building height, Standard deviation of building height and AH maximum level. The remaining parameters have been set as default as per the recommendations of various other researchers (Ahmed et al., 2015; Salleh et al., 2015; Tan et al., 2016).

Anthropogenic heat is mainly produced by human production and living and biological metabolism. Due to the high population density in cities, heat released by fossil fuels comprises of that in the combustion of gas stoves and internal combustion engines in industrial production, by air temperature regulating equipment and motor vehicle exhausts, amongst others. The effect of anthropogenic heat on urban heat balance is influenced by many factors, such as the geographical location of the city, the size of the construction scale of the city, the level of population density, the level of energy consumption per person, the nature of the city and its regional climate conditions, and other obvious seasonal and diurnal variations. (Wang et al., 2011; Lu et al., 2014)

In this research paper, anthropogenic heat emission sources are considered from industry, transportation, construction, and human metabolism with each contribution estimated in table 4.3(Li et al., 2015). To further substantiate the findings of the simulation, a diurnal profile of AH emission has been included.

Table 4.3 Estimated Anthropogenic Heat Flux

City	Area (km^2)	Anthropogenic Heat ($\times 10^6 J/A$)				Average Flux (W/m^2)
		Industry	Transport	Building	metabolism	
Shanghai	866	173.7	87.3	49.9	10	120
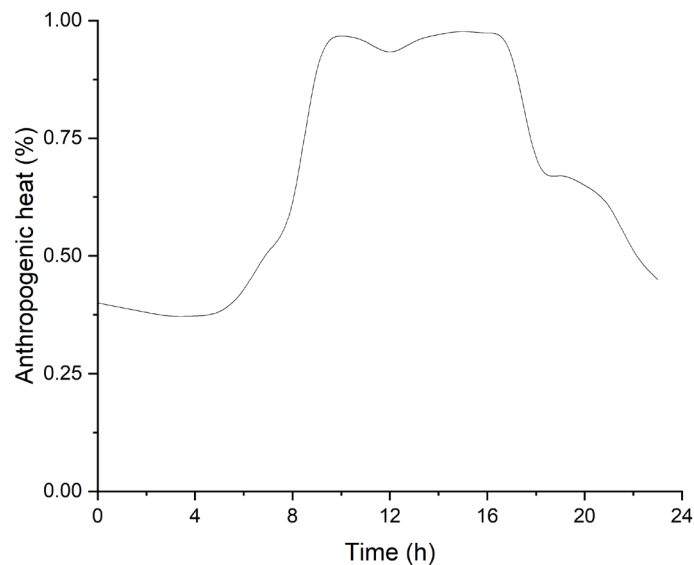
Figure 4.4 The diurnal profile of AH intensity used in the UCM

For simulation lateral boundary conditions, data from the National Centres for Environmental Prediction Final Analysis data is used. The data is on 0.25-degree resolution of each grid cell generated by each six hours. The Global Data Assimilation System, which continuously collects observational data from the Global Telecommunications System is used to help assimilate the product to increase its accuracy (NCEP et al., 2000).

Observation data used is Hourly Data from Surface Meteorological Stations in China. In this case, there are 11 national observation stations in Shanghai and the real time data are quality controlled at an overall 99% accuracy standard. Observation

60

stations information can be found in table 4.4 and Figure 4.4. Model validations and analyses are conducted using this observation data on corresponding results from d03, unless stated otherwise.

Table 4.4 Observation stations information

Station Name	Station ID	Longitude (°)	Latitude (°)	Elevation (m)
Minhang	58361	31.10	121.37	5.5
Baoshan	58362	31.40	121.45	5.5
Jiading	58365	31.37	121.25	4.4
Chongming	58366	31.67	121.50	4.3
Xujiahui	58367	31.20	121.43	4.6
Nanhui	58369	31.05	121.78	5.0
Pudong	58370	31.23	121.53	4.4
Jinshan	58460	30.82	121.27	-
Qingpu	58461	31.13	121.12	4.0
Songjiang	58462	31.03	121.23	4.2
Fengxian	58463	30.88	121.50	4.6

Figure 4.5 Observation station locations

4.3 Model validation

Numerical modelling has the advantage of being able to support simulations in different scenarios and easy to alter settings for different research interests, while its inherent limitation is non-neglectable, such as lack of complexity of real -world characteristics, and an over simplified physical process model in theoretical assumptions. Thus, validation of this WRF/NOAH/UCM combination on its ability to capture meteorology characteristic of our research is necessary before more scenarios are introduced for further study.

2-m temperature (T2m), 2-m relative humidity (RH) and wind speed (WS10m) generated during simulation period is validated against network of all 11 Observation stations (result generated during first 12hours are abandoned as spin hour data). Five statistics tools are used at this stage, namely: Mean Bias Error (MBE), root-mean square

error (RMSE), hit rate (HR) and Index of Agreement (IOA).

MBE is calculated as

$$MB = \frac{1}{N}\sum_{i=1}^{N}(P_i - O_i)$$

where Pi is the modelled value for station i, Oi is the observed value, and N is the number of values analysed.

IOA is calculated as

$$IOA = 1 - \frac{\sum_{i=1}^{N}(P_i - O_i)^2}{\sum_{i=1}^{N}(|P_i - \bar{O}| + |O_i - \bar{O}|)^2}$$

Index of Agreement (IoA) provides further insight into the behaviour of the model for scalar magnitudes. It ranges from 0 to 1, (0<IoA<1)

HR is calculated as

$$HR = \frac{1}{N} \times num(|P_i - O_i| < C)$$

C as the threshold value is set as 1.0°C (Cox et al., 1998) for 2-m temperature, 1.0 m/s (Kulkarni et al., 2008) for 10-m wind speed and 5% (Lawrence 2005) for relative humidity as the desired accuracy (hit-rate).

RMSE is calculated as

$$RMSE = \sqrt{\frac{1}{N}\sum_{i=1}^{N}(P_i - O_i)^2}$$

Table 4.5 Statistical summary of model validation for different cases

Variables	Statistics Indicators	MODIS	URB_noAH	URB	CONTROL
T2m (°C)	MB	-2.074	-0.39	0.269	-2.569
	RMSE	2.244	1.546	1.512	2.823
	IOA	0.854	0.991	0.993	0.852
	HR	0.46	1	1	0.50
RH (%)	MB	7.087	2.411	-2.18	8.319
	RMSE	8.428	5.347	4.712	9.292
	IOA	0.885	0.933	0.936	0.913
	HR	0.66	0.83	0.88	0.125
WS10m (ms^{-1})	MB	1.128	0.418	0.306	1.175
	RMSE	1.192	0.995	0.918	1.285
	IOA	0.335	0.634	0.715	0.138
	HR	0.41	0.92	0.92	0.38

Statistics of model validation for all 4 different cases are summarized in table 4.5. Generally, the WRF/NOAH/UCM combination model yields a good performance for 2-m temperature, 2-m relative humidity, and 10-m wind speed as our main indexes of evaluation. This is particularly the case for case b - URB, which uses the updated land use and land cover map along with an estimated AH emission diurnal curve. The IOA for case b - URB is 0.993, 0.976 and 0.815 for T2m, RH and WS10m, respectively.

Regarding the T2m simulation, cold bias can be found in the case of MODIS, URB_noAH and CONTROL case as there is no urban land cover. It is noticeable that even for the cold bias, URB_noah shows a relatively low value of the cold bias (-0.39) compared to the MODIS case (-2.074), which indicates that the updated LULC map is able to correct the underestimated urban area in MODIS 2001 dataset. The only warm

bias comes when the AH emission is taken into consideration in case b - URB. The introduction of SLUCM and updated LULC yields a better result when looking at RMSE and IOA considered with that of MODIS case. RMSE is reduced from 2.244 to 1.546 and 1.512, IOA is increased from 0.854 to 0.991 and 0.993, without and with AH respectively.

Similar result can be found in terms of RH simulation. Positive bias is reduced when updated LULC map and SLUCM is employed in case c - URB_noAH, from a large mean bias of 7.078 to 2.411, and further turns into a negative bias of -2.18 in case b - URB when the AH emission is taken into account. This result makes sense as the rapidly change of land cover from croplands and forest into impermeable artificial underlying surface in Shanghai is observed since 2001, when MODIS data was generated. An improvement can be inferred by a 5.081 and 5.168 ˚C reduce of RMSE of 2-m temperature for URB_noAH case and URB case, respectively. It is noticeable that most observation stations located on MODIS 2001 map are classified as cropland, which is not consistent with reality. All cases therefore overestimate the wind speed in the simulations while the case b. URB still presents the most accurate results out of 4 with a RMSE at 0.918 m/s and a IOA of 0.715.
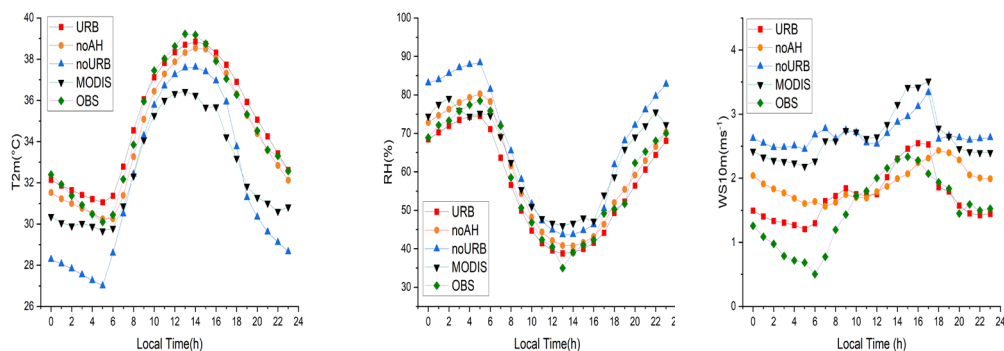
Figure 4.6 Average diurnal profile of (a) 2-m temperature (left), (b) Relative humidity (middle), (c) Wind speed (right)

The update of urban underlying surface datasets is helpful to input updated surface albedo, radiation, roughness, and other parameters, which is more consistent with present reality, and thus has an impact on the simulation of water vapor and energy balance in the land-surface scheme.

In addition, the introduction of UCM and AH enables the model to consider simple building morphological characteristics, and the shading effect among buildings to establish energy balance equations on the roof, wall, and road surface. The improvement of the simulations' results is clearly demonstrated diurnally in Fig 4.6.

For 2m-temprature, 1700 – 0700 local time simulation indicates that the AH is playing an important role in heating the surface, leading a slower temperature drop before the sunrise. Temperature rises rapidly during daytime and reaches its peak at 1300 when the radiation is dominant all the energy balance equation. All simulation fail to capture temperatures as extreme as 39.225°C but the URB case can be seen as coming the closest. MODIS case is able to capture the trend of temperature diurnal curve but the outdated LULC distribution leads to a systematic underestimated of T2m. The increase in simulated surface temperature also results in a reduction of relative humidity of Shanghai area, which led to an underestimation of the relative humidity during the simulation period. (Figure 4.6b). Due to updated urban land cover information such as building height and roughness length in the simulation, wind speed simulated for both URB case is lower than MODIS and noURB. However, overestimated wind speed during 0000 – 1000 is observed for all cases.

Overall, land-use dataset update setting (URB_noAH) and with AH parameterization setting (URB) increases WRF simulation performance, with AH added case is having best result with a RMSE at 0.512°C, 4.712 and 0.918ms-1 for 2-m temperature, 2-m relative humidity and 10-m wind speed, respectively.

In the further research of this chapter, Case b - URB is used to study the climatology of Shanghai city. Spatio-temporal distribution of temperature, humidity, wind speed, energy budget and planetary boundary layer height will be the next topics discussed.

4.4   Results and discussions

4.4.1 2-m Temperature and Urban heat island intensity

As demonstrated above, diurnal profile of average 2-m temperature is shown in Figure 4.6, while Figure 4.7 indicates it also has a spatial distribution pattern dependent upon the land cover and human activities. 3 typical intervals can be classified according to Figure 4.7a (Morning before sun rise: 0100 – 0500 LT, daytime when sun rises: 0700 – 1400 LT, and night time after sunset: 1800 – 2400 LT). 2-m temperature is dropping in the morning with different pace as rural area reaches its lowest temperature at 27.56°C, followed by LIR at 29.78°C and HIR at 31.05°C. AH emission plays a dominant role in heating the surface when there is no direct sun radiation. At daytime, surface temperatures would start increasing naturally after sunrise until reaching the maximum temperature at 38.85°C, 38.30°C and 37.91°C for HIR, LIR and rural areas respectively. Although the temperature distribution gradient is maintained in the simulation, it is clear that the maximum temperature is relatively closed. Within the first 6 hours of sunrise, T2m of rural area experiences a surge for 10.4°C, while that of the HIR for 7.8°C only. Large areas of artificial underlays in cities, such as impermeable roads and roofs, absorb more heat than vegetation in suburban areas, which slows down the temperature rise of urban areas directly exposed to sunlight during daytime and slowly releases the heat back after sunset. This can be verified by the night time curve of Figure 4.7a as a similar process of that in the morning. Overall, HIR with higher fraction of urban area shows the highest max temperature(38.85°C) but lowest Diurnal temperature range(7.8°C), as opposed to rural spaces that come with 37.91°C max and

10.4°C range, with LIR in the middle of all indicators (38.3°C maximum and 8.52°C range).
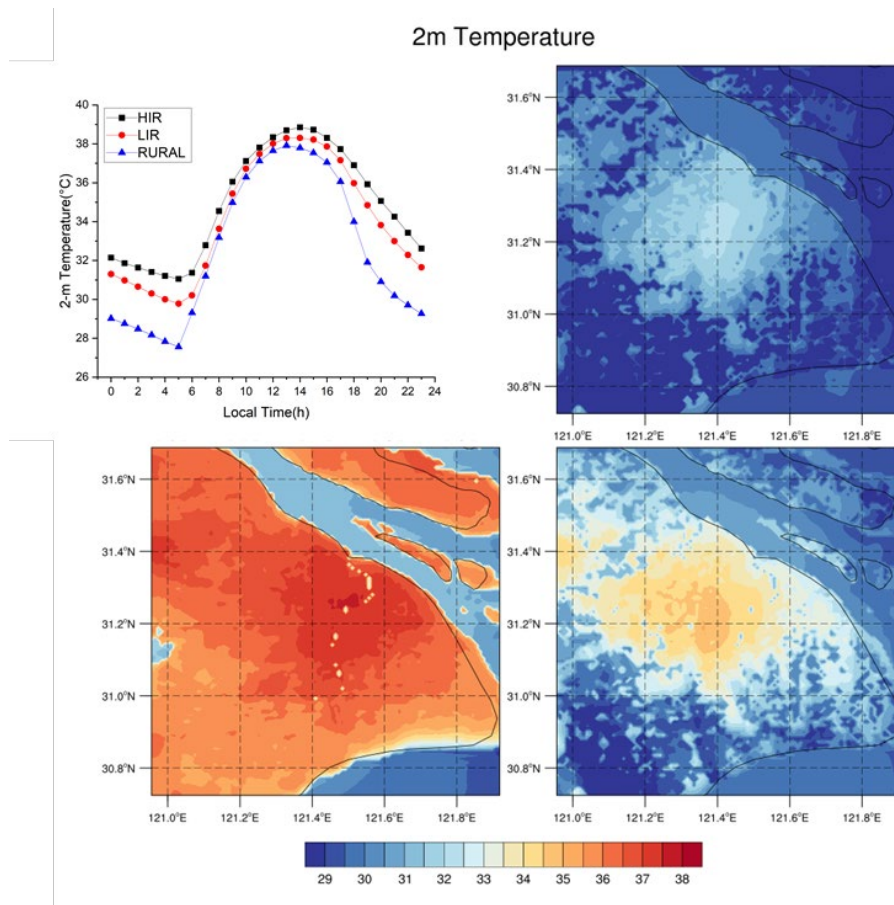
Figure 4.7 Averaged temporal variations of: (a) 2-m temperature (up left figure) and Spatiotemporal variation of 2-m temperature above the surface during: (b) morning (up right figure), (c) day time (bottom left figure) and (d) night time (bottom right figure)

Fig 4.7 bcd shows the spatial distribution of 2m temperature at different stages. The temperature distribution after sunrise shows no obvious difference among 3 underlying surfaces. The maximum temperature appears in the northwest direction of Huangpu River and gradually decreases towards the coastline. However, the temperature distribution after sunset reflects the obvious influence of underlying surface, which is more significant in 0000-0500 LST stage. It can be clearly seen that there is a certain degree of cliff in the temperature distribution, and the temperature gradient at the edge

of the high temperature area is large. It is posited that this is a result of the oversimplified introduction of AH emission, with no consideration of continuous distribution in the boundary area of 2 different land cover types.
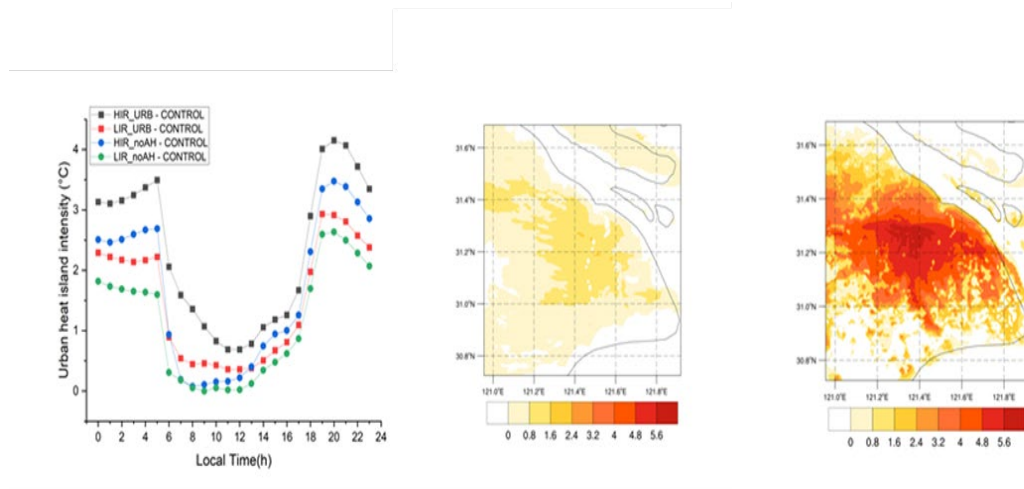
Figure 4.8 (a) Averaged temporal variations of UHII (left figure) Spatiotemporal variation of 2-m temperature above the surface during (b) day time (middle figure), (c) night time (right figure)

The UHI distribution is calculated by result of case a. URB minus results of CONTROL case. Results representing purely temperature rise due to urbanization can be observed in such idealistic experiments design. Another idealistic experiment using case c. URB_noAH minus case d. noURB is carried out to evaluate the UHII without the AH emission. By comparing the results, contribution to UHII from AH can be inferred.

Fig 4.8a summarises the diurnal profile of UHII for 2 different land cover type. Results indicate that stronger effect of Urban heat island can be found during night time than daytime. The peak value of UHI occurs at time around 2000LST with a maximum magnitude of 4.15°C and 2.93°C for HIR and LIR, respectively. In the next few hours, the urban heat island effect has been largely slowed down and maintains a relatively stable level before sunrise (3.13 to 3.37 for HIR and 2.22 to 2.29 for LIR). Immediately,

during the daytime when the solar radiation is heating the whole surface, UHII decreases fast and reaches its lowest level around 1200LST with a value of 0.68 for HIR and 0.36 for LIR.

The contribution of AH for UHI can be inferred from Figure4.9a as well. During daytime, an average contribution of 69%(HIR) and 76%(LIR) is made by AH emission while that percentage drops to 20%(HIR) and 19.7%(LIR) at night and over all 36% and 39% for HIR and LIR, respectively. The contribution of AH to the UHI intensity in this study is comparable with those described by Wang et al., (2013a) (34% in the Beijing–Tianjin–Hebei metropolitan area) and Feng et al., (2012) (31% in the Yangtze River delta region).

Fig 4.8b and c shows the spatial distribution when a lowest and highest UHII occurs in simulation period. It is clear that UHI distribution is dependent on urban land-use type and is preponderant during night time when strong UHI is observed as seen in Figure 4.8c. The centre of UHI is located in HIR and its intensity rapidly decrease to LIR and rural area in descending order of magnitudes. It is however much less significant in the case of daytime UHI like Figure 4.8b shows. The margin of UHI level is not consistent with LULC map of HIR and LIR, and there is less hierarchy of UHII like Figure 4.8c. During daytime, the surface is heated by direct solar radiation and atmospheric longwave fluxes, which dominates the fluxes over both rural and urban landcover with almost equal energy heating the whole Shanghai city; this leads to a reduction of thermal different between surfaces, which also explains the results in Figure4.7a where temperature for all surfaces is rising rapidly. It is natural that the dominant of direct sun radiation ends after sunset and re-radiation of absorbed fluxes plays a more important role at night time.

The most notable feature of the urbanization process is that the underlying surface

changes from vegetation to urban areas. In this process, many physical parameters such as albedo and heat capacity have changed. Lower urban surface albedos and higher heat capacity of urban landcover result in higher heat retention relative to the vegetated areas, which is released to the atmosphere at night time. What is more significant is the shortwaves radiation absorption and trapping effect by the urban surfaces and buildings are also taken into consideration in single layer urban canopy model. The AH emission amplifies such an effect and pushes the UHII to reach its maximum magnitude during night time.

4.4.2 Urban surface energy balance and PBLH
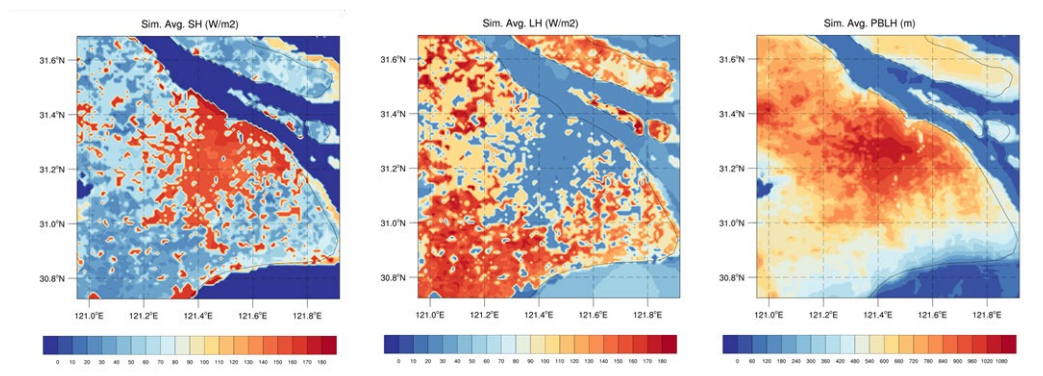
Figure 4.9 Averaged (a) Sensible heat flux – SH (left figure) in Wm^{-2}, (b) Latent heat flux – LH (middle figure) in Wm^{-2} and (c) PBLH in m (right figure)

Fig. 4.9 shows a simulated average of both sensible and latent heat fluxes and planetary boundary layer height above Shanghai during the investigated period. Spatial distribution of LH, SH and PBLH can be seen clearly on the model domain, with different areas showing a great difference. HIR has an average sensible heat flux of 161.7 Wm^{-2}, while the rural area shows the least sensible average flux with a mean magnitude of 39.5 Wm^{-2}. In contrast, the average latent fluxes of 234 Wm^{-2} and 148.3

Wm^{-2} are observed for HIR and rural areas, respectively (66.5 Wm^{-2} averaged SH and 102.5 Wm^{-2} for LIR). The surface energy budget was modified due to urbanization process, as the increase in impervious subsurface in urban areas reduces moisture presence, thereby reducing evaporation and latent heat intensity. On the other hand, this increase of artificial material leads to a larger temperature difference between the surface lying and the atmosphere in city area, which causes energy flux to show as sensible heat flux.
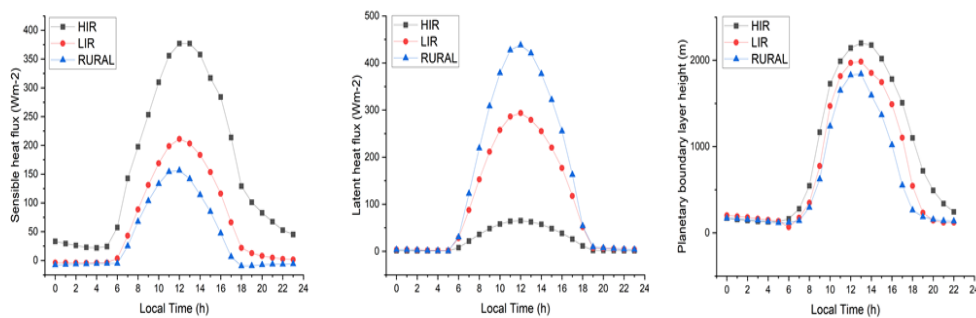
Figure 4.10 Averaged temporal variations of: (a) sensible heat flux (left figure), (b) latent heat flux (middle figure), (c) Planetary boundary layer hight (right figure)

As for the diurnal profile of sensible and latent heat, the variance from different land cover types also can be noticed. Latent heat flux is observed to maintain at a stable level for all 3 area in the morning before the sunrise (0 – 9.8 Wm^{-2}), while the sensible heat flux is relatively higher than the other 2 land cover at around 44 Wm^{-2}. Nonetheless, the SH benefits greatly from the increase in urban surfaces, which cause rapid changes in heat content of the surfaces during solar irradiance. Highest sensible heat flux level can be observed during 1200LST to 1300LST with value of 378.5 Wm^{-2}, 201.3 Wm^{-2} and 149.6 Wm^{-2} for HIR, LIR and Rural, followed by a dive in all magnitude. This is reasonable as sensible heat comes only comes from shortwaves solar radiation and atmospheric longwave fluxes, and temperature difference between ground and atmosphere is decrease gradually from 1400LST, and eventually drops to the lowest

72

during the night. For HIR the sensible heat flux is still observed with a value of 44 Wm^{-2} due to the AH emission that must be taken into consideration even at night time which constantly heats the atmosphere.

Similar processes can be found in terms of PBLH shown in Figure 4.10 c. After sunrise, shortwave solar radiations and atmospheric longwave fluxes is the heat the Earth's surface receives, leading to a rise in surface temperature for all land cover types, and as a result causes vertical and horizontal transport of the heat fluxes (SH). After that, an increase of evaporation from surface moisture and transpiration from vegetation begins, which is then transported by wind (LH) into the canopy layer as the lower boundary layer above the surface. These interactions of the solar radiation, atmospheric longwave fluxes, sensible heat flux and latent heat fluxes affect the temporal growth of the PBLH. A higher proportion of urban coverage and AH intensity amplifies this effect, thus a number of over 2300m of the maximum PBLH can be found for HIR area during 1200LST to1300LST, while that of LIR and rural areas are just 1987m and1664m, respectively. During morning before sunset, the three land classes have a near-stable PBLH around 195 m, however the HIR area has a much higher value after the sunrise, which is different from other 2 land cover types. This is likely the heat energy retained during daytime which has re-radiated into the urban canopy layer after sunset, providing the fluxes to maintain a deeper PBL height. Likewise for the case of SH and LH – from the average PBLH representation in Figure. 4.9c, land cover spatial characteristic can be observed in the PBLH spatial distribution, with a decreasing magnitude corresponding to a decreasing urban fraction.

4.4.3 Wind speed and Relative humidity
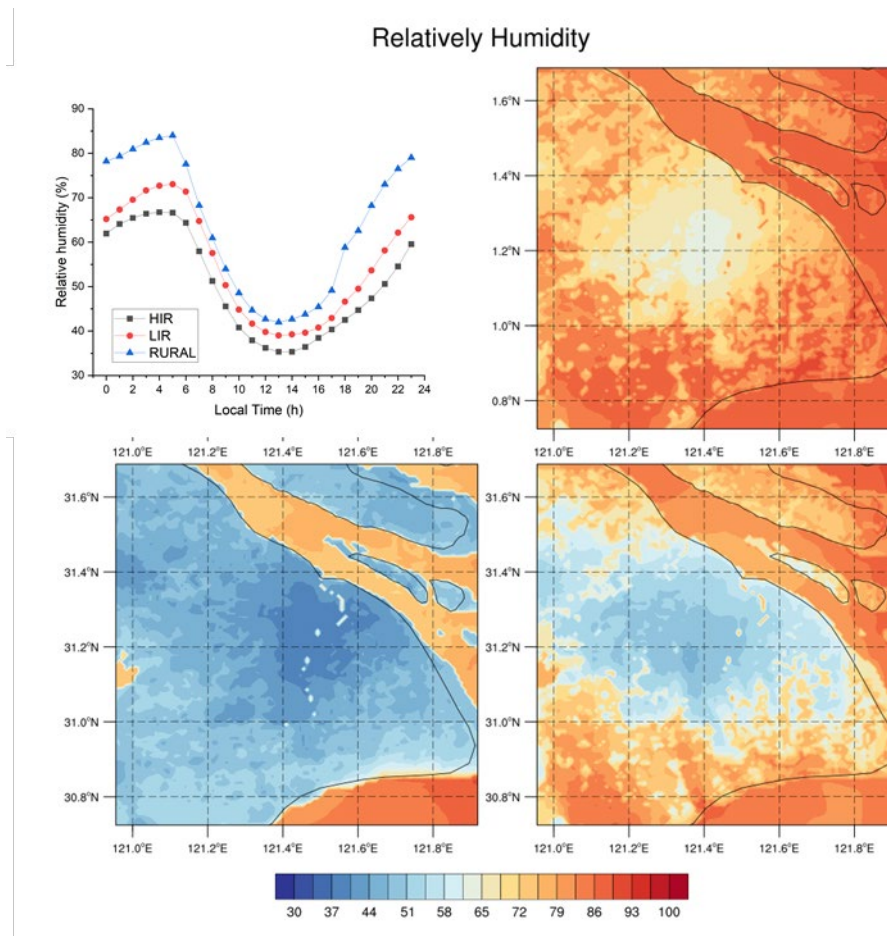
Figure 4.11 Averaged temporal variations of: (a)Relatively humidity (up left figure) and Spatiotemporal variation of RH above the surface during: (b) morning (up right figure), (c) day time (bottom left figure) and (d) night time (bottom right figure)

Just like the heat island effect, the urban dry island of Shanghai is also fully reflected in this simulation. As the main body of the city is reinforced by a concrete impermeable underlying surface, most of the water falling on the ground is drained to other places through artificial laid pipes, lacking the absorption and storage capacity of soil and vegetation that the natural ground has. As a result, the air near the surface of a city is not constantly replenished by the evaporation of soil and vegetation as it is in other natural areas (Kratzer 1956; Lokoshchenko 2014). Consequently, cities have less

moisture and lower humidity in the air, creating "dry islands" isolated from surrounding areas, as is demonstrated in Figure 4.11.

In addition to the impact of surface underlying, daily solar radiation has a direct effect on the relative humidity. After sunrise, the relative humidity of the three kinds of underlying surfaces begins to drop rapidly from their maximum values (66.6 for HIR, 73 for LIR and 84 for rural area) until reaching its lowest level at about 1400LST at noon, followed by a gradual increase. It is worth noting that after sunset, the relative humidity increases faster in the rural area, which is due to the more obvious temperature drop in the suburbs and more abundant water vapor in the air, while HIR and LIR do not show such changes due to more impervious underlying surface coverage. Urban dry island effect is also a change in residents' living environment caused by urbanization, which is coupled with urban heat island effect and affects residents' health (Wang et al., 2010).

The distribution of wind field in Shanghai is complex as Shanghai is located in the centre of the north and south coast at the confluence of Yangtze River and Huangpu River. It is thus difficult to simulate the wind field due to the combined influence of land-sea breeze and heat island effect.

The following figures shows the wind field distribution at two different typical moments. As shown in Figure 4.12a, it can be clearly seen that the temperature on the land surface is higher than that on the sea surface, resulting in the surface pressure being lower than that on the sea surface, forming a relatively strong sea and land breeze blowing from the sea to the land. Additionally, the lake breeze from Lake Taihu can be observed in the west due to pressure difference. The coupling of such mesoscale effects adds greater difficulty to precisely simulate the wind field of Shanghai area.
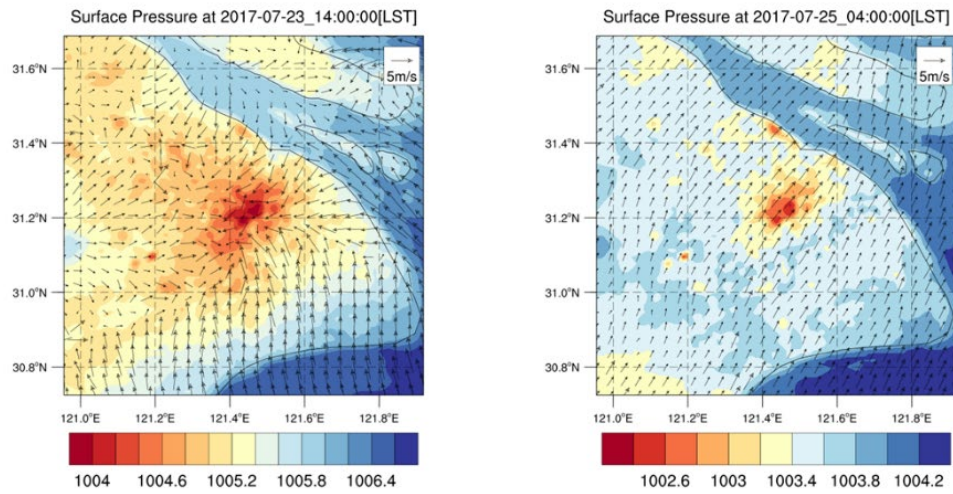
Figure 4.12 Surface pressure and wind field for: (a) 1400 LST (left figure), (b) 0400 LST (right figure)

During the night, the specific heat capacity of sea water is much higher than that of the urban area of Shanghai, resulting in a relatively rapid cooling of the urban area. At this time, the sea and land breeze blow from the land to the sea. However, due to the existence of heat island effect, there will still be some areas in the main urban area of Shanghai with a high temperature, which influences the distribution of land sea breeze wind field.

In general, while the wind field simulation does not fully reflect reality, it can still reflect the typical situation of the complex wind field distribution in Shanghai to a certain extent, in particular the UHI affecting the land- sea breeze which can be clearly shown from simulation results.

4.5 Conclusion

In this study, the effect of LULC dataset and anthropogenic heat parameterization on the performance of coupled model systems (WRF / Noah / UCM) were examined. The simulation results shows that the introducing of AH and elaborative LULC dataset does significantly improve the model prediction of atmospheric and surface meteorology. The comparison between the simulation results and the observation data shows that the model has the ability and is sufficiently suitable to reproduce the regional meteorological parameters of Shanghai and can continue to be used in the current research.

The influence of urbanization on meteorology characteristic in Shanghai has also been canvassed. Further simulation results shows that the environmental conditions in this area have changed due to urbanization. For example, the average relative humidity and latent heat flux in urban areas are lower compared to the rural space. On the contrary, the impact of urbanization also significantly increases the average planetary boundary layer height, sensible heat flux, 2-m temperature, and urban heat island intensity.

The transformation of vegetation to urban surface changes the surface energy balance of local environment and the spatial distribution of PBLH and UHII. For instance, planetary boundary layer height, sensible heat flux, 2-m temperature, and urban heat island intensity decreases radially from the urban centre to the minimum near the least developed areas. However, relative humidity and latent heat flux increased radially away from the city centre. In terms of diurnal profile, the impact of urbanization on the heat island effect in Shanghai is dominant after sunset, and then decreases to the minimum during the day to reaches its lowest level at noon. In addition, the intensity of urbanization, solar radiation and periodic sea land wind have an

77

important impact on the temporal and spatial distribution of meteorological parameters.

The simulation shows the impact of urbanization on environmental meteorology in Shanghai. The increase of urban buildings and decrease of vegetation is one of the reasons for the average temperature rising and the formation of both urban heat island and uber dry island. This means efforts must be made to increase the vegetation fraction in urban areas to mitigate said effect.

The results also implies that uniformed parameterization of single layer urban canopy likely has an impact on the validation of the model. In addition, the current research does not consider the impact of urban design and building structure in detail, and therefore, simulation of wind field is not as accurate as the observation data. Further research should be carried out in this respect.

5 Urbanization of Shanghai and its impact on local climate since 21st century

5.1 Introduction

With the rapid development of China's economy, the world's economic centre is increasingly shifting to China. Urbanization is not only the basis and driving force of economic development, but also the inevitable choice and final result of economic development. Since the reform and opening up, China's urbanization has been significantly accelerated, with the urbanization rate growing at an annual rate of 1%. In 1978, There were only 193 cities in China, but by the end of 2017, the number of cities in China has increased to 661 (Mohurd, 2017). Meanwhile, China has also formed three major urban agglomerations: the Yangtze River Delta, the Pearl River Delta and the Beijing-Tianjin-Hebei region. As the core city of the Yangtze River Delta city group, Shanghai is also the economic, financial, and technological centre of China. The rapid economic development has been accelerating the urbanization process in Shanghai, attracting a large number of people. By the end of 2017, the permanent resident population of Shanghai has reached 24.18 million (Shanghai Statistical Yearbook, 2018). Nowadays, the urbanization rate of Shanghai exceeds 70%, making it one of the cities with the highest urbanization degree in China (Yu et al., 2019). The improvement of urbanization level has also led to earth-shaking changes in the local land use structure, which has changed the physical properties of underlying surface and affected the local weather and climate characteristics. Compared with the suburbs, the drainage system in the city is more developed, and the ground material is mostly asphalt or cement, which leads to the high impermeability of the city. The density of urban buildings and the building height leads to an increase of urban surface roughness. At the same time, the interior of the city has a more complex geometry than the suburbs and the radiation

reflect multiple times between buildings, forming a "capture" effect. All of these characteristics make the energy budget in the city significantly different from that in the suburbs, so there are significant temperature differences between the suburban area and downtown area (Balling et al., 1988; Cai et al., 2003). Studies show that the enhancement of urban surface heat island is mainly caused by land use change (Chen et al., 2013), and there is a significant positive correlation between surface temperature and built-up area (Cao et al., 2013; Shi et al., 2018).Taking Shanghai as an example, during the 30 years from 1984 to 2014, the urban area of Shanghai increased by 994 km^2, while the temperature in some areas rose by 81% (Zhao et al., 2016). Many people have made detailed analyses on this aspect based on observation data. For example, Shen et al. (2014) based on observation data from 1994 to 2014, concluded that sea-land temperature difference gradually decreased, which weakened sea-land wind in Shanghai with the development of urbanization. Also, by comparing the observation data since 1916, Liang and Ding (2014) obtained the fact that the frequency of heavy precipitation in Shanghai increased with the development of urbanization. However, few people realize the fact that statistical data analysis not only reflect the influence of the urbanization of Shanghai, also includes the background of the impact of global warming. And due to the fixed location of observation stations, the clear boundary between suburbs and cities cannot be accurately grasped, so the calculation of UHII is not rigorous enough.

In view of such a gap in the research, four ideal experiments are designed in this chapter to represent the urbanization development process of Shanghai in 2000, 2010 and 2017 by replacing LULC data set and AH Settings (no urban scenario as fourth case). Sensitivity analyses are conducted based on the simulation results, aiming to exclude the influence of global warming background. And to explore the impact of the

urbanization development process in Shanghai on local climate (near surface humidity, near-surface temperature, and wind speed) and human comfort.

5.2 Methodologies

In this study, different materials and methods are used to adapt to different simulation situations. Land use and land cover datasets for 2000, 2010 and 2017 are converted into MODIS 33-category classification system as replacement of WPS default static dataset. By comparing the data sets of land use and land cover in 2000, 2010 and 2017, three cases representing the urbanization process of Shanghai since the 21st century is simulated under same other settings. NCEP generated Global Final reanalysis data in the resolution of 0.25° x 0.25° are used as the initial and lateral boundary conditions of the simulation. The initial conditions are updated in every 6 hours (NCEP, 2000).

In addition, before starting the case study simulation, an observation data network is used to evaluate the performance of the model. The observation data of 11 observation stations located in different area of Shanghai and simulation results are compared.

Finally, by coupling WRF/NOAH/UCM, a set of sensitivity experiments investigating the impact of urban expansion and urbanization on local climate are carried out.

5.2.1 Study area

Situated at 120° 51' E - 122° 12' E and 30° 40' N - 31° 53' N, Shanghai lies on the west coast of the Pacific Ocean and the east coast of the Asian continent, at the central point of China's north and south coast, at the confluence of the Yangtze River and the Qiantang River into the sea. Additionally, Shanghai borders the Yangtze River to the north, the East China Sea to the east, Hangzhou Bay to the south, and Jiangsu and

Zhejiang provinces to the west. It has an inland coastline of nearly 172 kilometres long, and boasts a superior geographical location, convenient transport facilities, and fantastic river and seaports. It is approximately 120km long from north to south and 140km wide from east to west. At the mouth of the Yangtze River to the north of Shanghai, there lie three islands: Chongming, Changxing and Hengsha (Ren et al., 1991; Yuan et al., 2004; Nie et al., 2006). Shanghai has the northern subtropical monsoon climate, with mild humidity, noticeable monsoon, and abundant rainfall (Gu et al., 2007; Da et al., 2004). According to statistics, Shanghai has an annual average temperature of 15.2-15.9°C, and the coldest month has an average temperature of 3.1-3.9°C, while the hottest month has an average temperature of 27.2-27.8°C (National Climatology centre, 2021). The annual average precipitation is 1048-1138mm, with 129-136 days of annual precipitation and 228 days of annual frost-free. The prevailing wind direction in Shanghai demonstrates an obvious seasonal change: the southeast wind prevails in spring and summer, and the northeast and northwest wind haunts in autumn and winter. The dominating wind directions throughout the year are the east and southeast wind (Mu et al., 2008; Hou et al., 2008).

Shanghai has the highest population density in China and is one of the most dynamic economic zones in the world. In 2020, Shanghai's GDP reached 3,870 billion yuan (Shanghai Municipal Statistics Bureau, 2021), accounting for 2.4% of China's total. Administratively equivalent to a province, it is divided into 18 county-level districts: 17 districts and one county, nine of which the urban core area collectively known as the downtown area, namely the Huangpu, Luwan, Xuhui, Changning, Jing'an, Putuo, Zhabe, Hongkou, and Yangpu. Other nine area located far away from downtown are Baoshan, Minhang, Jiading, Jinshan, Songjiang, Qingpu, Fengxian, Pudong, and Chongming island. There are 11 weather stations in Shanghai, as shown in Figure 5.1.
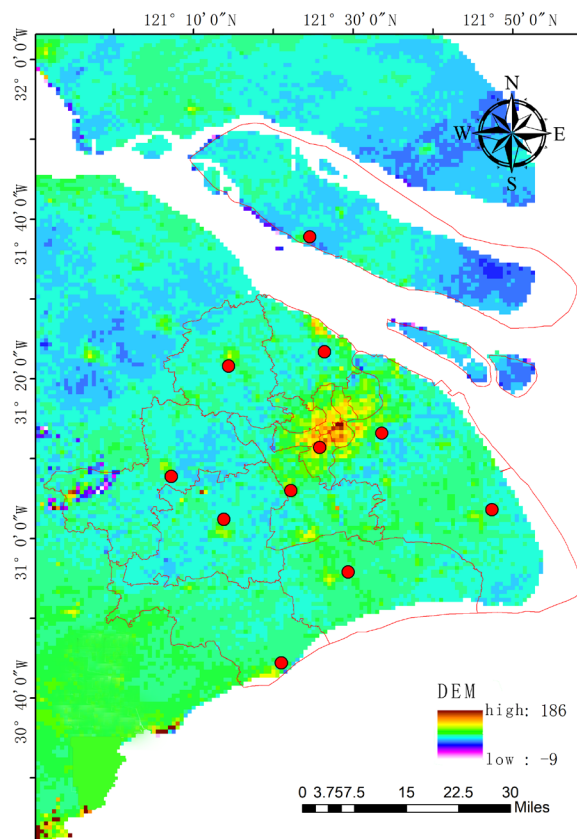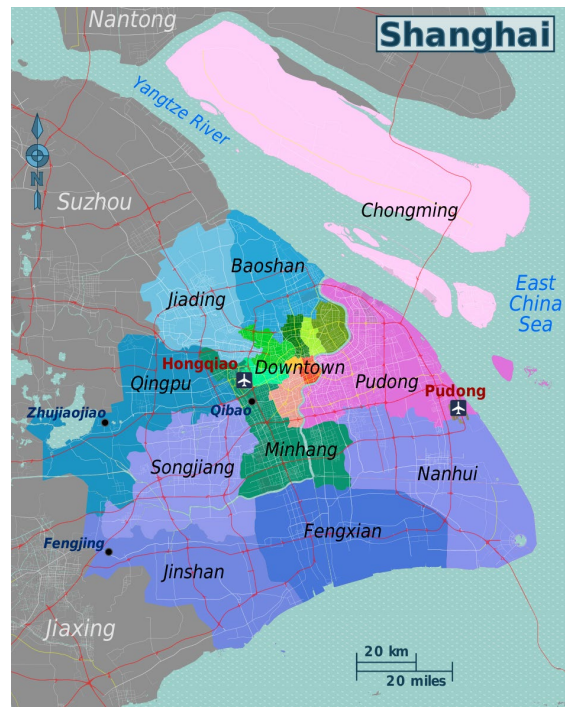
Figure 5.1 Administrative Divisions of Shanghai

Shanghai has seen rapid urbanization and infrastructural development. Natural vegetation and environmental surface energy balance in cities have been replaced by

asphalt engineering surfaces, and most materials used in the construction of roads, high-rise buildings and recreational facilities have low reflectivity and low surface albedo (Ahmed et al.,2015). Air flow, temperature distribution, momentum exchange, heat and moisture in cities are all affected by anthropogenic surface changes. Moreover, emissions from heavy machinery, cars and air conditioning units only add to Shanghai's environmental problems (Zhao et al., 2006). Urbanization in the region has led to an increase in the number of people living in cities and a corresponding increase in human factors (Moser 2010). It is therefore important to observe the development of urban heat islands through urbanization.

5.2.2 Model and experimental design

Simulation is conducted using WRF-ARW dynamic core (Skamarock et al., 2008) coupled to NOAH land surface model (Chen & Dudhia 2001; Tewari et al., 2007) with the urban canopy model (Kusaka & Kimura 2004; Chen et al., 2011). WRF is not a statistically balanced but compressible model which uses large-scale coordinate systems. Although WRF is designed as a numerical weather prediction model, it can also be used as a regional climate model. Noah LSM, as a coupled atmospheric model for lower boundary layer conditions, has a basic function of providing surface sensible heat, latent heat flux and surface temperature. It is based on a diurnal Penman potential evaporation method, multi-layer soil model, a complex canopy resistance parameter, surface water literature and frozen soil physics (Chen et al., 1997; Chen and Dudhia, 2001; Eket et al., 2003). Variables calculated include temperature in the soil layer, water stored in the plant canopy and snow water equivalent stored in the ground.
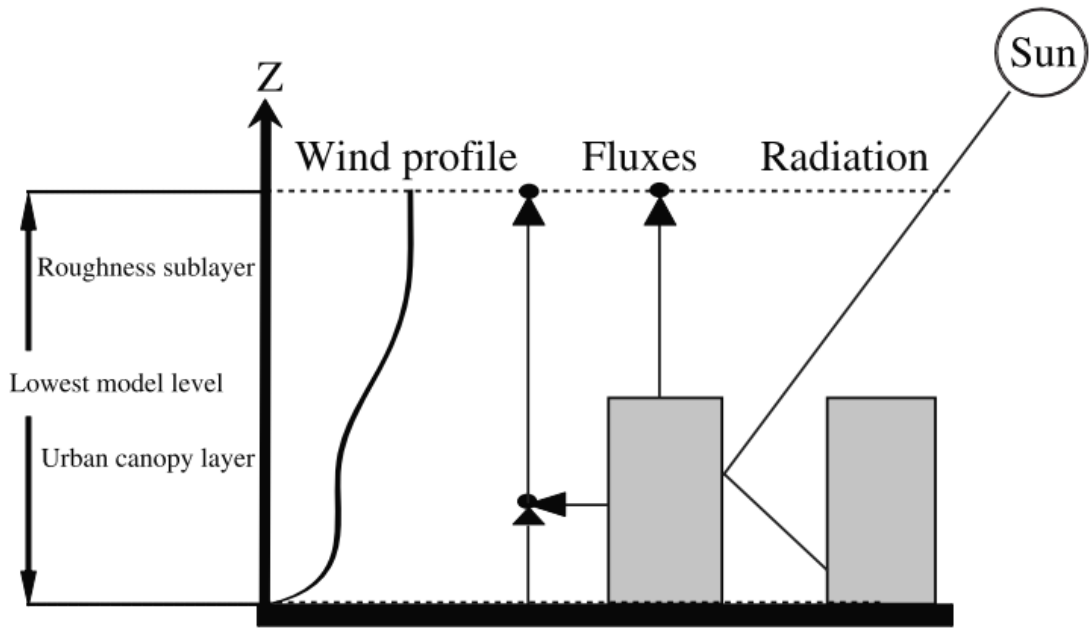
Figure 5.2 Schematic of Single urban canopy model

A single-layer urban canopy model assumes that the infinite length of the street represents the urban geometry but can recognize the three-dimensional urban surface (Kusaka & Kimura 2004). In the street canyon, an additional wind profile description file is specified, taking into account the effects of shadow, reflection and capture on radiation. The predicted variables include surface temperature (calculated from the surface energy balance) and temperature profile (calculated from the heat conduction equation) of roof, wall and road surfaces. The sensible heat flux of each surface was calculated using Monin-Obukhhov similarity theory and Jurges formula. The total sensible heat fluxes of roofs, walls, roads, and city blocks are transmitted to the WRF-NOAH model. The total frictional velocities of aggregated urban and non-urban surfaces are transmitted to the WRF boundary layer scheme. Consideration of anthropogenic heat and its diurnal variation needs to be considered in the aggregate sensible heat flux output of the urban canopy model (Mukul et al., 2007). In total, SLUCM takes into account about 20 parameters. (Hashim et al., 2012; Ahmed et al.,

2015; Morris et al., 2015).

Anthropogenic heat is mainly produced by human production and living and biological metabolism. For example, in industrial production, the heat released by fossil fuels in the combustion of gas stoves and internal combustion engines and other equipment, air temperature regulation equipment and vehicle exhaust heat are the most significant causes of anthropogenic heat. Likewise, a dense residential population directly contributes a large amount of anthropogenic heat. The effect of anthropogenic heat on urban heat balance mainly depends on the geographical location of the city, the size of the construction scale of the city, the level of population density, the level of energy consumption per person, the nature of the city and regional climate conditions, including seasonal and diurnal variations (Li et al, 2015).

At present, the energy inventory method, energy balance method and building energy efficiency modelling method are the main methods to study urban anthropogenic heat emission. The energy inventory method is a practical, reliable, and widely used method, which estimates anthropogenic heat emissions based on energy consumption in statistical yearbooks. In this method, anthropogenic heat is divided into three aspects: industrial anthropogenic heat emission, transportation anthropogenic heat emission and residents anthropogenic heat emission (Wang et al., 2011; Lu et al., 2014).

The calculation formula of annual anthropogenic heat emissions E_i from industrial sources is as

$$E_i = C_i \times \varepsilon_e$$

Where C_i is annual consumption of standard coal in industry and ε_e is Calorific value of standard coal (29306 kJ/kg).

The calculation formula of annual anthropogenic heat emissions E_i from transportation sources is as

$$E_i = C_g \times \varepsilon_g + C_d \times \varepsilon_d + C_{LPG} \times \varepsilon_{LPG}$$

Where the C represents fuel consumption, ε is Calorific value and subscript g, d and LPG are gasoline, diesel, and liquefied petroleum gas, respectively.

The calculation formula of annual anthropogenic heat emissions E_r from residents' sources is as

$$E_r = C_r \times \varepsilon_e$$

Where C_r is annual consumption of standard coal in residents and ε_e is Calorific value of standard coal.

The annual coal consumption can be obtained directly from The Shanghai Municipal Bureau of Statistics, while the transportation fuel consumption needs to be estimated approximately by data. Li estimated the anthropogenic heat in Shanghai in 2015(Li et al., 2015) and proved the data that the average AH applicable to WRF model should be 120Wm^{-2} in downtown Shanghai, based on which the reasonable AH value setting for other years can be calculated.

130 Wm^{-2}, 90 Wm^{-2} and 50 Wm^{-2} are set for year 2017, year 2010 and year 2000, respectively.

For model physical setting, the Yonsei University scheme (Hong et al., 2006) is employed. A combination of YSU scheme with the coupled NOAH/UCM land surface model is deemed to perform well in high resolution urban climate applications (Hong et al., 2006; Lin et al., 2008). Other physical settings including the microphysics scheme of single-moment six-class microphysics scheme (Hong et al., 2006; Dudhia et al., 2008), and a surface-layer scheme based on the Monin-Obukhov similarity theory are used. For radiation, the Dudhia shortwave radiation scheme (Dudhia 1989), and the RRTM longwave scheme (Mlawer et al., 1997) are applied for all domains. While the Kain-Fritsch convective cumulus parameterization scheme (Kain et al., 2004) are

applied only on the D01 and D02. D03 do not need any cumulus parameterization as it is able to resolve updrafts and downdrafts in such a sufficiently refined resolution.
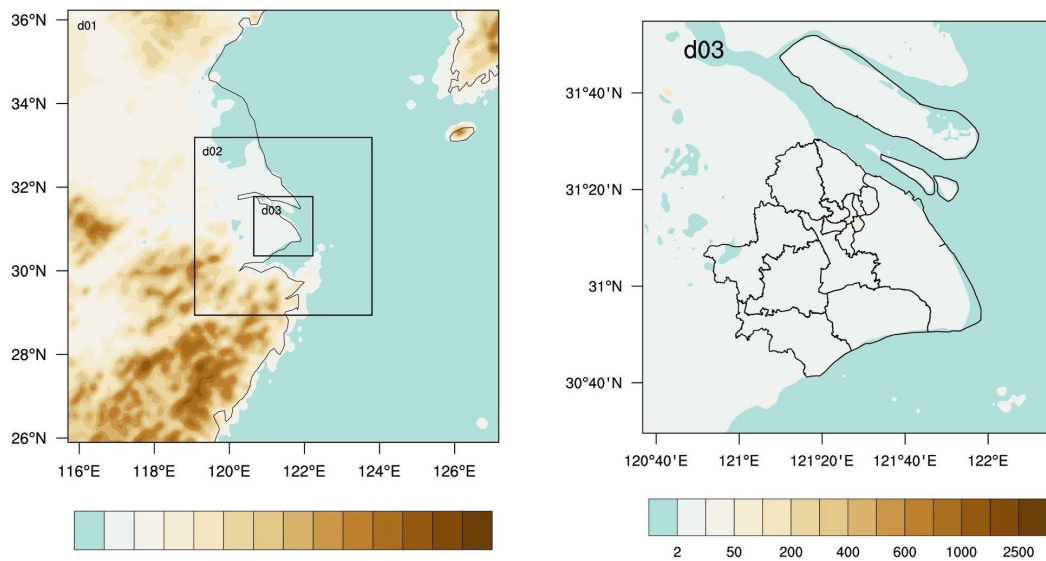
Figure 5.3 Domain setting of the simulation and terrain height of simulation area

A 3 one-way nested simulation is used in this simulation, shown as in Figure 5.3 The horizontal grid resolution is 9km for D01 (out domain), 3km for D02 (middle domain) and 1km for the finest domain as D03 in the centre. There are 128×128 grids for D01, which covers the most area of Southeast China. D02 with 118×118 grids are mainly Yangtze River Delta, while D03 covers only the whole central area as our main study interest. For the vertical setting, there are 34 hydrostatic-pressure levels to resolve vertical layers for all domains, with 15 of the levels are reserved below 850 hPa to further resolve turbulence and frequent changes of atmospheric variables within the lower planet boundary layer (PBL) and top at 100hpa. Further, these lower levels would be helpful illustrating the small-scale feature near Earth's surface (Morris et al., 2016)

To explore the impact of urbanization on local climate in Shanghai, three cases of Shanghai underlying surface data in different years are simulated, namely, the underlying surface data in 2000, 2010 and 2017, which are converted into static data sets that could be directly read and used by WPS according to the classification model

of MODIS-33 category system. Figure 5.4 is a visual representation for the compositions of land use classes for different years.

Except for the static data set, other physical parameters and simulation settings remain constant. Such sensitivity tests are used to investigate the impact of urbanization and urban expansion in Shanghai on local climate since the 21st century.

In addition, a control group was set up in the simulation where all impervious materials in urban area are replaced by vegetation cover such as cropland, which is used as an ideal experiment to explore the spatial distribution of urban heat island effect. This research method can effectively reduce the convection due to ambient heat flow through the surface, and advection due to radiation flux (Li et al., 2013).
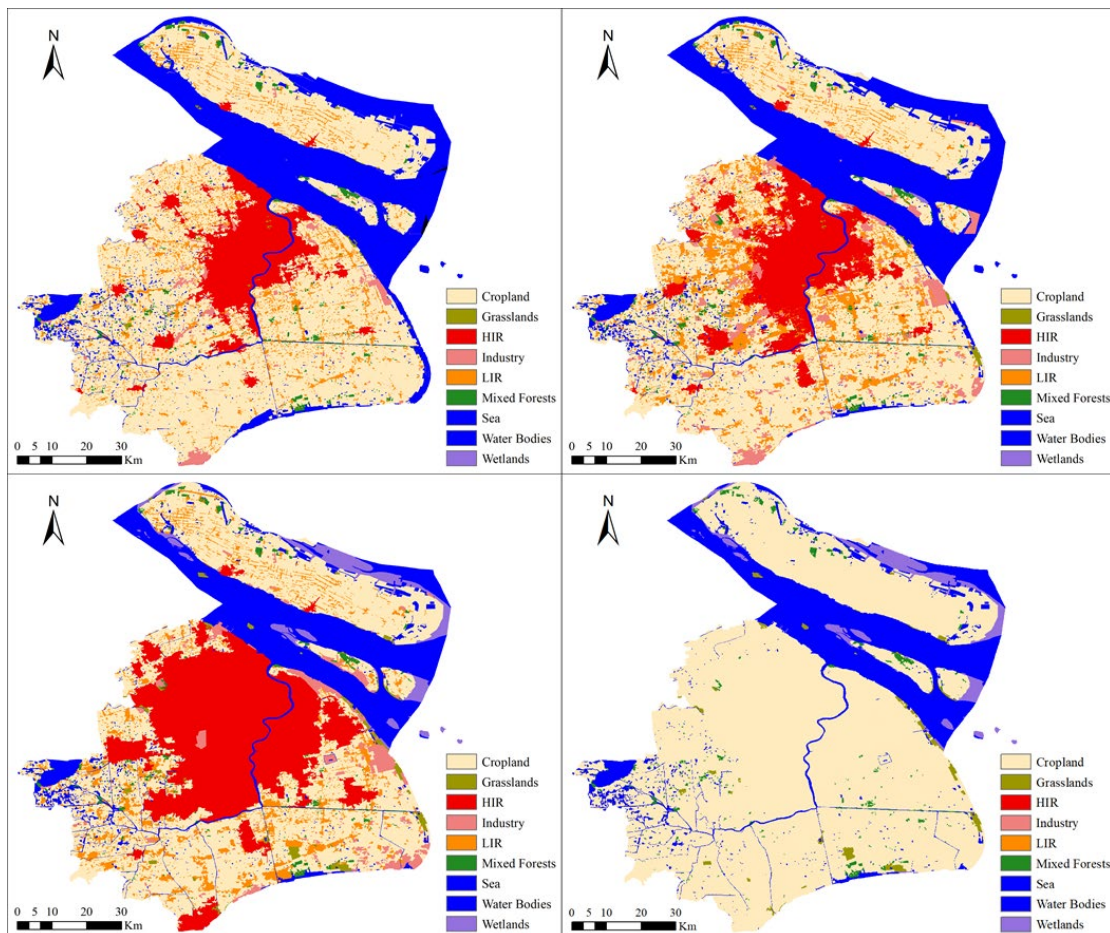
Figure 5.4 Land use and Land cover map for year 2000 (top left), year 2010 (top right), year 2017 (bottom left), Control case – no Urban (bottom right)

The simulation duration is set to 288 hours after the beginning of 0000 UTC on July 21st, 2017, during which an extreme heat event lasted for several days, and a relatively stable weather process was maintained for most of the time of the simulation. The first 24 hours of the simulation were set to spin-up time. The lateral boundary conditions data during the simulation are FNL reanalysis data provided by US National Environmental Forecasting Centre with a resolution of 0.25°×0.25° updated every 6 hours (NCEP, 2000).

5.2.3 Observation data for validation

Observation data used is hourly data from Surface Meteorological Stations in China. In this case, there are 11 national observation stations in Shanghai and the real time data is quality controlled at an overall 99% accuracy standard. The information from observation stations can be found in table 4.1 and Figure 5.5 Model validations and analyses are conducted using this observation data on corresponding results from d03, unless stated otherwise.

Table 5.1 Observation stations information

Station Name	Station ID	Longitude (°)	Latitude (°)	Elevation(m)
Minhang	58361	31.10	121.37	5.5
Baoshan	58362	31.40	121.45	5.5
Jiading	58365	31.37	121.25	4.4
Chongming	58366	31.67	121.50	4.3
Xujiahui	58367	31.20	121.43	4.6
Nanhui	58369	31.05	121.78	5.0
Pudong	58370	31.23	121.53	4.4
Jinshan	58460	30.82	121.27	-
Qingpu	58461	31.13	121.12	4.0
Songjiang	58462	31.03	121.23	4.2
Fengxian	58463	30.88	121.50	4.6

Figure 5.5 Observation station location map

5.3 Model evaluation

The biggest problem of the numerical simulation is inherent deviation caused by unreasonable parameterization of the real physical process. Therefore, statistical verification of simulation results and observation data is necessary. In this study, the following 8 indicators will be calculated to evaluate the coincidence of the model with the observed data, namely, mean value, MBE, MAE, RMSE, R, R^2, HR, and IOA.

MBE is used to measure the tendency of the model to overestimate or underpredict the predicted events. It cannot be used to reflect the typical error of the simulation itself, and therefore cannot be used as an indicator of accuracy (Moriasi et al., 2007). MAE, on the other hand, is more commonly used to indicate the typical size of the prediction

error (Wilks 2006).

RMSE is generally used to measure model accuracy and precision (Willmott et al., 1985) and aggregate the size of prediction errors of various time series into a single measure of predictive power related to model prediction (Murphy, 1988; Lundy et al., 2001). Smaller numbers of MBA, MAE, and RMSE represent simulations that are closer to reality.

Both R and R^2 are values in the range of 0~1. The higher the value of R (close to 1), the stronger the linear relationship between the prediction variable and the observed variable, while the higher R^2 represents the smaller the fluctuation between the prediction variable and the observed variable (Wilks, 2006). R and R^2 are generally used to represent the acceptability of model predictions (Santhi et al., 2001; Liew et al., 2003). However, because these two parameters are too sensitive to the abnormal deviation value of the model, HR and IOA need to be introduced as further indicators (Legates and McCabe 1999).

HR is one of the standards to measure the reliability of prediction. By calculating the frequency of deviation less than the threshold value, it represents the probability of correct 'yes' event obtained from simulation results. IOA is also known as the original Willmott index is used to measure how well model results simulate observed data (Willmott, 1984). IOA is a dimensionless number ranging from 0 to 1. The closer it is to 1, the better the model simulation is (Pereira et al., 2018).

The HR threshold value is set as 1.5°C (Cox et al., 1998) for 2-m temperature, 1.0 m/s (Kulkarni et al., 2008) for 10-m wind speed and 5% (Lawrence, 2005) for relative humidity as the desired accuracy.

5.3.1 Near-surface urban climate parameters

The verification of the model performance is evaluated by comparing the simulation

results of D03 in the 2017 case with data from 11 observation stations. The simulation time started on July 21, 2017. Since the difference between local time and World Standard time is 8 hours, the actual corresponding time would be 8000 local time on July 21, 2017. The first 24 hours of simulation are abandoned as spin-up time, and the subsequent simulation results are averaged within a standard day (24 hours).

Table 5.2 land use types at each station

Station Name	Station ID	Classification in Model
Minhang	58361	Urban(HIR)
Baoshan	58362	Urban(HIR)
Jiading	58365	Urban(HIR)
Chongming	58366	Rural (Cropland)
Xujiahui	58367	Urban(HIR)
Nanhui	58369	Sub urban (LIR)
Pudong	58370	Urban(HIR)
Jinshan	58460	Sub urban (LIR)
Qingpu	58461	Sub urban (LIR)
Songjiang	58462	Urban(HIR)
Fengxian	58463	Rural (Cropland)
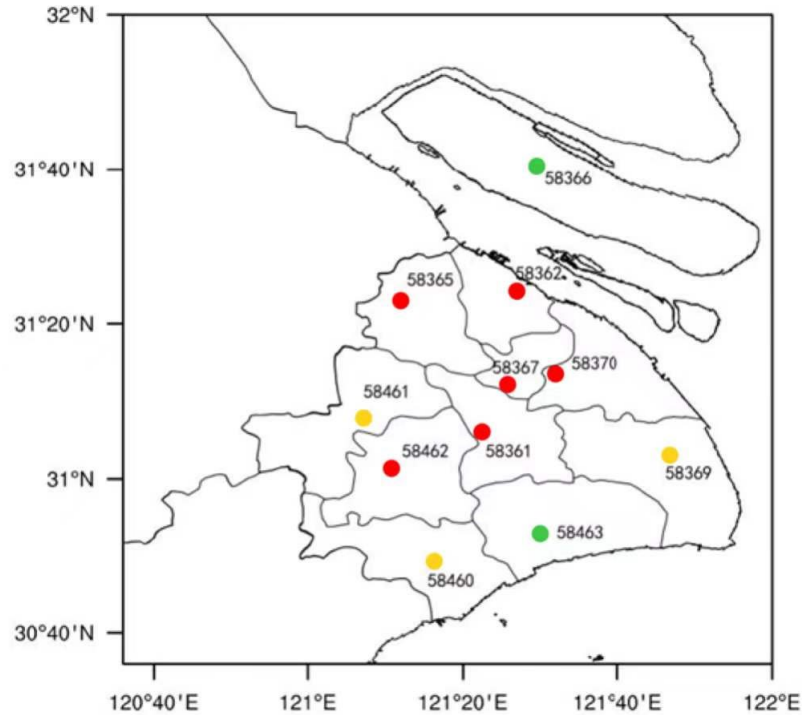
Figure 5.6 Observation station location with land use classification (Red: Urban, Yellow: Sub-urban and Green: Rural)

In order to verify the reliability of spatial distribution of simulation results, the underlying surface of 11 observation stations is classified as follows according to the underlying surface data of simulated cases in 2017 as indicated in table 4.2 and Figure5.6 Minhang, Baoshan, Jiading, Xujiahui, Pudong and Songjiang stations are classified as urban areas due to the land cover information in WRF is high intensity residential area, while Nanhui, Jinshan and Qingpu station are Sub-urban (or low intensity residential area in WRF). The Rural area stations are Chongming and Fengxian station as cropland land cover in WRF.
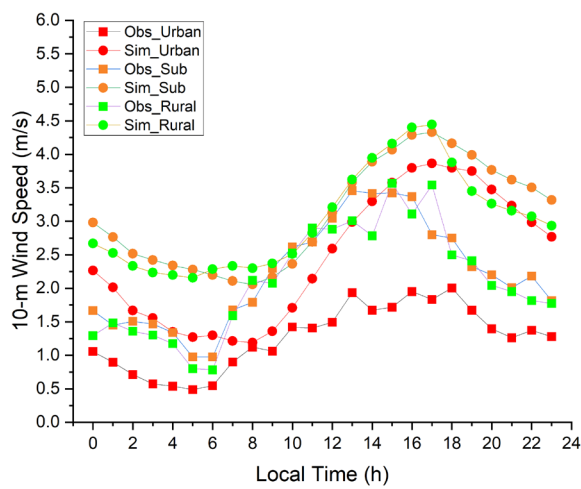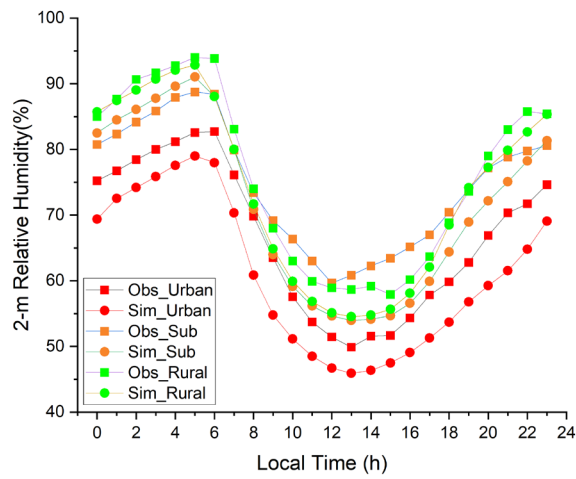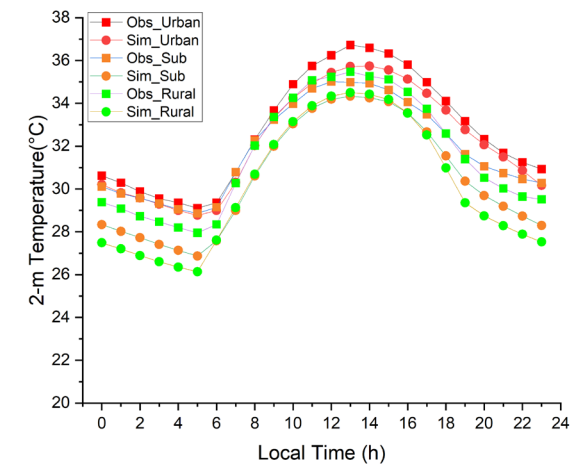
Figure 5.7 Model validation for near-surface urban climate variables: (a) 2-m temperature, (b) 2-m relative humidity, (c) 10-m wind speed

Table 5.3 Model evaluation statistics for near surface variables

Variables	Statistics Indicators	Urban	Sub Urban	Rural
T2m (°C)	MBE	-0.503	-1.343	-1.446
	MAE	0.503	1.343	1.446
	RMSE	0.551	1.432	1.505
	R	0.998	0.997	0.995
	R^2	0.996	0.995	0.99
	IOA	0.988	0.916	0.933
	HR	0.958	0.542	0.5
RH (%)	MBE	-5.683	-3.136	-2.101
	MAE	5.683	4.184	2.21
	RMSE	5.899	4.99	2.648
	R	0.99	0.992	0.994
	R^2	0.981	0.983	0.987
	IOA	0.934	0.951	0.99
	HR	0.5	0.583	0.958
WS10m (ms^{-1})	MBE	1.203	0.888	0.896
	MAE	1.203	0.919	0.903
	RMSE	1.351	1.072	1.004
	R	0.85	0.691	0.828
	R^2	0.723	0.478	0.685
	IOA	0.456	0.585	0.655
	HR	0.417	0.5	0.542

In general, the model can successfully capture the diurnal variation curve of 2-m air

temperature (Figure 5.7 and Table 5.3). The simulation corresponds with the observed 2-m air temperature. Particularly, the simulation result match with the urban area with only 0.551 RMSE. However, the result for sub-urban and rural areas are slightly inferior to urban area, with RMSE of 1.432 and 1.505 respectively. It is worth noting that the simulated temperature is generally observed to be smaller than the observed value in the three different scenarios, and such underestimation is more obvious in the area with lower urban coverage (MBE -0.503, -1.343 and -1.446 for urban, sub-urban and rural, respectively). For the urban area, the underestimation of air temperature may be due to the insufficient estimation of AH or the underestimation of the re-reflected energy flux in UCM model. The underestimation result of rural areas, however, may be since the observation stations are still being influenced by the underlying surface of urban area.

For the simulation of relative humidity, a similar conclusion can be obtained; the simulation has a good grasp of the diurnal profile of relative humidity. However, the overall relative humidity is still underestimated, which is more obvious with the increase of urban coverage (MBE for urban is -5.683, for sub-urban as -3.136 and for rural as -2.101). This may be due to the overestimation of impervious underlying surface coverage in the model, especially in the main urban area, which fails to fully consider the spatial heterogeneity of urban fractions. For sub-urban and rural space, the simulation effect is better, with RMSE being 5.899, 4.99 and 2.648 for 3 different cases. The simulation for wind profile is not so satisfactory as that for the previous 2 near-surface urban climate parameters. The simulation results show that there is a persistent overestimation of wind speed, especially in the afternoon. This may be because of the low complexity of the urban underlying surface considered in the single-layer canopy model, which makes the drag effect of buildings on wind speed unable to be effectively reflected. In addition, observation stations in the main urban area are in relatively

complex urban environments, which is more difficult to be reflected by the current model. Nonetheless, an overall correlation coefficient is obtained with 0.85 for urban, 0.69 for sub-urban and 0.828 for rural areas, which indicates the model still serve as an accurate representation of the simulated case.

In conclusion, the WRF/Noah LSM/UCM model can reflect the daily variation curves of near-surface urban climate parameters, such as temperature, relative humidity and wind speed. Additionally, the simulation results are consistent with observed data in spatial distribution.

LULC Maps of 2000 and 2010 are also imported into WRF in subsequent experiments. A sensitivity analysis is presented aiming to explore the specific impact of urbanization on local climate in Shanghai since the 21st century.

5.4 Results and Discussions

5.4.1 LULC change

One noteworthy feature of so-called urbanization is the land cover change of cropland area from vegetation and permeable soils to urban and semi-urban forms with impervious surfaces. As opposed to interactions of solar radiation, the physical properties change of land use and land cover largely determines the surface energy balance of the region. This is due to the different physical and chemical properties of the constituent materials. It is therefore appropriate to carefully identify rural and urban land with relevant characteristics when investigating urban climate and related phenomena such as surface temperature, moisture availability, relative humidity, and urban heat island, urban dry island, and planetary boundary layer height in the region.
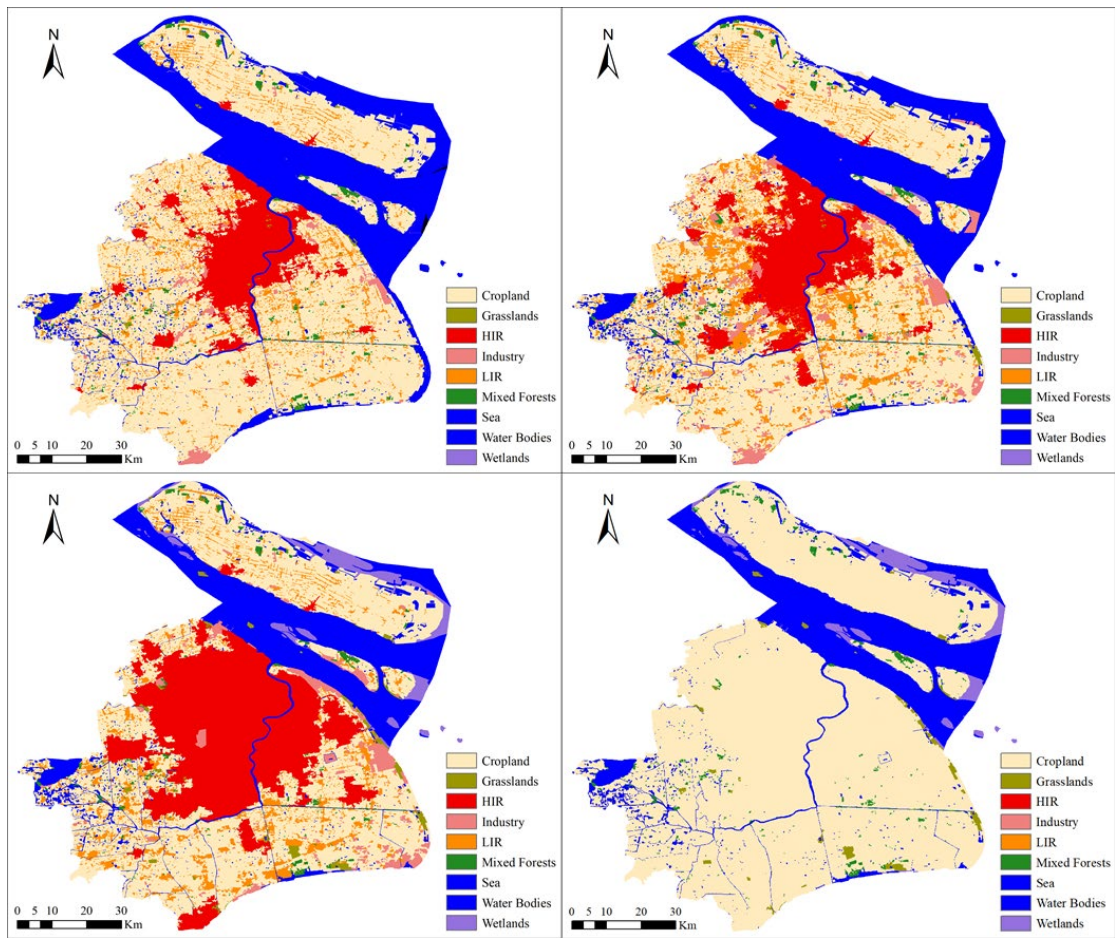
Figure 5.8 Land use and Land cover map for year 2000 (left), year 2010 (middle) and year 2017 (right)

The LULC data shown in Figure 5.8 are different data sets of 2000, 2010 and 2017 obtained from Landsat 8 remote sensing images and processed by ArcGIS (Xu et al., 2018). The data set is provided by Data Centre for Resources and Environmental Sciences, Chinese Academy of Sciences.
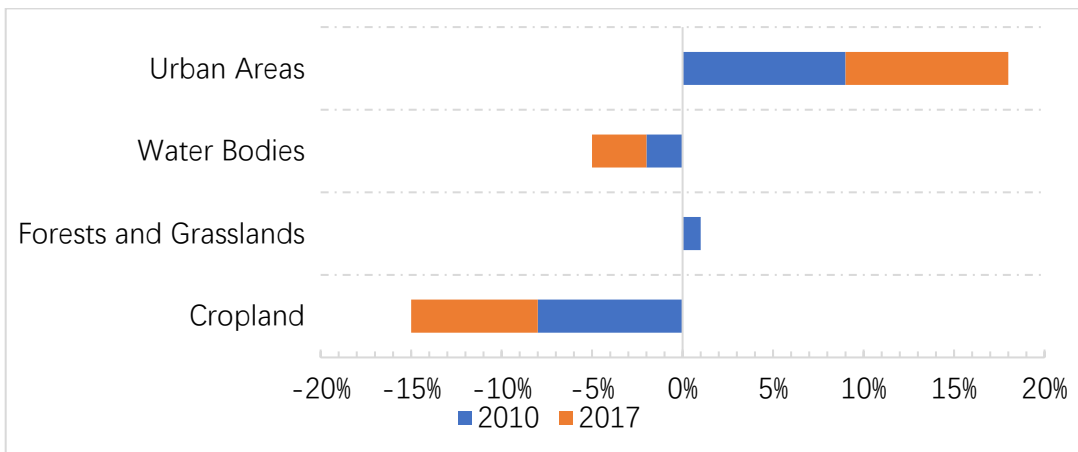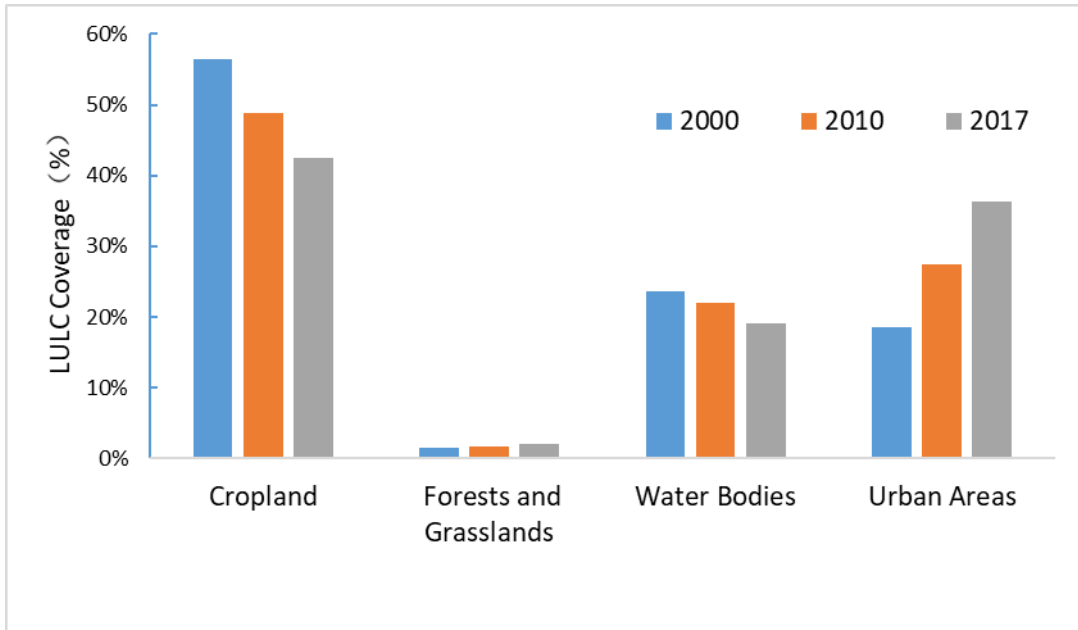
Figure 5.9 (a) coverage of each LULC in 2000, 2010 and 2017 (b) change of each LULC class

Figure 5.9a shows the percentage of area occupied by each specific land use classification. with similar classifications reclassified as cropland, forests and grass land, water bodies, and urban area to simplify the comparison. Figure 5.9b shows the proportion of values of specific changes in 2010 and 2017.

The increase of urban land use mainly comes from human transformation of urban environment, that is, transforming natural green cover into urban engineering surface. From 2000 to 2010 to 2017, urban coverage increased from 18% to 27% and 36%,

respectively. The proportion of farmland decreased from 57% in 2000, 49% in 2010 and finally to 42% in 2017. The water bodies in urban area also decreased year by year, from 24% in 2000 to 19% in 2017. The sharp loss of water bodies and farmland is attributed to the rapid construction of buildings, roads, urban pavements, and pedestrian paths that are ongoing in the area. It should be noted that there was some improvement in vegetation coverage, such as parks within the urban area, from 1% in 2000 to 3% in 2017, but such changes may not be obvious to the results due to the low static resolution of WRF data(1km×1km).

As can be seen from Figure 5.8, compared with 2000, the development direction in 2010 mainly focused on the southward expansion of the city, while a large number of low-density urban areas were built up in the west part of Shanghai, while the east of the Huangpu River did not see much change. However, LULC in 2017 highlights the trend of Shanghai's westward development, with almost all low intensity residential area being replaced by high intensity areas, except for the traditional downtown area. For example, Baoshan, Jiding, Qingpu and Minhang have all been developed into high intensity urban areas. The east bank of the Huangpu River has evolved into the Pudong New Area with higher urban coverage. Low-density urban areas are scattered on the southern side of Shanghai.

Impacting of such changes in land use and land cover over a period on air temperature, UHI distribution, human comfort and energy balance are closely investigated in subsequent sections.

5.4.2 2-m air temperature

In the simulation of many near-ground urban climate variables, air temperature is often the most concerned hotspot. Figure 5.10 and Table 5.4 respectively show the average temperature changes and their spatial distribution in rural, sub-urban and urban

areas under three LULC conditions in 2000, 2010 and 2017. The influence of urbanization on canopy temperature is analysed.

According to observations, the highest average temperature in urban areas was 32.23°C in 2017, followed by 31.62°C in 2010 and 31.17°C in 2000. The average air temperature in the suburbs of Shanghai increased year by year from 30.26°C in 2000 to 30.8°C in 2017, with an increase of about 0.27°C for both periods considered. This is consistent with the observed changes in land use distribution during corresponding periods. The smallest temperature change was observed in rural areas, with only about 0.16°C, rising from 29.82°C in 2000 to 30.15°C in 2017. The small temperature changes observed in surviving area suggest that the impact of urbanization on air temperature for rural areas is much less significant than in urban area.

Table 5.4 Summary of 2-m temperature for each year

	2000	2010	2017	2017-2010	2010-2000
Urban (°C)	31.17	31.62	32.23	0.59	0.45
Sub-urban(°C)	30.26	30.52	30.80	0.28	0.26
Rural(°C)	29.82	29.97	30.15	0.18	0.15

In addition to the change of average temperature, the distribution of 2m temperature also changed with the transition of land use. As shown in Figure 5.10, the first column shows the average temperature distribution at all time points during the simulation, with the spatial distribution for 2017 at the bottom and 2000 at the top.

An obvious difference can be seen is that with the development of urbanization, the area with high simulated temperature is also gradually expanding. In 2000, the high temperature area is concentrated in the traditional downtown urban area, and there is

little change in 2010 compared with 2000. However, in 2017, the area expands more obviously and tends to the west of Shanghai. This may be due to the fact that the urban area expanded in 2010 were mainly low-density urban areas, while the urban areas that expanded in 2017 were mainly high-density urban area. Most of the structural renovation and construction are represented by materials with low surface albedo, high surface thermal conductivity and surface heat capacity. Thus, resulting in a large temperature rising in 2017 case, which is also reflected in Table 4.5, that is, from 2017 to 2010, the temperature rise in urban area was as high as 0.59°C, while in 2010, it was only 0.45°C.

2m Temperature
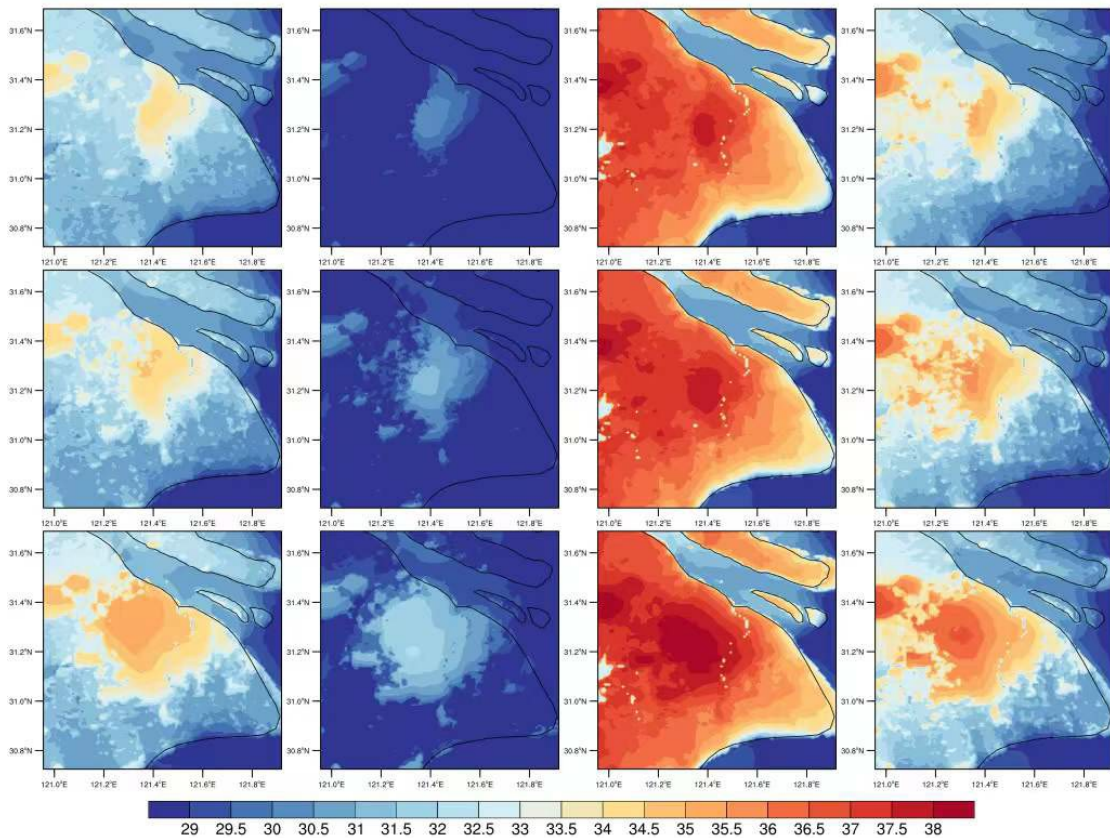
Figure 5.10 First column: Average air temperature distribution of 2000 (up), 2010 (middle), 2017(bottom); Second column: morning time – 0100 -0700 LST averaged air temperature distribution of 2000 (up), 2010 (middle), 2017(bottom); Third column: day time – 1100 -1700 LST averaged air temperature distribution of 2000 (up), 2010 (middle), 2017(bottom); Fourth column: night time – 2000 -2400 LST averaged air temperature distribution of 2000 (up), 2010 (middle), 2017(bottom);

Figure 5.10 also shows the distribution of 2-m temperature at different time periods (morning time – 0100 -0700 LST; day time – 1100 -1700 LST; night time – 2000 -2400 LST). When solar shortwave radiation dominates the energy balance during the daytime, there is no obvious difference in the temperature among different underlying surfaces. However, a large difference in temperature between rural and urban area is seen after

104

sunset. This will be further analysed in a subsequent chapter on the heat island effect.

Overall, the average urban temperature in 2000 was 1.04°C lower than that in 2017, with other conditions remaining the same but only the underlying surface and anthropology heart emission being modified (representing the urbanization took place from 2000 to 2017). This is largely due to urbanization and surface modifications observed in the area. It should be noted that this is only a sensitivity analysis. It is of particular note that with global warming, the average global temperature in 2000 was even lower than that in 2017, making the real temperature difference in Shanghai even larger.

5.4.3 UHI and wind field

Figure 5.10 shows the spatial distribution of 2-m air temperature in different LULC cases, which is able to represent the distribution of urban heat island effect to a moderate extent. In short, the heat island phenomenon becomes increasingly obvious with the development of urbanization. To further explore the heat island effect intensity, a control experiment was designed to replace all the urban underlying surface with cropland, as shown in Figure 5.4d. By comparing the 2000 case, 2010 case and 2017 case with the control case (no_urban case), a more reasonable spatial distribution map of heat island intensity can be obtained. Compared with the traditional 'urban' - 'suburban' approach, this approach has two advantages. On the one hand, it can avoid errors caused by the wrong classification of so called urban and suburban, and on the other hand, it can eliminate the influence of sea-land breezes, impacts of clouds, advection, heatwaves, and topography that may alter the surface temperature or other meteorological parameters (Bohnenstengel et al., 2011; Li et al., 2011; Wang et al., 2014).
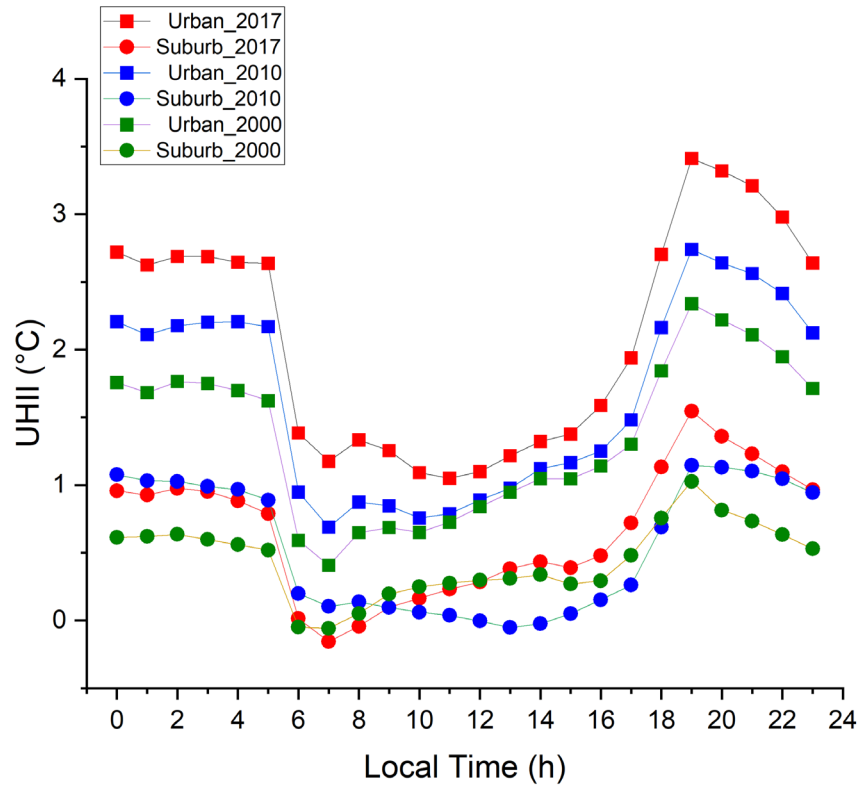
Figure 5.11 Averaged temporal variations of Urban heat island intensity

In the three different cases, the time variation trend of UHII is almost identical (Figure 5.11). Taking 2017 as an example, the results indicate that stronger effect of urban heat island can be found during night time than daytime. The peak value of UHI occurs at time around 1900LST with a maximum magnitude of 3.32°C in 2017 case. In the next few hours, the urban heat island effect has been slowed down to a certain extent and maintained a relatively stable level before sunrise. During daytime, the Earth's surface is heated by direct solar radiation and atmospheric longwave fluxes, which dominates the fluxes over vegetated and urban landcover; this in effect reduces the thermal difference between urban and vegetated surfaces during daytime.

With the urbanization process in Shanghai, the average intensity of the heat island effect has gradually increased, from 1.35°C in 2000 to 2.08°C in 2017. What is of

greater note, is that the maximum value of UHII increased from 2.33°C to 3.41°C, indicating that the extreme value of the UHII is more sensitive to urban coverage.

In 2010, as urbanization process was concentrated on suburban construction, it could be seen that the heat island effect of suburbs at this time had a higher improvement than that of 2000 (1.03°C in 2010 and 0.62°C in 2000), but with the gradual disappearance of rural area in 2017, such UHII changes are no longer evident.

In addition, it should be noted that although the heat island effect in all three cases showed low values during daytime, the minimum heat island effect in 2017 was significantly higher than that in 2000 and 2010, which may be caused by the fact that AH still heated the underlying surface in the daytime, while AH setting in 2017 case is much higher than 2010 and 2000(120, 90 and 50, respectively).

To further explore the spatial distribution of the heat island effect, Figure 5.12 shows the spatial distribution of UHI during night (when the heat island effect is at its strongest). As with the development of urbanization, the coverage area will also gradually improve. In 2000, it mainly concentrated in downtown area, while in 2010, it expanded southward, which is consistent with the trend of land use change.

Furthermore, the heat island centre in 2017 goes more western than that in 2010. This is close to the trend of land use change, but the heat island centre is not in the centre of urban development. This is mainly due to the underlying surface being predominantly composed of artificial materials with high thermal storage ability. The heat gradually releases at night, resulting in a vertical momentum that will push up the planetary boundary layer height. As a result, the air pressure over the urban area is lower than the surrounding area, resulting in heat island winds blowing toward the urban area. Coupled with land and sea winds blowing from the sea at night, the centre of the urban heat island shifts to the northwest can be observed. This simulation result

is also consistent with the conclusion of Hu's study on the heat island effect in Shanghai in 2020 (Hu 2020).
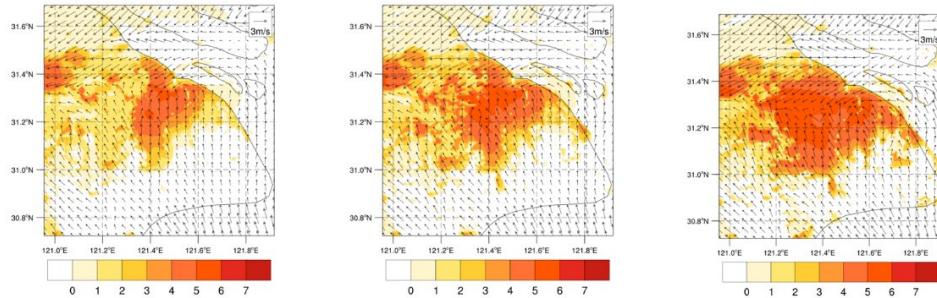
Figure 5.12 Averaged UHII at 1900 LST during simulation for (a) 2000 case, (b) 2010 case and (c) 2017 case.

This is also one of the reasons for the complexity of wind field simulation in Shanghai. Due to the different intensity of heat island effect, it can be observed that the factors leading the wind field over the city in 2000, 2010 and 2017 are different. With the increase of urban underlying surface, the influence of heat island circulation on wind field simulation is gradually obvious. Even in the period of time when the heat island effect is strongest, the wind speed in the urban area has improved, which is one of the reasons why the simulation results are higher than the observation results. However, in general, the simulated average wind speed becomes lower with the advancement of urbanization, especially in urban area (3.419 m/s in 2000, 3.32m/s in 2010, 2.96m/s in 2017, respectively).

5.4.4 Relative humidity and human comfort

The relative humidity value indicates the effectiveness of evapotranspiration in a specific location. Evapotranspiration is regulated by bulk stomatal resistance, which is influenced by root zone soil moisture, photosynthetically active radiation, air

temperature, and leaf surface relative humidity. Grid aggregate parameters for vegetation and soil are produced from fractional coverages of land use categories – urban fraction and soil texture types (Skamarock et al., 2008). Thus, the urban percentage is critical in influencing the fluctuation of the RH over the years studied. This is demonstrated in Table 4.5, where 2000 with the highest vegetation/cropland proportion results in the highest measured relative humidity for the whole area and for all cases Rural area shows higher RH value than urban area.

Table 5.5 Mean Relative humidity of WRF simulated

Year	Urban (%)	Sub-urban (%)	Rural (%)
2000	67.5	73.4	76.2
2010	64.5	69.9	74.9
2017	61	71.4	73.6

Urbanization has a significant impact on the reduction of relative humidity, which is caused by gradually increasing building height, denser buildings, higher surface temperature and stronger heat island effect in urban area. Although the urban underlying surface was the same, the urban relative humidity in 2000 was much higher than the case in 2017. However, the change in rural areas is far less obvious because the change of underlying surface in rural areas is not significant, and the existing decline in relative humidity is more likely due to the decrease of night time relative humidity caused by the step effect of urban heat island effect. It is worth noting that the lowest suburban relative humidity occurred in 2010 due to the vigorous construction of suburban area, which indicates that the change of underlying surface is the biggest factor affecting the simulation of relative humidity.

The relationship between local microclimate status and human thermal sensation

has resulted in the development of several biometeorological indices that have been used to define human thermal comfort levels. The thermohydrometric index, THI (Thom 1958), was chosen to analyse the acquired data since it is recognized to properly reflect variations in air temperature and humidity caused by urban landscapes. The temperature humidity index is easily calculated from the air temperature (°C) and relative humidity (%) using McGregor and Nieuwolt's equation (McGregor et al., 1998):

$$THI = 0.8 \times T_a + \frac{RH \times T_a}{500}$$

where Ta is air temperature simulated in °C and RH is relative humidity in percentage.

However, the temperature and humidity index (THI) is the only human comfort index considered in this study due to its ability to capture land use and land cover-induced changes in air temperature and humidity that frequently affect people's comfort. Monitoring human comfort variances across different land use categories is critical for urban planning and environmental protection.
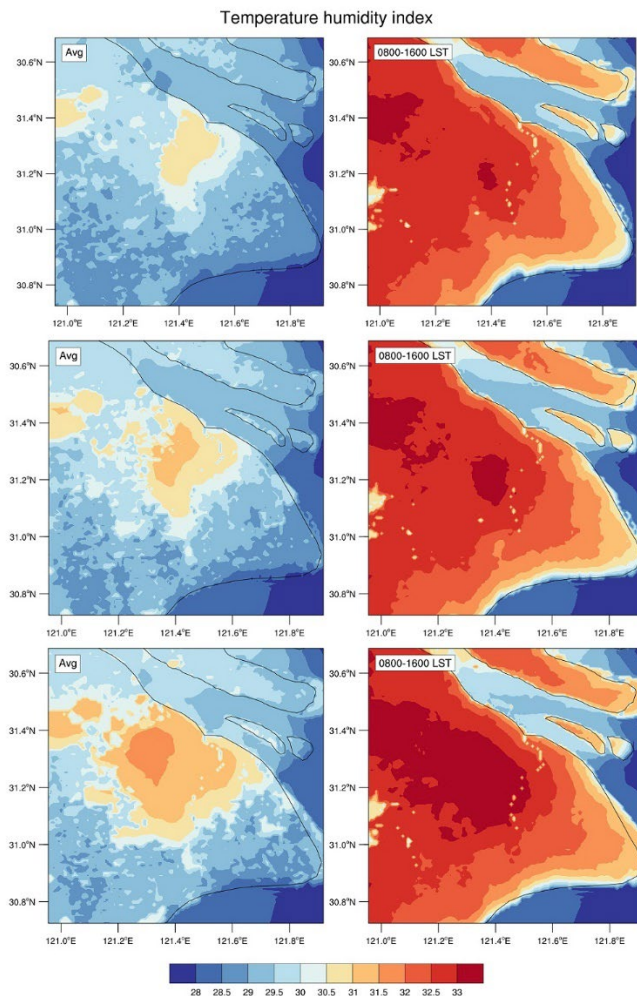
Figure 5.13 Averaged THI in 24 hours for: 2000(up left), 2010(middle left) and 2017(bottom left); 0800-1600LST averaged THI for: 2000(up left), 2010(middle left) and 2017(bottom left)

Figure. 5.13 shows the spatial distribution of THI in three different cases. The average THI shows a synchronous change in the distribution of underlying surface (LULC). With the change of underlying surface from 2000 to 2017, average THI over 30 is only seen in the urban area. Table 4.6 shows the categories of The Thermohydrometric Index (THI) (Kyle 1994). According to the classification in the table, almost all urban areas in 2017 cases are in hot state during the day time. This would increase outdoor work in Shanghai's urban and suburban areas which is unnecessarily dangerous and difficult and would also significantly increase the energy

111

consumption of air conditioners used by urban residents to keep their indoor temperatures down (Biometeorol et al., 1999; Samuel 2017).

Table 5.6 The categories of the thermohydrometric index (THI) (Kyle 1994)

Category	THI Value
Very cold	-9.9 to -1.8
Cold	-1.7 to 12.9
Cool	13 to 14.9
Comfortable	15 to 19.9
Hot	20 to 26.4
Very hot	26.5 to 29.9
Torrid	Over 30

Reducing THI to improve residents' comfort not only requires reducing air temperature, but also increasing relative humidity. As such, increasing urban vegetation coverage is a relatively effective approach, which is also consistent with the widely accepted measures to reduce the heat island effect (Yamamoto 2006; Moris et al., 2016).

The impact of extreme heat on the human health cannot be ignored, including increased hospitalizations and emergency department visits, increased deaths from cardiopulmonary and other diseases, adverse pregnancy and childbirth outcomes, and other vulnerable groups that are more vulnerable to extreme heat. More than 356,000 deaths were linked to heat in 2019, and the number is expected to grow as global temperatures rise (Ebi et al., 2021; Jay et al., 2021). Zhao et al. (2017) calculated the number of hospitalized patients and the frequency of extreme weather in Shanghai and concluded that the average number of hospitalized patients will increase by 1.266 (95% confidence intervals: 1.074 -- 1.493) after the temperature exceeds 33.1°C.
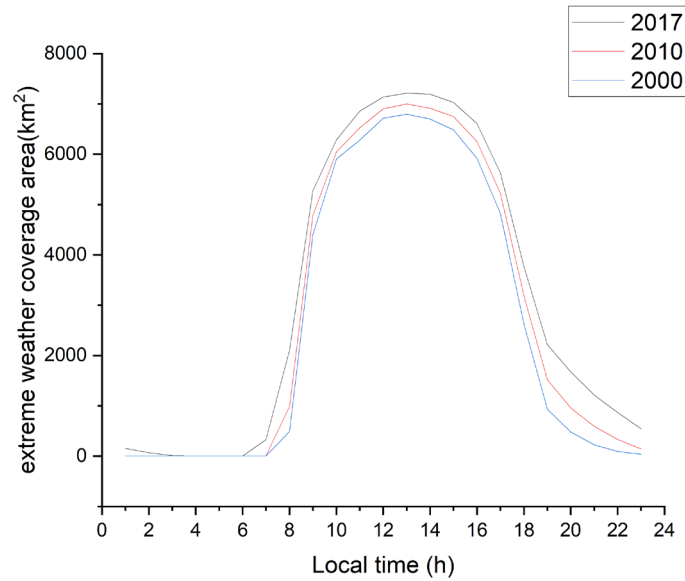
Figure 5.14 Averaged extreme event (air temperature over 33°C) coverage area (km^2) during simulation

Therefore, variation of urban area with simulated temperature over 33°C over time in different cases are shown in Figure 5.14. It can be seen that in the simulation of 2017, not only is the occurrence of extreme high temperature weather is more frequent, so is the occurrence area range of extreme weather events is rapidly expanding with the development of urbanization. In the 2000 case, no extreme weather was observed during seven hours of the night (0100 LST-0700 LST), while in the 2017 case, the gap was only 0400 LST-0600 LST. Meanwhile, in terms of coverage area, extreme weather only covered 6,694 km^2 at 1300LST in 2000, while this value increased to 7,316 km^2 in 2017. It should be noted that due to sensitivity experimental design, such changes in results only come from changes in underlying surface coverage and AH release values. With the worsening of global warming, the future summers will likely be accompanied by higher frequency and greater coverage of extreme heat events.

5.4.5 Energy Balance and PBLH

Table 5.7 Summary of mean sensible heat flux and latent heat flux from model simulations

Year	Urban		Sub-urban		Rural	
	SH (W/m^2)	LH (W/m^2)	SH (W/m^2)	LH (W/m^2)	SH (W/m^2)	LH (W/m^2)
2000	149.7	19.6	88.7	85	57.8	132.2
2010	162.7	20.1	84.7	91.2	56.6	134
2017	179.9	20.4	87	88.5	55.3	134.9

In general, the surface energy balance is not sensible to the land use and land cover change, especially for the latent heat flux. LH remains a relatively stable range for all 3 cases in different year during the simulation. Nonetheless, the sensible heat flux shows dependence on the urbanization process, especially in urban areas, where the average flux increased from 149.7 W/m^2 in 2000 to 162.7W/m^2 in 2010 and 179.9 W/m^2 in 2017. This is mainly due to the expansion of the underlying surface, which makes the urban area absorb more short-wave radiation and store more heat during the day. The temperature difference between the surface and the air brought by this heat is an important source of sensible heat flux.
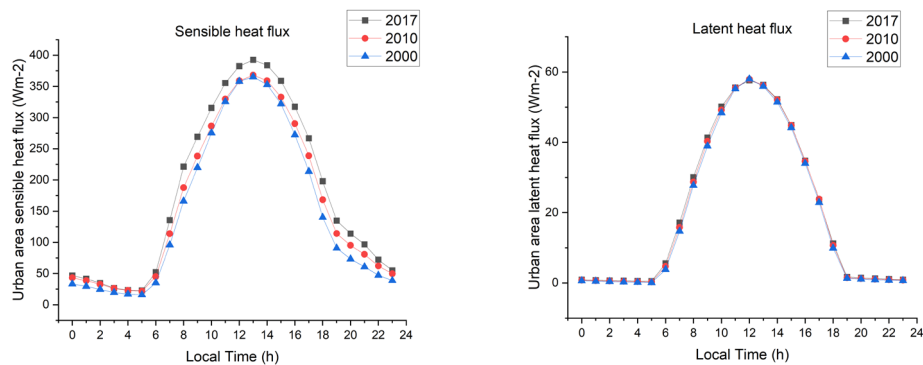
Figure 5.15 Mean diurnal profile of surface energy components: SH (left), LH (right)

This is also reflected in Figure 5.15 as an example diurnal profile of both SH and LH for urban area. The SH gains significantly from the growth in urban surface area, which results in fast fluctuations in surface heat content with sun irradiation during daytime. The maximum sensible heat flux level is recorded between 1200 and 1300LST at 392 W/m^2, 368 W/m^2, and 365 W/m^2 for 2017,2010 and 2000, respectively, followed by a decline in all magnitudes. This is understandable since sensible heat is generated solely by shortwave solar radiation and atmospheric longwave fluxes, and the temperature differential between the ground and atmosphere steadily decreases throughout the night. This also explains that after sunset, the SH values of the 2017 and 2010 cases and the 2000 cases began to differ significantly. Although urbanization is increasing, LH is mainly affected by parameters related to vegetation cover, which has changed little for urban areas in these 3 cases. Therefore, the simulation does not observe drastic changes in LH, or in urban areas.
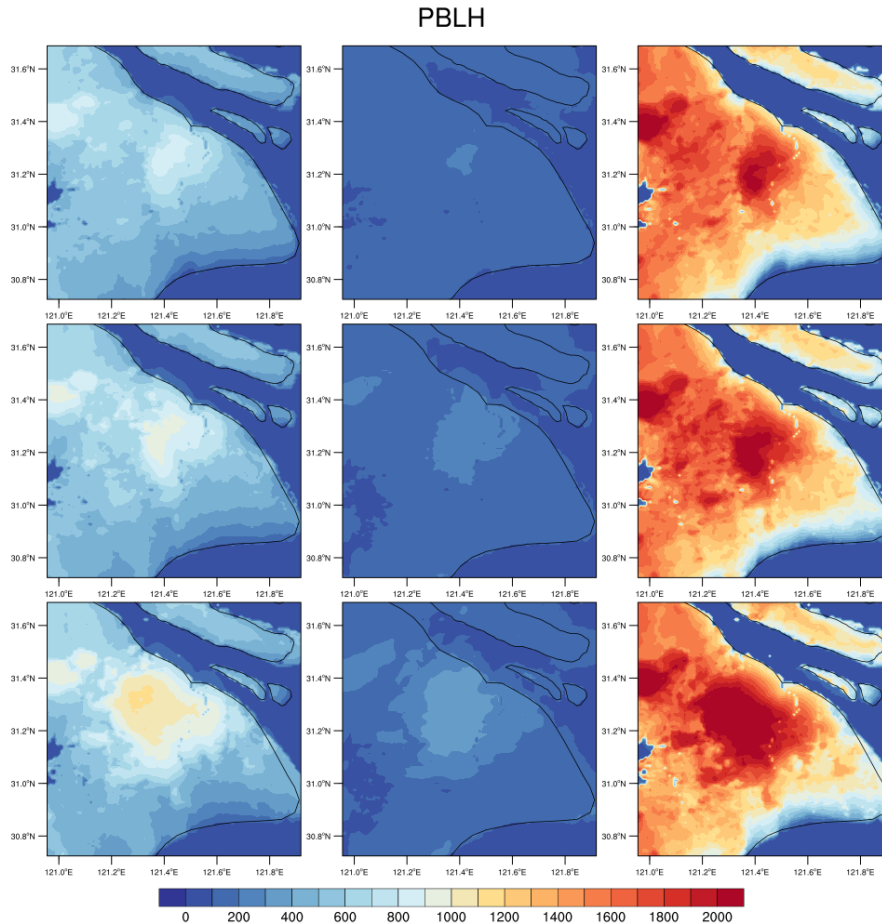
Figure 5.16 First column: Average PBLH distribution of 2000 (up), 2010 (middle), 2017(bottom); Second column: 2000 - 0700 LST averaged PBLH distribution of 2000 (up), 2010 (middle), 2017(bottom); Third column: 0800 - 1900 LST averaged PBLH distribution of 2000 (up), 2010 (middle), 2017(bottom)

The variation trend of PBLH is close to that of 2-M temperature, especially on the diurnal variation curve. During the day, the earth's surface receives short-wave solar radiation and long-wave atmospheric flux. These fluxes heat the surface and increase the surface temperature, resulting in vertical and horizontal transport of heat flux (SH). The time growth of PBLH is influenced by the thermodynamics of solar radiation, atmospheric long-wave flux, and the interaction of sensible and latent heat flux. Therefore, the change in the maximum value was not significant, only rising from 1530m in 2000 to 1619m in 2017.

However, the change of PBLH spatial distribution obviously depends on the expansion of urban areas, that is, the development of urbanization. This is more obvious from the spatial distribution figure of 0800-1900 LST (right column of Figure 5.16). With the expansion of urban area, high PBLH gradually spreads to the west side of Huangpu River. This lowers the pressure in the overlying area below, which is consistent with the wind field explained above.

5.5 Conclusion

A network of observed data from 11 local observation station is used to evaluate our simulation model. The results are corroborated by the observed data, especially for 2-m air temperature. RMSE, MBE, and R2 of 1.16ºC, -1.10°C, and 0.99; 4.51%, -3.64%, and 0.98; 1.14 m/s, 0.99 m/s, and 0.63, are observed for 2-m temperature, relative humidity, and wind speed, respectively.

In this study, the thermal urban climate of Shanghai was successfully identified. The model results show that the distribution of 2m temperature is extremely sensitive to the changes of underlying surface caused by urbanization. By comparing the no_urban method, the heat island effect is investigated and gradually increases of UHII is seen with urbanization process, from 1.35°C in 2000 to 2.08°C in 2017. The frequency and intensity of extreme weather events also increased, with such cases covering 11.2% larger acreage in 2017 than in 2000 and lasting two hours longer after sunset. An increase in THI is found to be also a greater threat to the health of the citizens.

In the sensitivity experiment, the energy balance, especially the latent heat flux did not change much. Nonetheless, the change of urban underlying surface still has an impact on the maximum sensible heat flux. In addition to the influence of land - sea wind and lake wind, the simulation of wind speed also shows the influence of heat island wind on the wind field in the urban area, which is clearly reflected in the case of

117

2017.

In order to further improve the performance of the model, a more detailed LULC map is needed, especially in downtown, urban areas. The local climate zone model can be considered as a direction, but due to the introduction of too many variables, it may be necessary to run further tests in order to verify with reality and obtain more accurate simulation results. Most significantly, the simulation reveals the severe heat island effect and adverse impact on residents' health brought by urbanization. It is therefore critical to consider how to mitigate the heat island effect in the development of Shanghai.

6 Projection of urban climate in the 2030s of Shanghai under different PCR scenarios and development pathways

6.1 Introduction

Today, more than half of the human population lives in urban areas, and this proportion is expected to increase to 66% by 2050; an additional 2.5 billion people are predicted to relocate to cities (United Nations, 2014). The impact of urbanization is mostly on local and regional climate. Nonetheless the process of urbanization has a significant impact on the global-scale climate change. The relationship between urbanization and global-scale climate change is intricate. Cities, regardless of their trivial spatial extend, exert an influence on global-scale climate change (Masson et al., 2020). Identifying the individual and combined effect of climate change and urbanization would provide opportunities for effective planning of urban adaptation strategies to curb the future impact of climate change and urbanization on urban areas.

Shanghai has been one of the largest metropolises in China ever since 1843. Due to its unique geographical and climatic advantages, the city has been endowed with unlimited development potential and opportunities, gradually replacing Guangzhou as the centre of foreign trade. Since 1990, a large amount of arable land was occupied by building land, which has resulted in the total area of construction land in Shanghai being tripled compared to 30 years ago. Now, the total construction land of this city is as high as 46% of the land area, far more than Tokyo, Paris and other international metropolises.

Numerical studies on the impact of future urbanization have been conducted. Georgescu et al. (2014) attempted to simulate the sensitivity of temperature to the future expansion of cities in the United States. Doan et al. (2016) evaluated the impact of future urbanization in the case of HCM City, Vietnam. However, there are few studies

on the future urban climate in Shanghai. This study will propose two different RCP development paths in 2030, to simulate and analyse the climate of Shanghai in the summer of 2030 by making different RCP scenarios and using dynamic downscaling method under the premise of considering the development of urbanization.

6.2 Methodology

6.2.1 Study region

Shanghai is in the eastern part of China, at the lower reaches of the Yangtze River, between 120.87° E -122.2° E and 30.67° N-31.88° N, with a total area of 6,340 km^2. As a part of the Yangtze River delta impact plain, Shanghai has a dense network of rivers and abundant water systems, and the terrain is vast and low, with an average altitude of only 2.19 meters above sea level, the highest point of which is 103.7 meters above sea level on Da Jinshan Island in Jinshan District. Shanghai's climate is mild and humid, with distinct seasons, short spring and autumn but long winter and summer. Shanghai has plenty of sunshine and rainfall, with south easterly winds prevailing in spring and summer, and northerly winds in autumn and winter, making it a very typical subtropical monsoon climate.
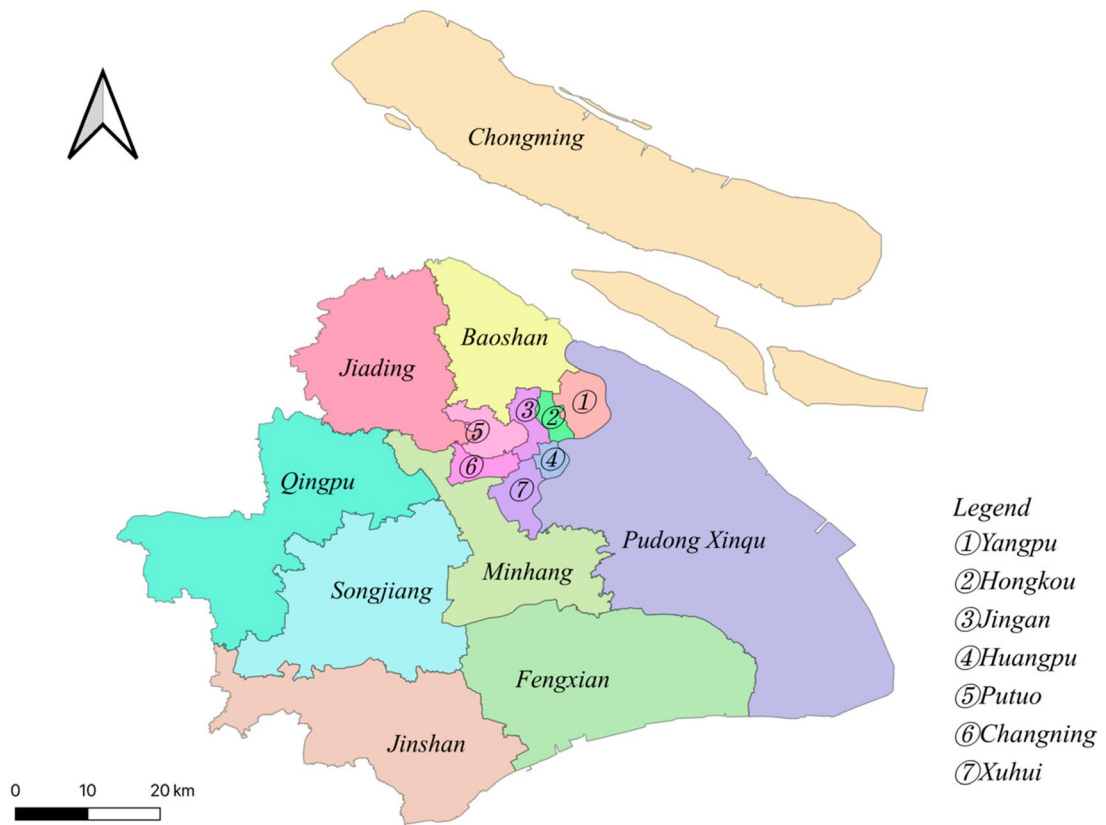
Figure 6.1 administrative divisions of Shanghai

The administrative divisions of Shanghai are shown in Figure 6.1, among which 9 core urban areas are generally considered as the main urban areas, such as Huangpu, Luwan, Xuhui, Changning, Jing 'an, Putuo, Zhabei, Hongkou and Yangpu. The other nine counties far from the city are Baoshan, Minhang, Jiading, Jinshan, Songjiang, Qingpu, Fengxian, Pudong New Area and Chongming county.

Economic growth and industrialization stimulated rapid urbanization and population growth in Asia (Jago-on et al., 2009). From 1949 to 2020, the total population and population density of Shanghai changed significantly with the rapid industrialization and urbanization. The population increased from 5.03 million in 1949 to 24.28 million in 2020, (Shanghai Bureau of Statistics, 2020). And with the industrialization and urbanization of Shanghai, land resources are under increasingly severe spatial and environmental pressure. Due to rapid economic development,

Shanghai has one of the highest rates of LULC change in the last 30 years, which is mainly manifested by urban expansion and decrease of cultivated land. From 1949 to 2020, the largest area of cultivated land was 417,100 hectares in 1990 and only 117,400 hectares in 2020. From 1990 to 2000, cultivated land decreased significantly at a rate of 158,300 ha/ decade, and in the last 10 years, it has rapidly decreased at a rate of 83,800 ha / decade.

With the development of urbanization, Shanghai Urban Master Plan (2017-2035) was announced in 2017 (Shanghai government, 2017), which presents a clear plan for the path of urban development and provides the basis for the subsequent research in this study. This study chooses Shanghai as the main research area and compares the measured land use data of Shanghai in 2015 and forecast in 2030 to explore the impact of urbanization under different the future scenarios of Shanghai

6.2.2 Land use and land cover dataset in 2030

The land use and land cover data using in this study is from the Mega-cities Project led by University of Tsukuba (Murayama et al, 2015). The data is obtained from satellite imageries of different resolutions, for instance, MODIS, Landsat and QuickBird. Landsat images at 30m resolution are mainly used in most cases. The images from satellite sensors are then processed by certain re-classification methods such as Pixel-based classification and object-based classification (Hay and Castilla 2008; Blaschke et al., 2014), Random Forests classification (Breiman 2001) and Support Vector Machine classification (Brian et al., 2011). The final product is re-classified into eight LULC classes: urban dense, urban sparse, forest, cropland, grassland, bareland, water and other land (Murayama et al, 2015).
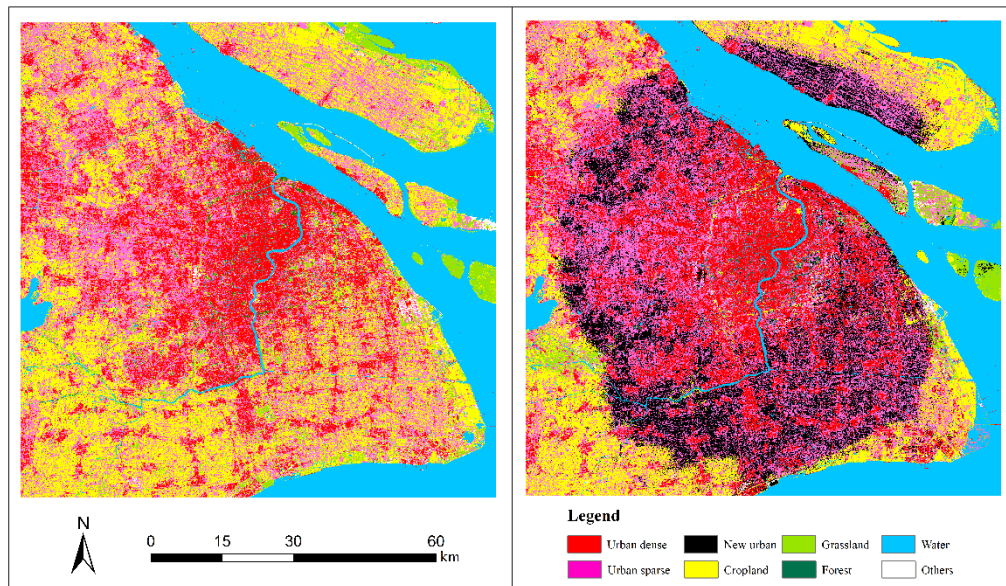
Figure 6.2 Land use and Land cover map of (a) current case (left panel), (b)2030 projected case (right panel)

Figure 6.2a shows the LULC map of Shanghai area in 2015 while Figure 6.2b shows the projected LULC map of shanghai in 2030 based on the known development path of Shanghai in previous observation study. Furthermore, the urban area in 2030 LULC case are considered as 3 different types: urban dense, urban sparse and new built-up urban, the urban dense and urban spare are same with 2015 and new built-up urban is apparently the additional urban area in 2030 compared with 2015 case.

It is fully acknowledged that such classification cannot accurately represent the land use of Shanghai in 2030. For example, some old urban areas may be renovated, or residential areas may be transformed into parks. Such improvement of city appearance cannot be predicted, so the underlying surface of the prediction of 2030 in this study can only be approximated in this way.

Through the comparison of LULC map, it can be found that the future land use change in Shanghai is mainly concentrated in the direction of southeast, accompanied

by urban area expansion and further decrease of cultivated land area. At the same time, it can be expected that the parallel renovation of the new and old urban areas will bring about further changes in the underlying surfaces, such as an increase in the average building height and an increase in the intensity of anthropogenic heat release. This will be reflected in subsequent simulation Settings

6.2.3 Representative Concentration Pathways scenarios

The Representative Concentration Pathways describe the different Pathways of greenhouse gas emissions, air pollutant emissions, land use and atmospheric concentrations evolve in the 21st century. It was developed by Integrated Assessment Models as input to extensive climate model simulations to predict their consequences on the climate system. These climate prediction simulations are in turn used for impact and adaptation assessments. RCPs are a good representation of the broader range of greenhouse gas emissions in the literature, which includes a strict mitigation scenario RCP2.6, two intermediate scenarios RCP4.5 and RCP6.0, and a very high GHG emission scenario RCP8.5 (IPCC, 2021). Different RCP development paths will have different impacts on future global climate, as shown in Figure 6.3. It is generally thought that the worst-case scenario represented by RCP8.5 would be if governments did nothing to limit their emissions (IPCC, 2014). As the world attach more importance to environmental issues, a more reasonable development path should be RCP4.5 or RCP6, depending on the implementation of energy conservation and emission reduction of each country in the future.

(a) Global average surface temperature change (relative to 1986–2005)

(°C)

12

9

6 — 12

3 — 39

0 — 42 · 32 · 12

1900 1950 2000 2050 2100 2150 2200 2250 2300
Year

(b) Global average surface temperature change (relative to 1986–2005)

Mean over 2081–2100

(°C)

6
4 — 39
2
0 — 32
−2

2000 2050 2100
Year

RCP2.6 RCP4.5 RCP6.0 RCP8.5

(c) Northern Hemisphere September sea ice extent

Mean over 2081–2100

(10^6 km^2)

10
8
6 — 3
4 — 5
2
0

2000 2050 2100
Year

RCP2.6 RCP4.5 RCP6.0 RCP8.5

(d) Global mean sea level rise (relative to 1986–2005)

Mean over 2081–2100

(m)

1
0.8
0.6 — 21
0.4
0.2 — 21
0

2000 2050 2100
Year

RCP2.6 RCP4.5 RCP6.0 RCP8.5

(e) Global surface ocean pH

Mean over 2081–2100

(pH)

8.2
8 — 9
7.8 — 10
7.6

2000 2050 2100
Year

RCP2.6 RCP4.5 RCP6.0 RCP8.5

Figure 6.3 Time series of global annual change in different factors for 4 RCP scenarios (IPCC, 2014)

Although different RCP models provide approximate climate change pathways, and the Global Circulation Model simulates future environmental changes based on pre-set pathways. However, in the specific GCM simulation results, different GCM outputs still have significant differences, which will introduce a certain degree of systematic error. To eliminate such error, hence, a bias correction method is needed (Holland et al.,2010; Xu and Yang 2012; Done et al.,2013).

The specific operation method is to divide the prediction results of GCM into two parts:

$$GCM = \overline{GCM} + GCM' \ldots\ldots\ldots\ldots\ldots\ldots\ldots\ldots\ldots\ldots\ldots\ldots \ (1)$$

Where the GCM is decomposed into a seasonally averaged climatological

125

component $\overline{GCM}$ and a perturbation term GCM'.

And same process is done to the observation data as followed:

$$OBS = \overline{OBS} + OBS' \ldots\ldots\ldots\ldots\ldots\ldots\ldots\ldots\ldots\ldots\ldots \quad (2)$$

Where OBS is reanalysis data from observation and $\overline{OBS}$ is mean climatological component.

The bias corrected climate data is eventually calculated by replacing the GCM climatological mean from Eq. 1 with the OBS mean from Eq. 2:

$$GCM^* = \overline{OBS} + GCM' \ldots\ldots\ldots\ldots\ldots\ldots\ldots\ldots\ldots\ldots \quad (3)$$

These bias-corrected climate data thus combine a seasonally varying climate with the six-hourly weather from the GCM. This approach also retains the GCM longer-period climate variability and climate change (Bruyère et al., 2014; Bruyère et al., 2015).

Following this method, the European Centre for Medium-Range Weather Forecasts Interim Reanalysis (ERA-Interim; Simmons et al., 2006 and Dee et al., 2011) fields for 1981-2005 are used as $\overline{OBS}$ and NCAR's Community Earth System Model (CESM; Hurrell et al., 2013) output results are used as GCM' to generate a six-hourly based, with 26 pressure levels and of horizontal resolution of approximately 1° dataset in this study.

In this study, two time periods are selected, one in July 2017 and the other in July 2030. The time period of July 2017 is used to verify the reliability of the model and data set, while the time period of July 2030 is used to reflect the thermal environment of Shanghai in 2030s.

In order to reflect the difference in future global warming predicted by RCP path selection, two different development paths: RCP4.5 and RCP8.5 are used to drive WRF simulation in 2030, and comparative analysis are carried out in later subchapters.

In general, the driving data can be divided into the following three types: July 2017,

July 2030 (RCP4.5) and July 2030 (RCP8.5). It should be noted that for the dataset of July 2017 are also synthesized by observation data and GCM simulation results from 1981 to 2005. Therefore, this dataset also belongs to the "predicted result" (from late 20 century), thus the data in July 2017 under the RCP8.5 path is selected in this study as the driving data to verify the model reliability.

6.2.4 Numerical settings and model initialisation

A 3 one-way nested simulation is used in this simulation, shown as in Figure 6.4 The horizontal grid resolution is 9km for D01, 3km for D02 and 1km for the finest domain as D03. There are 120×120 grids for D01, which covers the most area of Southeast China. D02 with 160×160 grids are dominant by Yangtze River Delta, while D03 covers only the whole central area as our main study interest. For the vertical setting, there are 34 hydrostatic-pressure levels to resolve vertical layers for all domains, with 15 of the levels are reserved below 850 hPa to further resolve turbulence and frequent changes of atmospheric variables within the lower planet boundary layer (PBL) and top at 100hpa. Further, these lower levels would be helpful illustrating the small-scale feature near Earth's surface (Morris et al., 2016)
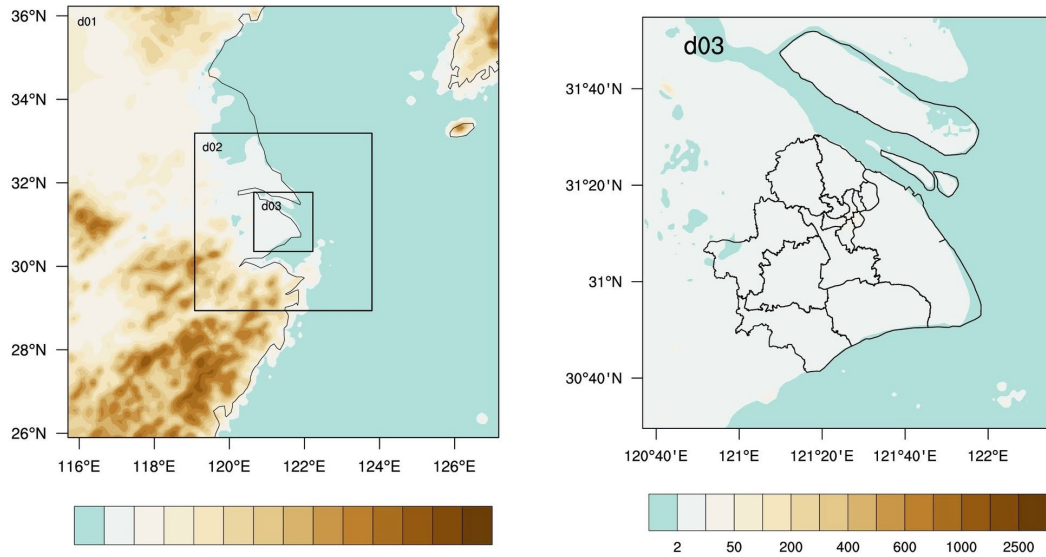
Figure 6.4 Domain setting of the simulation and terrain height of simulation area

Table 6.1 Main Physical parameterization setting

	D01	D02	D03
Microphysics Scheme	single-moment six-class (WSM-6) microphysics scheme	single-moment six-class (WSM-6) microphysics scheme	single-moment six-class (WSM-6) microphysics scheme
Longwave Radiation Scheme	Long-wave Rapid Radiative Transfer Model (RRTM)	Long-wave Rapid Radiative Transfer Model (RRTM)	Long-wave Rapid Radiative Transfer Model (RRTM)
Shortwave Radiation scheme	Dudhia cloud radiation scheme	Dudhia cloud radiation scheme	Dudhia cloud radiation scheme
Surface-layer Scheme	Monin-Obukhov similarity theory	Monin-Obukhov similarity theory	Monin-Obukhov similarity theory
Planetary Boundary scheme	Yonsei University (YSU) scheme	Yonsei University (YSU) scheme	Yonsei University (YSU) scheme
Convective Cumulus Parameterization Scheme	Kain-Fritsch convective cumulus parameterisation	N/A	N/A
Urban Canopy Model	N/A	N/A	SLUCM

Physical parameterizations used are listed in table 4.2, including the microphysics scheme of single-moment six-class microphysics scheme (Hong and Lim 2006; Dudhia et al., 2008), and a surface-layer scheme based on the Monin-Obukhov similarity theory. For radiation, the Dudhia shortwave radiation scheme (Dudhia 1989), and the RRTM longwave scheme (Mlawer et al., 1997) was used. On the D01, the Kain-Fritsch convective cumulus parameterization scheme (Kain, 2001) was applied. D02 and D03 does not need any cumulus parameterization as it is able to resolve updrafts and downdrafts in such a sufficiently refined resolution.

The UCM as single layer urban canopy model was used to consider the effects of urban geometry on surface energy balance and wind shear for urban regions (Kusaka et al., 2001; Kusakaand Kimura, 2001).This model includes shadows from buildings，canyon orientation，diurnal variation of azimuth angle, reflection of short and long wave radiation, wind profiler in the canopy layer, anthropogenic heating associated with energy consumption by human activities and multi-layer heat transfer equation for roof, wall, and road surfaces (Chen et al., 2011).

Anthropogenic heat is mainly produced by human production and living and biological metabolism. For example, in industrial production, the heat released by fossil fuels in the combustion of gas stoves and internal combustion engines and other equipment, air temperature regulation equipment and vehicle exhaust heat are the most significant causes of anthropogenic heat. Likewise, a dense residential population directly contributes a large amount of anthropogenic heat. The effect of anthropogenic heat on urban heat balance mainly depends on the geographical location of the city, the size of the construction scale of the city, the level of population density and energy consumption per person (Li et al., 2015).

In this study, anthropogenic heat is estimated by three aspects: industrial

anthropogenic heat emission, transportation anthropogenic heat emission and residents anthropogenic heat emission based on the method of estimating total coal consumption number from official statistic yearbook (Wang et al., 2011; Lu et al., 2014). The AH max value for urban dense area in 2017 is 120 Wm^{-2} and 180 Wm^{-2} for 2030 case. Considering that anthropogenic heat release has a relatively obvious diurnal variation pattern, and industrial emissions occupy the main source of AH, the change curve of AH built into WRF is changed to figure 6.5, which is closer to the overall anthropogenic heat release pattern in Shanghai (Li et al., 2015).
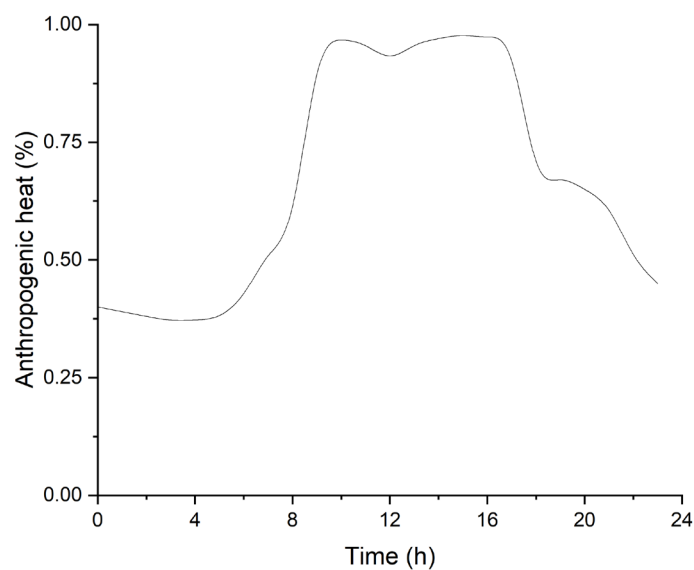
Figure 6.5 The diurnal profile of AH intensity used in the UCM

The total duration of the simulation is 10 days, starting at 1200 UTC on July 20 and ending at 1200 UTC on July 30 (both 2017 and 2030), where the simulation results of the first 20 hours are discarded as spin-up time. If not noted, the data below will average the results of the simulations over a period of 24 hours to obtain the average results of

the simulations for analysis.

In this study, a total of 4 different experimental combinations were designed, as shown in Table 6.2

Table 6.2 Four cases settings in this study

	LULC map	Lateral Boundary data
Case0	Current	2017 RCP 8.5 hindcast
Case1	Current	2030 RCP 8.5 prediction
Case2	2030 prediction scenario	2030 RCP 4.5 prediction
Case3	2030 prediction scenario	2030 RCP 8.5 prediction

Case0 is mainly used to verify the consistency of hindcast data and real observation data, and to represent the reliability of the WRF/Noah/UCM model and input data.

The difference between Case3 and Case1 can be used to represent the impact of urbanization development on climate change in Shanghai in the future while the difference between Case3 and Case2 can be used to characterize the future climate change of Shanghai under different global warming models. The transaction from Case0 to Case2 and Case3 represent the final urban climate change under different development scenarios.

6.3 Model Validation

To verify the accuracy of the 2017 hindcast dataset as WRF lateral boundary data, observations from 11 observation sites of Shanghai in July 2017 were compared with the simulation results. The 11 observation stations are located as figure 6.6 shows.
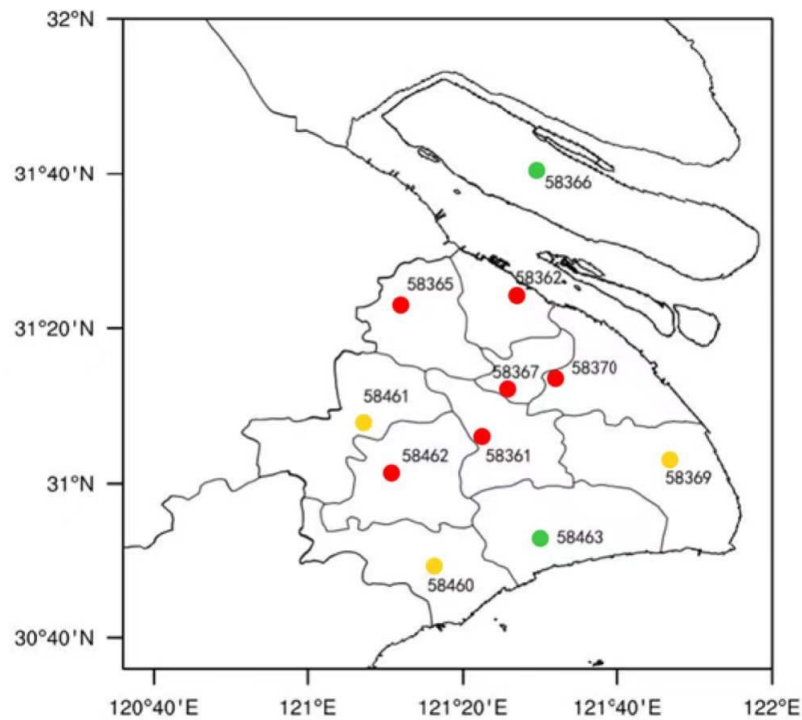
Figure 6.6 Observation station location with land use classification (Red: Urban, Yellow: Sub-urban and Green: Rural)

Due to the fixed location of observation stations, the verification results obtained from a single station are relatively accidental. Therefore, the 11 stations are classified into three categories according to the underlying surface corresponding to the simulation, namely, urban area, suburb and rural area.

Among them, 58361-Minhang, 58365-Jiading, 58362-Baoshan, 58367-Xujiahui, 58462-Songjiang, 58370-Pudong are urban areas, 58460-Jinshan, 58461-Qingpu and 58369-Nanhui are suburban areas, finally 58366-Chongming and 58463-Fengxia are classified as rural station.

In this study, the following 7 indicators will be calculated to evaluate the coincidence of the model with the observed data, namely, MBE, MAE, RMSE, R, R^2, HR and IOA. The HR threshold value is set as 2°C (Cox et al., 1998) for 2-m temperature and 10% (Lawrence, 2005) for relative humidity as the desired accuracy.
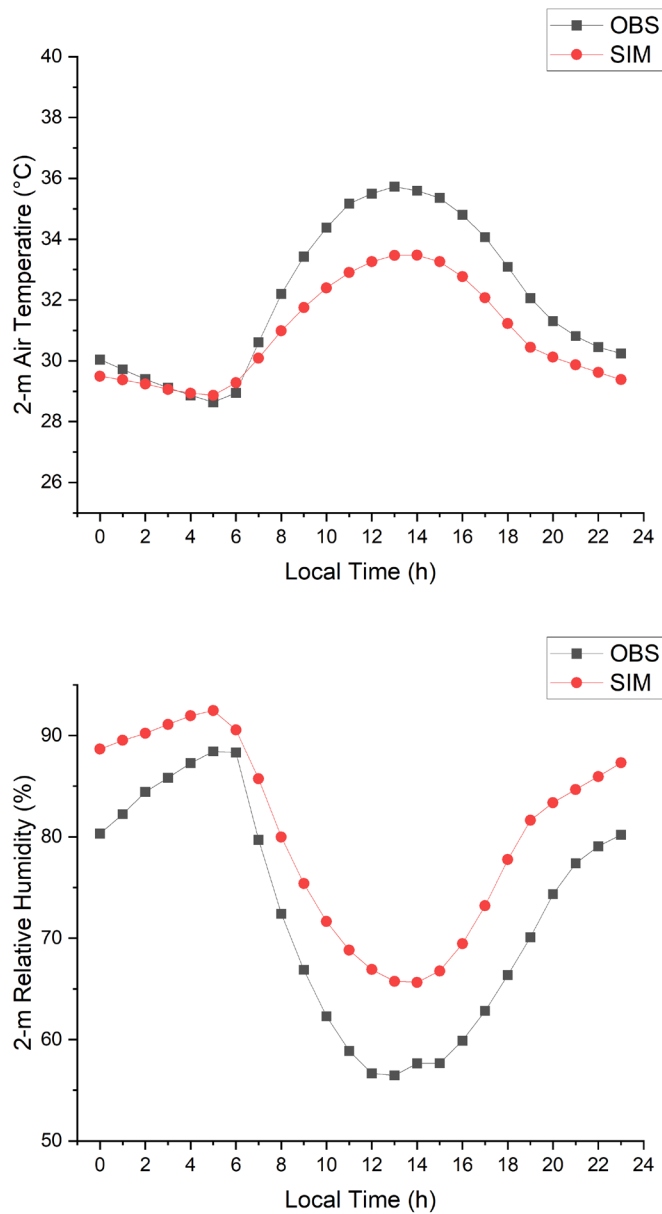
Figure 6.7 Model evaluation for case 0 in averaged 24 hours

Table 6.3 Model evaluation statistics for near surface variables

Variables	Statistics Indicators	Urban	Sub Urban	Rural
T2m (°C)	MBE	-1.475	-0.832	-1.215
	MAE	1.52	0.864	1.297
	RMSE	1.87	1.026	1.511
	R	0.991	0.993	0.986
	R^2	0.982	0.986	0.972
	IOA	0.988	0.927	0.894
	HR	0.583	1	0.667
RH (%)	MBE	10.461	4.617	8.521
	MAE	10.461	4.617	8.57
	RMSE	10.793	4.805	9.333
	R	0.984	0.99	0.981
	R^2	0.968	0.98	0.962
	IOA	0.773	0.936	0.853
	HR	0.416	1	0.583

In general, the model can successfully capture the diurnal variation curve of 2-m air temperature (Figure 6.7 and Table 6.3). In terms of correlation coefficient, R for urban as 0.991, Suburb as 0.993 and Rural as 0.986 reflect that the model can well capture the temperature variation trend of three different underlying surface types in Shanghai. However, it should also be noted that there are temperature underestimates (MBE value -1.475, -0.832 and -1.215 for urban, suburban and rural, respectively) in all three cases. This is more evident in urban areas, where RMSE is 1.87, higher than 1.026 of suburbs and 1.511 of rural areas. The underestimation result of rural areas, however, may be

since the observation stations are still being influenced by the underlying surface of urban area.

For the simulation of relative humidity, a similar conclusion can be obtained; the simulation has a good grasp of the diurnal profile of relative humidity. However, the overall relative humidity is still underestimated, which is more obvious with the increase of urban coverage (MBE for urban is -5.683, for sub-urban as -3.136 and for rural as -2.101). This may be due to the overestimation of impervious underlying surface coverage in the model, especially in the main urban area, which fails to fully consider the spatial heterogeneity of urban fractions. For sub-urban and rural space, the simulation effect is better, with RMSE being 5.899, 4.99 and 2.648 for 3 different cases.

On the other hand, the overall underestimation of temperature may also be caused by the lateral boundary data itself. This is because the boundary data is based on the observation data from 1981 to 2015 plus the fluctuation value predicted by GCM. The time selection of the base data has a great influence on the results, while WRF is highly sensitive to the boundary data. If there is a large deviation between the driving data and the observation data, it may lead to systematic error of the simulation results.

For the simulation of relative humidity, a similar conclusion can be obtained; the simulation has a good grasp of the diurnal profile of relative humidity. However, the overall relative humidity is still overestimated, which is more obvious within the urban area (MBE for urban is 10.461, for sub-urban as 4.617 and for rural as 8.521). The underestimation of relative humidity in urban areas may be due to the low simulated temperature. For sub-urban and rural space, the simulation effect is better, with RMSE being 10.793, 4.805 and 9.333 for 3 different cases.

Although there may be systematic deviations, from the overall trend, WRF/Noah/UCM can still accurately grasp the daily variation of 2-m temperature and

2-m relative humidity under this set of driving data, and systematic deviations can be eliminated to a certain extent by making differences between cases, which is also the basis of subsequent experimental results.

6.4 Results and discussion

6.4.1 2-m Temperature and 2-m relative humidity
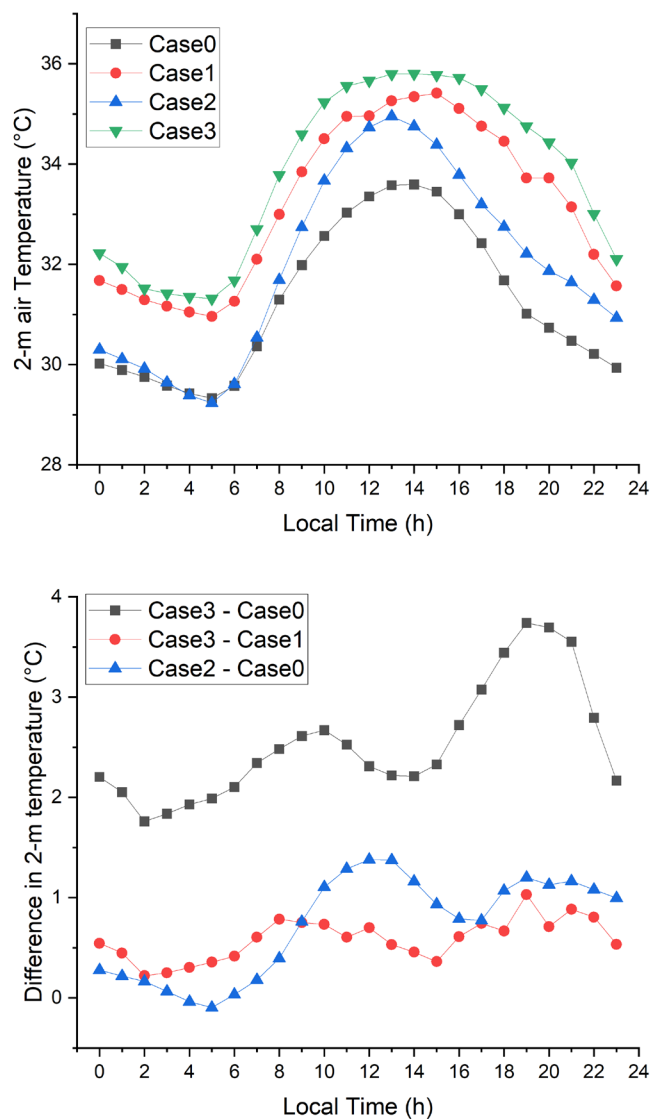
Figure 6.8 Mean diurnal profile of (a) 2-m Temperature (Up panel), (b) 2-m Temperature difference (bottom panel)

The 2-m air temperature mean diurnal profile of the four cases are shown in Figure 6.8a. It can be seen that the 2m temperature of Case123 is higher than that of case0 representing the current case, and Case3 (2030 LULC+2030 RCP8.5) is the highest of all time. This is followed by Case1 (2017LULC+2030RCP8.5) and Case2 (2030LULC+2030RCP4.5). According to the diurnal variation curve, case3 and Case1 adopting the RCP8.5 development path not only have higher daytime temperature, but also have an obvious higher temperature compared with Case2 and Case0 during night time. This indicates that when carbon emission is completely uncontrolled, the temperature in the urban area will be higher than the controlled scheme of all the time. Meanwhile, the temperature of Case3 and Case1 drops more slowly after sunset. The result is that due to the aggressive carbon emission development path of RCP8.5, the temperature in the peripheral areas of the city also increases sufficiently so that the heat absorbed during the day within the urban area cannot be released in time. The subsequent spatial distribution of the UHI corroborates this result.

The contribution of global temperature background and urban development to local climate change of Shanghai in the future can be inferred from Figure 6.8b: The average temperature difference between Case3 and Case1 is 0.58°C. As the same 2030 RCP 8.5 scenario is used as lateral boundary condition for Case3 and Case1, this part of temperature difference (0.58°C) completely comes from the future urbanization process in 2030. Similarly, the average difference between case1 and case0 is 1.95°C, which comes from the difference between the current lateral boundary condition and 2030 RCP 8.5 pathway. By comparing the two results, it can be inferred that under the RCP8.5 development path, 23% of the temperature increase in July in 2030 in Shanghai will be contributed by urbanization on average, while 77% will be contributed by global warming. This result is consistent with Doan s prediction of Ho Chi Minh City in the

2050s (Doan and Kusaka, 2019).

On the other hand, compared with the case representing the current situation, the average temperature rise of Case 3 is 2.53°C, while the average temperature rise of Case 2 is only 0.72°C. The huge difference between the two case3 is due to different RCP global warming pathway. This fully shows that if carbon emissions can be gently controlled as RCP4.5, future threats to urban climate will be greatly reduced.
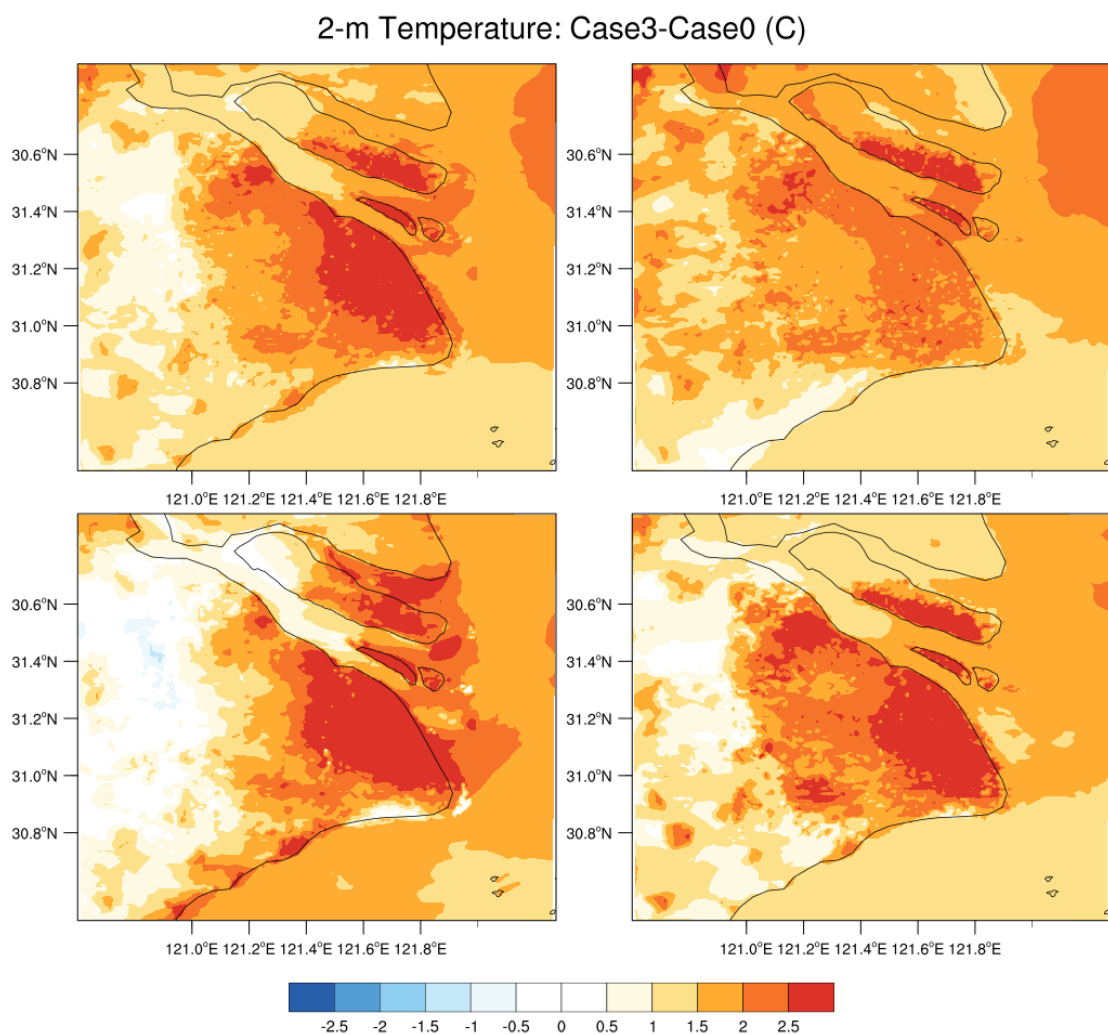
Figure 6.9 Spatiotemporal variation of 2-m air temperature difference of case3 and case0 above the area during: (a) 24h averaged time (b) morning: 0000-0700LST (up right figure), (c) day time: 0800 - 1500LST (bottom left figure) and (d) night time: 1600-2300LST (bottom right figure)

Figure 6.9a shows the spatial distribution of 2-m air temperature difference of case3 and case0. Generally speaking, the region with greater temperature increase is concentrated in Pudong area, and the temperature rise gradient gradually decreases westward. Figure 6.9b represents the temperature change before the sun rises, and the overall temperature rise is the lowest among the three periods. From the spatial distribution at noon (Figure 6.9c), the large cropland area in the west of Shanghai showed barely change in temperature difference, indicating that the rural area far away from the city had no significant effect on global warming compared with the urban area.
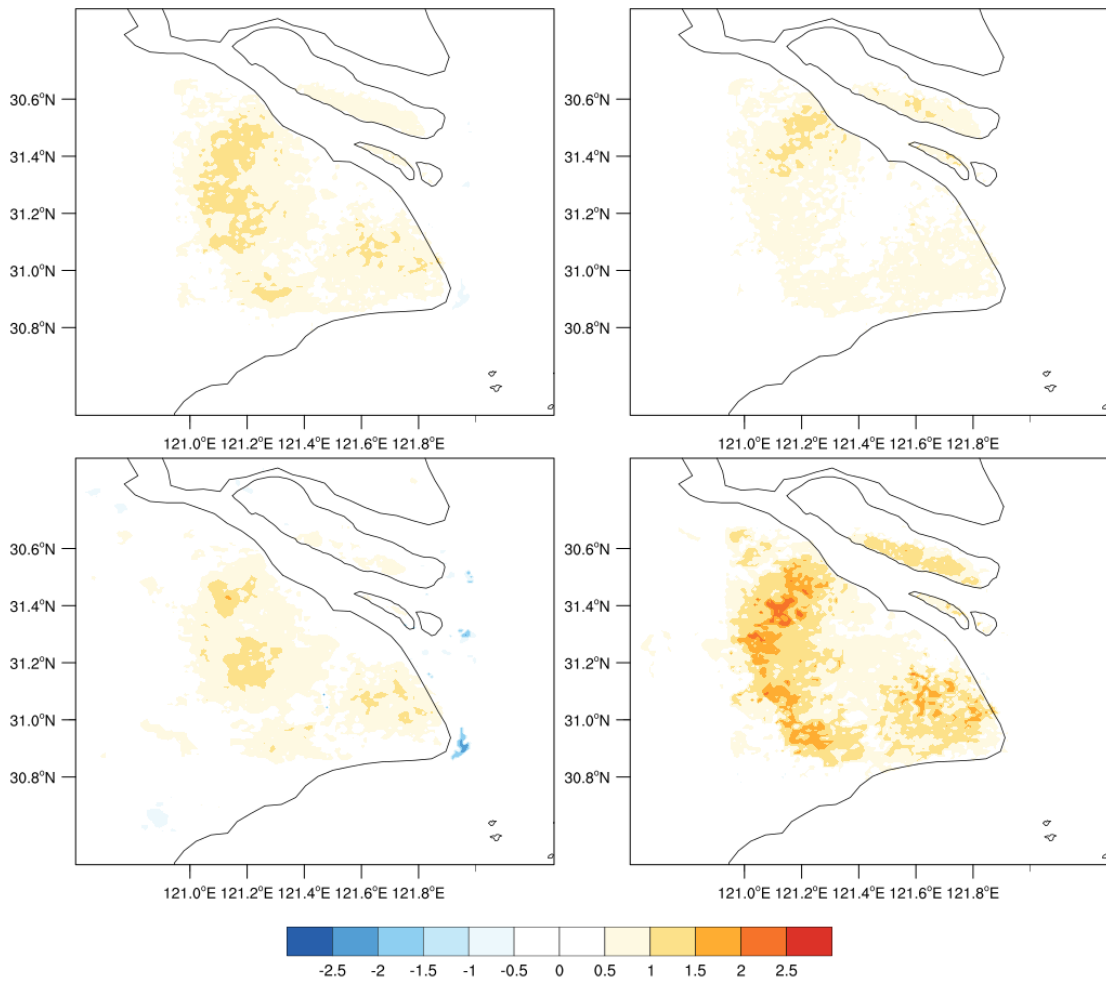
Figure 6.10 Spatiotemporal variation of 2-m air temperature difference of case3 and case1 above the area during: (a) 24h averaged time (b) morning: 0000-0700LST (up right figure), (c) day time: 0800 -1500LST (bottom left figure) and (d) night time: 1600-2300LST (bottom right figure)

The lateral boundary conditions of 2030 RCP 8.5 are applied in both Case3 and Case1, thus the spatial variation is completely caused by the further development of urbanization (i.e., the change of LULC). It can be clearly seen from Figure 6.10 that the temperature difference is almost completely concentrate upon the newly added urban areas, which is also in line with expectations. In terms of temporal variation, Figure 6.10d shows the largest temperature difference, indicating a huge temperature rise of newly added urban areas after sunset, which is mainly because land use in this area

changes from cropland to urban area. Given that urban surface materials are known for high thermal diffusivity and heat retention, it is resealable to notice such a temperature increasement.

Figure 6.11 Spatiotemporal variation of 2-m relative humidity difference of case3 and case1 above the area during: (a) 24h averaged time (b) morning: 0000-0700LST (up right figure), (c) day time: 0800 -1500LST (bottom left figure) and (d) night time: 1600-2300LST (bottom right figure)

The variation trend of relative humidity is almost completely opposite to that of 2-m temperature. Taking Case3-Case0 as an example (Figure 6.11), under the development path of RCP8.5, with the further expansion of urbanization, the relative

humidity in urban areas will be further reduced, especially in newly expanded urban areas. The centre area of relative humidity reduction is also concentrated in Pudong district. While in the cropland to the west of Shanghai, RH increased to some extent can be noticed. Relative humidity is closely related to the health of residents and Thermal heat index (THI). Subsequent THI analysis will further explore the changes of relative humidity and 2-m temperature under different conditions

6.4.2 UHII and human comfort

The difference in T2m between urban and rural areas is known as the urban heat island intensity (UHII). During the daytime, a certain percentage of the solar irradiation flux is retained on the urban surface. Through natural convection and radiation processes, the retained heat flux is radiated to the directly covered canopy, which is particularly important at night. In contrast, rural areas have higher vegetation fractions, higher plant respiration and transpiration, and higher surface canopy moisture effectiveness, which has a considerable cooling effect on the lower boundary layer. This leads to differences in canopy temperature between urban and rural areas.

According to the simulation results (Figure 6.12), it can be seen that either the continuous expansion of urbanization or the increasingly serious global warming will lead to the aggravation of UHII
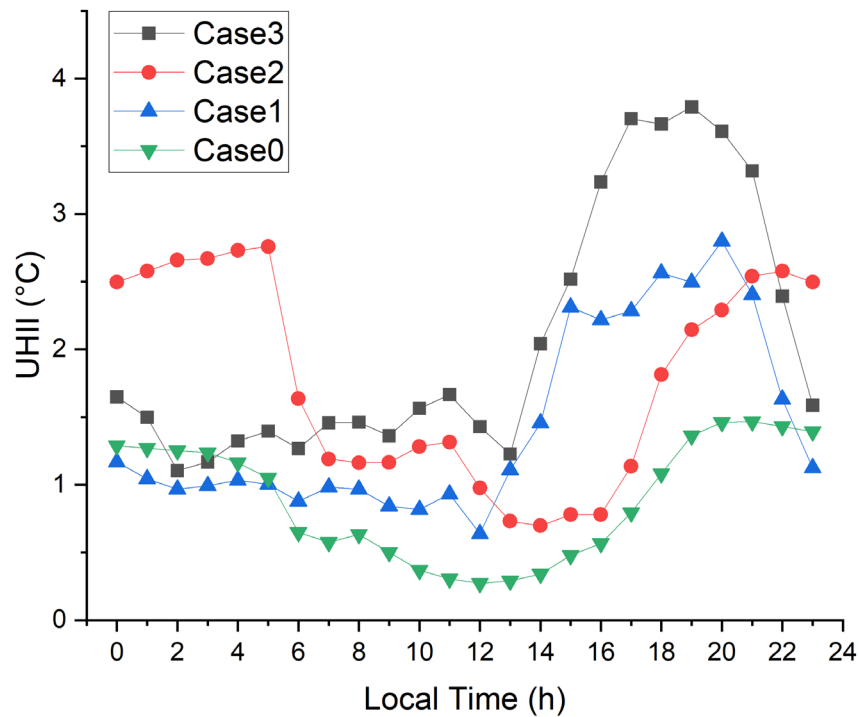
Figure 6.12 Mean diurnal profile of Urban heat island intensity (UHII) in °C

Mean UHI intensities of approximately 0.88, 1.44, 1.77 and 2.06°C are observed for cases 0, 1, 2 and 3, respectively. Minimum (~0.27, ~0.63 ~0.69 and 1.10°C) and maximum (~1.47, ~2.79, ~2.65 and ~3.79°C) UHII were observed for cases 0, 1, 2 and 3 at 0900 and around 2000 LST (Figure 6.12), respectively.

In order to further distinguish the respective contributions of global warming and urbanization to UHII, the changes in heat island intensity of Case0, Case1 and Case3 are taken as examples. The UHII increase from 0.88°C of Case0 to 1.44°C of Case1 is entirely due to the global warming trend under 2030 RCP 8.5 pathway, while the UHII development from 1.44°C of Case1 to 2.06°C of Case3 is entirely due to the further expansion of urbanization. Therefore, it can be inferred that the heat island effect of Shanghai will increase by 1.18°C on average by 2030 if the urbanization process is considered and the RCP8.5 path is followed, of which the contribution from

143

urbanization accounts for 52.5%(0.62°C), while the contribution from global warming is 47.5% (0.56°C).

At the same time, since the trend of global warming in the RCP4.5 development pathway is slower than that of RCP8.5, but the absolute contribution of urbanization to UHII will not decrease accordingly, it can be inferred that the contribution of urbanization to UHII will further increase to 69.6% under the RCP4.5 development pathway.

On the other hand, the expansion of urbanization can rapidly accelerate the rapid increase of UHI intensity. On the contrary, it can also act as an effective mitigation effect for UHII by curbing the rapid expansion of urban construction, i.e., increasing the area covered by water and vegetation, or increasing green roofs and other green urban facilities (Morris et al., 2016; Larsen, 2015; Papangelis et al., 2012). The verification of such conjecture can be further simulated by modifying the parameters of underlying surface or urban area.
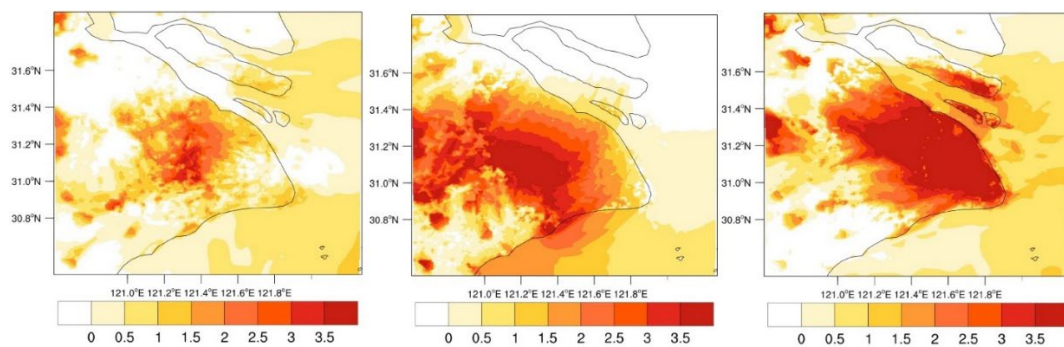
Figure 6.13 Spatial variation of UHII (°C) at 2000 LST for (a) Case1 (left panel), (b) Case 2 (middle panel) and (c) Case 3 (right panel)

The spatial distribution of UHI in different cases also follows certain patterns. Figure 6.13a represents the distribution of UHI on the underlying surface of the current Shanghai city, which is much smaller than Case2 and Case3 in terms of coverage area.

144

In particular, UHI in Case3 covers not only almost most urban areas of Shanghai, but also some suburbs at its edge. Compared with Case3, the heat island distribution of Case2 is more southwest, which may be caused by strong sea and land winds in the background field during the simulation time selection, leading downward wind shift of heat island centre. In general, the intensity of heat island effect increases with global warming and urban expansion, and the coverage area of heat island effect is more affected by urbanization.
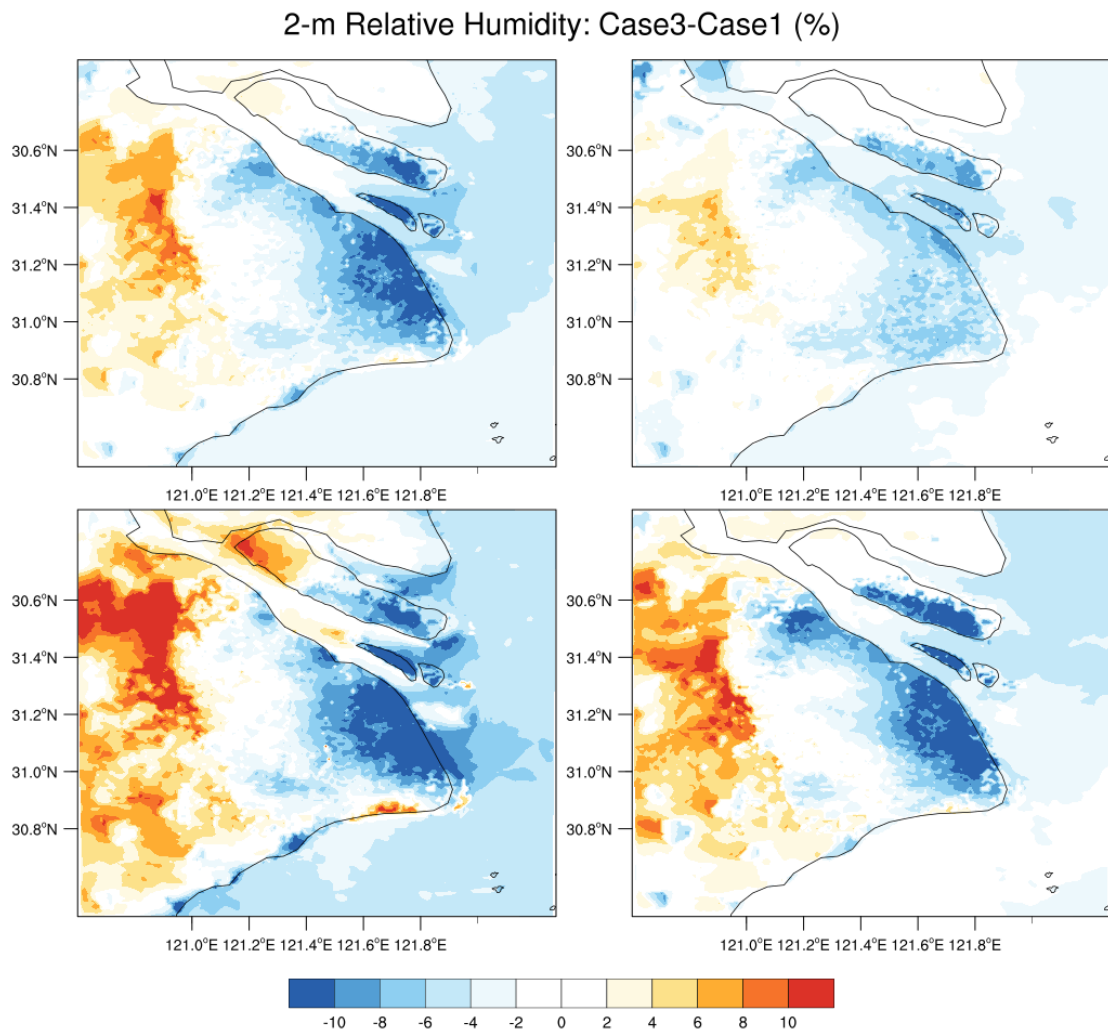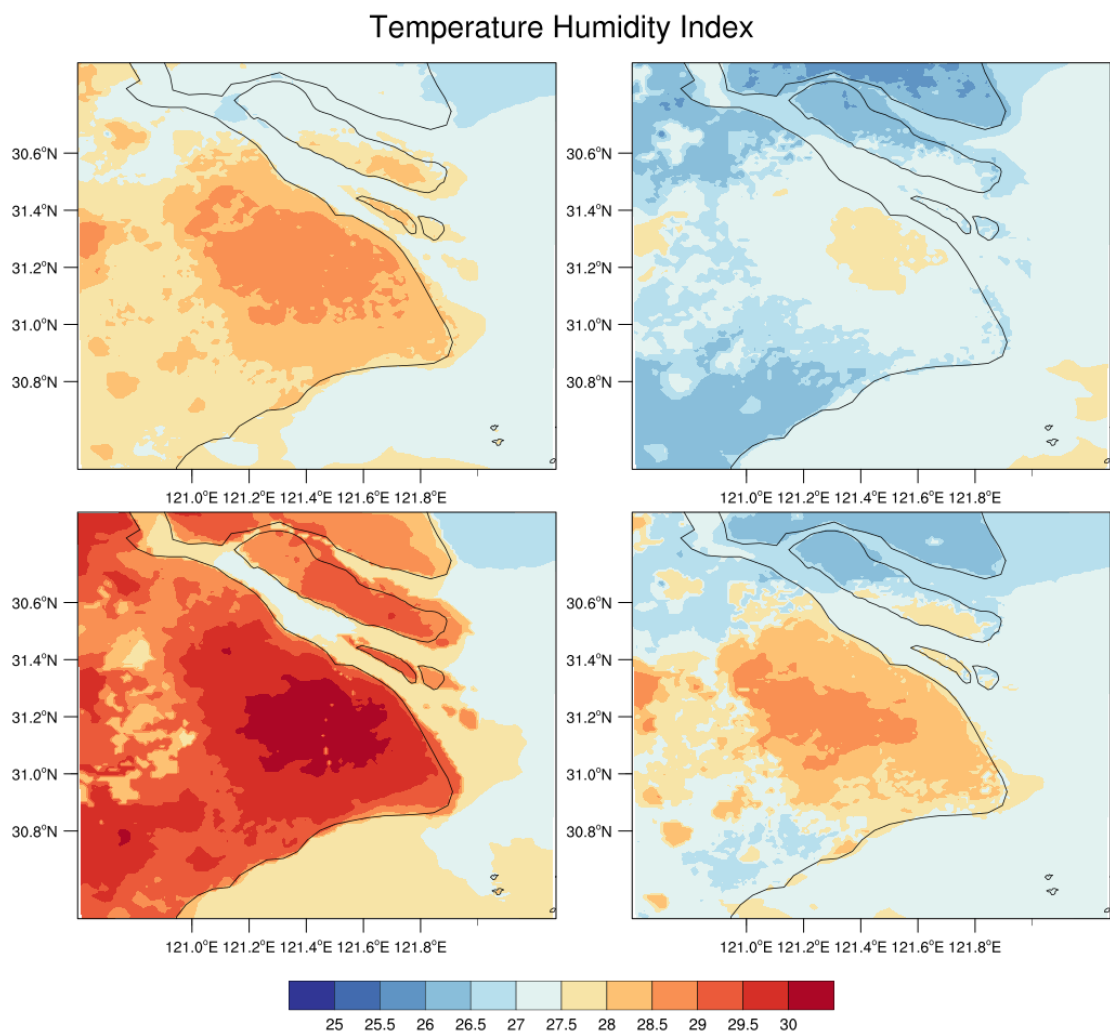

Figure 6.14 Spatiotemporal variation of temperature humidity index of case3 above the area during: (a) 24h averaged time (b) morning: 0000-0700LST (up right figure), (c) day time: 0800 -1500LST (bottom left figure) and (d) night time: 1600-2300LST (bottom right figure)

The relationship between local microclimate status and human thermal sensation has resulted in the development of several biometeorological indices that have been used to define human thermal comfort levels. The thermohydrometric index, THI (Thom, 1958), was chosen to analyse the acquired data since it is recognized to properly reflect variations in air temperature and humidity caused by urban landscapes. The temperature humidity index is easily calculated from the air temperature (°C) and relative humidity (%) using McGregor and Nieuwolt's equation (McGregor et al., 1998):

$$THI = \ 0.8 \times T_a + \frac{RH \times T_a}{500}$$

where Ta is air temperature simulated in °C and RH is relative humidity in percentage.

The thermal environment can be divided into different grades according to the values obtained by THI calculation. THI greater than 26.5 belongs to very hot and THI greater than 30 belongs to Torrid condition.

Figure. 6.14 shows THI distribution in different time periods during case3 simulation. Figure 6.14c is particularly noteworthy, which indicates that in case of Case3, Torrid Condition of a large area will appear in Shanghai during 0800-1500LST. In particular, the THI of the core urban areas is expected to exceed 30, and the situation is expected to worsen if extreme heat is considered instead of the average situation.

The impact of extreme heat on the human health cannot be ignored, including increased hospitalizations and emergency department visits, increased deaths from cardiopulmonary and other diseases, adverse pregnancy and childbirth outcomes, and other vulnerable groups that are more vulnerable to extreme heat. More than 356,000 deaths were linked to heat in 2019, and the number is expected to grow as global

temperatures rise (Ebi et al. 2021; Jay et al. 2021). Zhao Xinpeng calculated the number of hospitalized patients and the frequency of extreme weather in Shanghai and concluded that the average number of hospitalized patients will increase by 1.266 (95% confidence intervals: 1.074 -- 1.493) after the temperature exceeds 33.1°C (Zhao et al. 2017).

Although case3 represents a destructive development path of uncontrolled carbon emissions, in fact, the average THI in case2 (2030 RCP 4.5) is 2.45 lower than that in case3 (2030 RCP 8.5). Torrid areas also yield 35.1% less than coverage in Case3. Result from Case1 compared with Case3, the change of torrid coverage area is completely due to the expansion of urbanization, and the average THI decreased by only 1.67, which is less than the difference between Case2-Case3.This indicates the components of THI parameter are greatly affected by the global warming trend, meaning the worldwide energy conservation, emission reduction and carbon neutrality actions are essential to build a human comfort friendly environment.

If 33°C is considered as the threshold of extreme weather, in Case3, the duration of the average temperature greater than 33 is from 0700LST to 2300LST, while in Case2 it is 0800LST to 2230LST (Case1 and Case3 have the same length of time but cover a smaller area). Although this result is relevant to the simulation period choosing, it is still enough to show that the extreme weather of Case2 is less frequent than that of Case3, which indicates that global warming matters more even for the extreme weather happens to a single city like Shanghai that put threat to human thermal health.

6.5 Conclusion

In this study, a dynamic downscaling method was used to simulate the future urban climate state of Shanghai under different development paths in 2030 with coupled WRF/Noah/UCM model. Lateral boundary condition dataset is made using Pseudo Global Warming method to eliminate system bias. Through the hindcast simulation of 2017 data, it is confirmed that the lateral boundary driven data and model can well capture the current climate pattern of Shanghai. Meanwhile, it is also found that the simulation had a lower estimate of air temperature than the observation.

After comparative analysis of four groups of experiments, taking the average simulated temperature in July 2030 as an example, RCP8.5 shows the maximum temperature increase of 2.53°C, which is caused by the joint effect of urbanization and global warming. Among them, global warming contributes more, up to 77%, while urbanization contributes only 23%. RCP4.5 represents a controlled carbon emission development path, which is widely considered to be the global maximum in 2035, in which the temperature increase shown in the simulation is reduced to 0.72°C.

In the simulation of UHI, urbanization and global warming also show overlapping effects, while the impact of urbanization is more obvious. The impact of urbanization is not only reflected in the contribution of tree branches, but especially in the coverage area of heat island effect. Under the 2030 RCP8.5 path, UHII will increase by 1.18°C, 52.5% of which is due to the contribution of urbanization development. On the other hand, this suggests that increasing the area covered by water and vegetation or increasing green roofs and other green urban facilities may lead to significant reduction of UHI.

Residents thermal comfort condition under RCP8.5 path simulation is very pessimistic, although absolute numerical prediction cannot be verified, but the

emergence of extreme high temperature and extreme hot situation probability will be greater than the other 3 simulation settings. Especially in summer daytime, the whole city will be covered in the extreme hot environment, puts forward the severe challenge to outdoor work. Simulations using the RCP4.5 path showed significant relief of THI, with an average value of 2.45 lower than the RCP8.5 scenarios. Furthermore, sensitivity analysis shows that the coverage of extreme weather is related to the development of urbanization, but the intensity and duration of extreme weather are more affected by global warming.

Findings of this study will help urban planners, designers, ecologists, and governmental and non-governmental bodies to plan and update current guidelines and design methods for building sustainable and liveable cities.

7 Discussion and Conclusion

This study attempts to achieve four core research objectives :(1) to evaluate the suitability of WRF/NOAH/UCM coupling model for climatological investigation in Shanghai; (2) To investigate the urban climatology of Shanghai using the validated model above mentioned; (3) To study the climate change and its adaptation to urbanization in Shanghai since the 21st century (the impact of Shanghai urbanization on local climate); (4) Design ideal experiments to predict and analyse the local climate status in Shanghai in 2030.

In chapter 4, the setup of coupled WRF/Noah/UCM is introduced in detail, and the reliability of the coupled model after replacing the underlying surface data set and other simulation parameters is verified by comparing the experimental and observation data and the results showed that the simulations were in good agreement and correlation with the observed data. The simulation results for Shanghai show that LULC change, and AH have great influence on the simulation results. The surface energy balance is dominated by direct solar radiation during the day, while intercepted longwave radiation, re-radiative heat fluxes and anthropogenic heat release are most prominent in the early and late hours. The average maximum UHIIs observed in the simulation is 4.15ºC, and its daily variation is closely related to solar radiation. Areas with low urban settlement intensity experienced a moderate urban heat island. This is due to the presence of high vegetation and therefore high humidity availability (RH) relative to other urban layers. In this section, the first and second objectives are achieved.

As the model performance being proved, four ideal simulation experiments are designed in the fifth chapter with 4 different urban underlying surface datasets in different year cases (2000,2010, and 2017) to represent the urbanization process of Shanghai. The influence of urbanization on local climate of Shanghai is comparatively

analysed, and the sensitivity of heat island effect and residents' comfort to urbanization is also analysed. In this part, the thermal urban climate of Shanghai was successfully identified. The model results show that the distribution of 2m Temperature is extremely sensitive to the changes of surface due to urbanization. UHI increased by 2.08°C during the simulation period. The frequency and coverage of extreme heat increased by 11.2 percent, and the duration increased by two hours. Sensitivity analysis shows that the urbanization process has relatively little influence on sensible heat flux and wind speed in the simulated area. The simulation in this part describes the impact of Shanghai urbanization on local climate which is exactly the fourth goal in this research and leaves the problem with future projections for further discussed in chapter 6.

Based on chapter 5, the sixth chapter simulates the urban environment of Shanghai in 2030.The prediction and simulation of the future climate in Shanghai in 2030 show that the thermal environment will face great challenges in the future, especially under the RCP8.5 development path. The average temperature will rise as high as 2.53°C, and the heat island intensity will also increase by 1.18°C, which will have a significant destructive impact on the thermal comfort of residents. The impact of urbanization development cannot be ignored, in which 23% of temperature rise and 54.5% of heat island intensity are caused by urbanization. In addition, the area covered by heat island intensity is almost entirely determined by urbanization scale. Sensitivity analysis also indicates that the coverage of extreme weather is more related to the development of urbanization, while the intensity and duration of extreme weather are mainly affected by global warming. Overall, the simulation results show that the RCP4.5 simulation results are significantly moderated compared to RCP8.5, with a significant decrease in both temperature rise, UHI, and the occurrence of extreme weather, which should be the recommended path for future world development.

In general, the focus of this study is to verify the simulation effect of WRF/Noah/UCM, to learn the urban climate of Shanghai, and to retrospectively analyse the impact of urbanization on the urban climate of Shanghai. Finally, the simulation is extended to different future scenarios in 2030. The urban climates of Shanghai under different urbanization pathways and different future global warming scenarios are analysed.

There are still some unsolved problems in this research, such as the LULC data used in the fourth and sixth chapter of this thesis is not the same one in the fifth chapter, which makes the whole linkage relatively unclear. The reason is that it is hard to find a whole set of LULC dataset that covers different periods of Shanghai, especially to distinguish the city part between high and low density, let along the future LULC data projections. Therefore, each chapter has to re-validate the dataset used in this thesis.

Local Climate Zoon dataset (Ching et al., 2018) was once considered in this research as it allows us to make our own LULC dataset with a more detailed description of the underlying surface by supervised machine learning algorism. The advantage of this method is that saving lots of time making a prefect LULC map for research purpose. But at the same time, the introduction of more physical parameters (Local climate zoon dataset contains 10 different city underlying types while the default number of category for that in WRF is only 3) may also lead to distortion of simulation results, while more precise models require more measured data as the basis for parameter setting. It is not guaranteed that the result will be better. Also, the integration of that will need some modification of the source code of WRF. However, in the latest update of WRF 4, there are APIs that allow you easily combine local climate zoon dataset with the default dataset together, the only problem is that you cannot generate future LULC using this local climate zoon method for now. As this community still growing fast, this could be

something to look forward to in the future study process.

In the settings of simulations, the processing of AH is only allocated with fixed values in this thesis. Although the calculation of AH is speculated based on reasonable conditions, such assumptions are not the most ideal way to deal with AH. A more detailed processing method is to make a two-dimensional discrete distribution of AH based on more refined LULC data, which cannot be achieved in this study as LULC accuracy and discrimination are not high enough. This as well could be improved along with better LULC dataset mentioned above.

In terms of simulation results, because WRF has endogenous defects in the simulation of wind fields, especially for mesoscale simulations. Therefore, it is more difficult to guarantee the accuracy of the simulation effect of wind fields. In this study, the analysis of wind field simulation is not outstanding, and the simulation results show considerable uncertainty, which is different from the simulation of temperature field and relative humidity. For this point, a possible improvement method is to use data assimilation for a better result on hindcast simulations (like chapter 4 and 5), but this method cannot be used for future prediction (chapter 6). In order to ensure the coherence of the whole study, data assimilation was not used, and in this case how to improve the effect of wind field simulation is an important direction for further research.

I think the study expounds the deductive process of Shanghai urban climate from the perspective of temporal change (past, present, and future), the analysis discusses the impact of Shanghai local climate from both global warming and urbanization process. The sensitivity analysis of future scenarios illustrates the importance of controlling the global warming trend for local urban climate and shows the drastic changes of residents' thermal comfort under different scenarios, filling the gap in this field of research. Future research should be directed towards more refined LULC datasets and further

optimization of simulation results.

8 References

Adachi, S. A., Kimura, F., Kusaka, H., Duda, M. G., Yamagata, Y., Seya, H., Nakamichi, K. & Aoyagi, T. 2014. Moderation of summertime heat island phenomena via modification of the urban form in the Tokyo metropolitan area. *Journal of Applied Meteorology and Climatology,* 53**,** 1886-1900.

Adachi, S. A., Kimura, F., Kusaka, H., Inoue, T. & Ueda, H. 2012. Comparison of the impact of global climate changes and urbanization on summertime future climate in the Tokyo metropolitan area. *Journal of Applied Meteorology and Climatology,* 51**,** 1441-1454.

Alexader, B., Luisa, T. & Molina, M. Gauss (2016). Megacities, air quality and climate. *Atmospheric Environment,* 126**,** 235-249.

Argüeso, D., Evans, J. P., Fita, L. & Bormann, K. J. 2014. Temperature response to future urbanization and climate change. *Climate Dynamics,* 42**,** 2183-2199.

Balling, R. C. & Brazel, S. W. 1988. High-resolution surface temperature patterns in a complex urban terrain. *Photogrammetric Engineering & Remote Sensing,* 54**,** 1289-1293.

Bernstein, L., Bosch, P., Canziani, O., Chen, Z., Christ, R. & Riahi, K. 2008. IPCC, 2007: climate change 2007: synthesis report. IPCC.

Bian, T., Ren, G. & Yue, Y. 2017. Effect of urbanization on land-surface temperature at an urban climate station in North China. *Boundary-layer meteorology,* 165**,** 553-567.

Blaschke, T., Hay, G. J., Kelly, M., Lang, S., Hofmann, P., Addink, E., Feitosa, R. Q., Van Der Meer, F., Van Der Werff, H. & Van Coillie, F. 2014. Geographic object-based image analysis–towards a new paradigm. *ISPRS journal of photogrammetry and remote sensing,* 87**,** 180-191.

Bohnenstengel, S., Hamilton, I., Davies, M. & Belcher, S. 2014. Impact of anthropogenic heat emissions on London's temperatures. *Quarterly Journal of the Royal Meteorological Society,* 140**,** 687-698.

Brasseur, G. P., Prinn, R. G. & Pszenny, A. A. 2003. *Atmospheric chemistry in a changing world: an integration and synthesis of a decade of tropospheric chemistry research*, Springer.

Breiman, L. 2001. Random forests. *Machine learning,* 45**,** 5-32.

Change, I. C. 2007. Synthesis Report An Assessment of the Intergovernmental Panel on Climate Change. *IPCC Plenary XXVII: Valencia, Spain*.

Changnon Jr, S. A. 1979. Rainfall changes in summer caused by St. Louis. *Science,* 205**,** 402-404.

Chapman, S., Watson, J. & Mcalpine, C. 2016. Large seasonal and diurnal anthropogenic heat flux across four Australian cities. *Journal of Southern Hemisphere Earth Systems Science,* 66**,** 342-360.

Chapman, S., Watson, J. E., Salazar, A., Thatcher, M. & Mcalpine, C. A. 2017. The impact of urbanization and climate change on urban temperatures: a systematic review. *Landscape Ecology,* 32**,** 1921-1935.

Chen, F., Janjić, Z. & Mitchell, K. 1997. Impact of atmospheric surface-layer parameterizations in the new land-surface scheme of the NCEP mesoscale Eta model. *Boundary-Layer Meteorology,* 85**,** 391-421.

Chen, F., Kusaka, H., Bornstein, R., Ching, J., Grimmond, C., Grossman-Clarke, S., Loridan, T., Manning, K. W., Martilli, A. & Miao, S. 2011. The integrated WRF/urban modelling system: development, evaluation, and applications to urban environmental problems. *International Journal of Climatology,* 31**,** 273-288.

Chen, F., Kusaka, H., Tewari, M., Bao, J. & Hirakuchi, H. Utilizing the coupled WRF/LSM/Urban modeling system with detailed urban classification to simulate the urban heat island phenomena over the Greater Houston area. Fifth Symposium on the Urban Environment, 2004. American Meteorological Society Vancouver, BC, Canada, 9-11.

Chen, F., Mitchell, K., Schaake, J., Xue, Y., Pan, H. L., Koren, V., Duan, Q. Y., Ek, M. & Betts, A. 1996. Modeling of land surface evaporation by four schemes and comparison with FIFE observations. *Journal of Geophysical Research: Atmospheres,* 101**,** 7251-7268.

Chen, F., Yang, X. & Zhu, W. 2014. WRF simulations of urban heat island under hot-weather synoptic conditions: The case study of Hangzhou City, China. *Atmospheric research,* 138**,** 364-377.

Chen, L. & Frauenfeld, O. W. 2016. Impacts of urbanization on future climate in China. *Climate dynamics,* 47**,** 345-357.

Chen, L., Jiang, R. & Xiang, W.-N. 2016. Surface heat island in Shanghai and its relationship with urban development from 1989 to 2013. *Advances in Meteorology,* 2016.

Chen, Y., Bai, Y., Liu, H., Alatalo, J. M. & Jiang, B. 2020. Temporal variations in ambient air quality indicators in Shanghai municipality, China. *Scientific RepoRtS,* 10**,** 1-11.

Chen, Y., Jiang, W., Zhang, N., He, X. & Zhou, R. 2009. Numerical simulation of the anthropogenic heat effect on urban boundary layer structure. *Theoretical and applied climatology,* 97**,** 123-134.

Conry, P., Sharma, A., Potosnak, M. J., Leo, L. S., Bensman, E., Hellmann, J. J. & Fernando, H. J. 2015. Chicago's heat island and climate change: Bridging the scales via dynamical downscaling. *Journal of Applied Meteorology and*

Climatology, 54**,** 1430-1448.

Cui, L. & Shi, J. 2012. Urbanization and its environmental effects in Shanghai, China. *Urban Climate,* 2**,** 1-15.

Darmanto, N. S., Varquez, A. C. G., Kawano, N. & Kanda, M. 2019. Future urban climate projection in a tropical megacity based on global climate change and local urbanization scenarios. *Urban Climate,* 29**,** 100482.

Doan, Q.-V., Kusaka, H. & Ho, Q.-B. 2016. Impact of future urbanization on temperature and thermal comfort index in a developing tropical city: Ho Chi Minh City. *Urban Climate,* 17**,** 20-31.

Doan, V. Q., Kusaka, H. & Nguyen, T. M. 2019. Roles of past, present, and future land use and anthropogenic heat release changes on urban heat island effects in Hanoi, Vietnam: Numerical experiments with a regional climate model. *Sustainable Cities and Society,* 47**,** 101479.

Du, H., Wang, D., Wang, Y., Zhao, X., Qin, F., Jiang, H. & Cai, Y. 2016. Influences of land cover types, meteorological conditions, anthropogenic heat and urban area on surface urban heat island in the Yangtze River Delta Urban Agglomeration. *Science of the Total Environment,* 571**,** 461-470.

Dudhia, J., Hong, S.-Y. & Lim, K.-S. 2008. A new method for representing mixed-phase particle fall speeds in bulk microphysics parameterizations. *Journal of the Meteorological Society of Japan. Ser. II,* 86**,** 33-44.

Ebi, K. L., Capon, A., Berry, P., Broderick, C., De Dear, R., Havenith, G., Honda, Y., Kovats, R. S., Ma, W. & Malik, A. 2021. Hot weather and heat extremes: health risks. *The Lancet,* 398**,** 698-708.

Economic, D. O. 2008. *World Population Prospects: The 2006 Revision-Sex and Age Distribution of the World Population*, United Nations Publications.

Elmqvist, T., Fragkias, M., Goodness, J., Güneralp, B., Marcotullio, P. J., Mcdonald, R. I., Parnell, S., Schewenius, M., Sendstad, M. & Seto, K. C. 2013. Stewardship of the biosphere in the urban era. *Urbanization, biodiversity and ecosystem services: Challenges and opportunities.* Springer, Dordrecht.

Estoque, R. C. & Murayama, Y. 2017. Trends and spatial patterns of urbanization in Asia and Africa: a comparative analysis. *Urban Development in Asia and Africa.* Springer.

Fang, C., Liu, H., Li, G., Sun, D. & Miao, Z. 2015. Estimating the impact of urbanization on air quality in China using spatial regression models. *Sustainability,* 7**,** 15570-15592.

Farrell, K. & Westlund, H. 2018. China's rapid urban ascent: an examination into the components of urban growth. *Asian Geographer,* 35**,** 85-106.

Fischer, J., Lindenmayer, D. B. & Manning, A. D. 2006. Biodiversity, ecosystem

function, and resilience: ten guiding principles for commodity production landscapes. *Frontiers in Ecology and the Environment,* 4**,** 80-86.

Georgescu, M., Morefield, P. E., Bierwagen, B. G. & Weaver, C. P. 2014. Urban adaptation can roll back warming of emerging megapolitan regions. *Proceedings of the National Academy of Sciences,* 111**,** 2909-2914.

Gill, S. E., Handley, J. F., Ennos, A. R. & Pauleit, S. 2007. Adapting cities for climate change: the role of the green infrastructure. *Built environment,* 33**,** 115-133.

Golaz, J. C., Horowitz, L. W. & Levy, H. 2013. Cloud tuning in a coupled climate model: Impact on 20th century warming. *Geophysical Research Letters,* 40**,** 2246-2251.

Goldewijk, K. K. 2001. Estimating global land use change over the past 300 years: the HYDE database. *Global biogeochemical cycles,* 15**,** 417-433.

Gong, H., Simwanda, M. & Murayama, Y. 2017. An internet-based GIS platform providing data for visualization and spatial analysis of urbanization in major Asian and African cities. *ISPRS International Journal of Geo-Information,* 6**,** 257.

González-Aparicio, I., Baklanov, A., Hidalgo, J., Korsholm, U., Nuterman, R. & Mahura, A. 2014. Impact of city expansion and increased heat fluxes scenarios on the urban boundary layer of Bilbao using Enviro-HIRLAM. *Urban Climate,* 10**,** 831-845.

Grimmond, S. 2007. Urbanization and global environmental change: local effects of urban warming. *The Geographical Journal,* 173**,** 83-88.

Grossman-Clarke, S., Zehnder, J. A., Loridan, T. & Grimmond, C. S. B. 2010. Contribution of land use changes to near-surface air temperatures during recent summer extreme heat events in the Phoenix metropolitan area. *Journal of Applied Meteorology and Climatology,* 49**,** 1649-1664.

Guo, F., Wang, S. & Zhu, P. Numerical urban climate simulation and preliminary planning strategies of dalian city based on WRF model. The 9th International Conference of Urban Climate, Toulouse, France, 2015.

Hamdi, R., Giot, O., De Troch, R., Deckmyn, A. & Termonia, P. 2015. Future climate of Brussels and Paris for the 2050s under the A1B scenario. *Urban climate,* 12**,** 160-182.

Hamdi, R., Kusaka, H., Doan, Q.-V., Cai, P., He, H., Luo, G., Kuang, W., Caluwaerts, S., Duchêne, F. & Van Schaeybroek, B. 2020. The state-of-the-art of urban climate change modeling and observations. *Earth Systems and Environment,* 4**,** 631-646.

Hamdi, R., Van De Vyver, H., De Troch, R. & Termonia, P. 2014. Assessment of three dynamical urban climate downscaling methods: Brussels's future urban heat island under an A1B emission scenario. *International Journal of Climatology,* 34**,** 978-999.

Han, L., Zhou, W., Li, W. & Li, L. 2014. Impact of urbanization level on urban air quality: A case of fine particles (PM2. 5) in Chinese cities. *Environmental Pollution,* 194**,** 163-170.

Hay, G. J. & Castilla, G. 2008. Geographic Object-Based Image Analysis (GEOBIA): A new name for a new discipline. *Object-based image analysis.* Springer.

Hoffmann, P. & Schlünzen, K. H. 2013. Weather pattern classification to represent the urban heat island in present and future climate. *Journal of Applied Meteorology and Climatology,* 52**,** 2699-2714.

Hong, S.-Y., Dudhia, J. & Chen, S.-H. 2004. A revised approach to ice microphysical processes for the bulk parameterization of clouds and precipitation. *Monthly weather review,* 132**,** 103-120.

Hong, S.-Y., Noh, Y. & Dudhia, J. 2006. A new vertical diffusion package with an explicit treatment of entrainment processes. *Monthly weather review,* 134**,** 2318-2341.

Howard, E. 1965. *Garden cities of to-morrow*, Mit Press.

Ichinose, T., Shimodozono, K. & Hanaki, K. 1999. Impact of anthropogenic heat on urban climate in Tokyo. *Atmospheric Environment,* 33**,** 3897-3909.

IPCC, A. 2007. REPORT OF THE NINETEENTH SESSION OF THE INTERGOVERNMENTAL PANEL ON CLIMATE CHANGE (IPCC) Geneva, 17-20 (am only) April 2002.

IPCC, A. 2013. Climate change 2013: the physical science basis. Contribution of working group I to the fifth assessment report of the intergovernmental panel on climate change, 1535.

Jago-On, K. a. B., Kaneko, S., Fujikura, R., Fujiwara, A., Imai, T., Matsumoto, T., Zhang, J., Tanikawa, H., Tanaka, K. & Lee, B. 2009. Urbanization and subsurface environmental issues: An attempt at DPSIR model application in Asian cities. *Science of the total environment,* 407**,** 3089-3104.

Jiang, J., Zhou, T., Chen, X. & Zhang, L. 2020. Future changes in precipitation over Central Asia based on CMIP6 projections. *Environmental Research Letters,* 15**,** 054009.

Jiao, L., Gong, C., Xu, G., Dong, T., Zhang, B. & Li, Z. 2019. Urban expansion dynamics and urban forms in three metropolitan areas—Tokyo, New York, and Shanghai. *Prog. Geogr,* 38**,** 675-685.

Jin, M., Dickinson, R., Shepherd, J., Liang, S., Shepherd, J., Dickinson, R., Vogelmann, A. & Zhang, D. W. Kessomkiat, and G. Pereira, 2011: Satellite-observed urbanization characters in Shanghai, China: Aerosols, urban heat island effect, and land–atmosphere interactions. *Remote Sens,* 3**,** 83-99.

Johnson, H., Kovats, S., Mcgregor, G., Stedman, J., Gibbs, M. & Walton, H. 2005. The

impact of the 2003 heat wave on daily mortality in England and Wales and the use of rapid weekly mortality estimates. *Eurosurveillance,* 10**,** 15-16.

Kain, J. S. 2004. The Kain–Fritsch convective parameterization: an update. *Journal of applied meteorology,* 43**,** 170-181.

Kishtawal, C. M., Niyogi, D., Tewari, M., Pielke Sr, R. A. & Shepherd, J. M. 2010. Urbanization signature in the observed heavy rainfall climatology over India. *International journal of climatology,* 30**,** 1908-1916.

Koomen, E. & Diogo, V. 2017. Assessing potential future urban heat island patterns following climate scenarios, socio-economic developments and spatial planning strategies. *Mitigation and adaptation strategies for global change,* 22**,** 287-306.

Kusaka, H., Hara, M. & Takane, Y. 2012. Urban climate projection by the WRF model at 3-km horizontal grid increment: dynamical downscaling and predicting heat stress in the 2070's August for Tokyo, Osaka, and Nagoya metropolises. *Journal of the Meteorological Society of Japan. Ser. II,* 90**,** 47-63.

Kyle, W. The human bioclimate of Hong Kong. Proceedings of the Contemporary Climatology Conference, Brno. TISK LITERA, Brno, 1994. 350.

Larsen, L. 2015. Urban climate and adaptation strategies. *Frontiers in Ecology and the Environment,* 13**,** 486-492.

Lauwaet, D., De Ridder, K., Saeed, S., Brisson, E., Chatterjee, F., Van Lipzig, N., Maiheu, B. & Hooyberghs, H. 2016. Assessing the current and future urban heat island of Brussels. *Urban Climate,* 15**,** 1-15.

Lee, S. E. & Levermore, G. J. 2013. Simulating urban heat island effects with climate change on a Manchester house. *Building services engineering research and technology,* 34**,** 203-221.

Lee, Y. Y., Din, M. F. M., Ponraj, M., Noor, Z. Z., Iwao, K. & Chelliapan, S. 2017. Overview of urban heat island (uhi) phenomenon towards human thermal comfort. *Environmental Engineering & Management Journal (EEMJ),* 16.

Lelovics, E., Unger, J., Gál, T. & Gál, C. V. 2014. Design of an urban monitoring network based on Local Climate Zone mapping and temperature pattern modelling. *Climate research,* 60**,** 51-62.

Li, H., Zhou, Y., Wang, X., Zhou, X., Zhang, H. & Sodoudi, S. 2019a. Quantifying urban heat island intensity and its physical mechanism using WRF/UCM. *Science of the total environment,* 650**,** 3110-3119.

Li, R., Zhao, L., Ding, Y., Wang, S., Ji, G., Xiao, Y., Liu, G. & Sun, L. 2010. Monthly ratios of PAR to global solar radiation measured at northern Tibetan Plateau, China. *Solar Energy,* 84**,** 964-973.

Li, X. X., Koh, T. Y., Panda, J. & Norford, L. K. 2016. Impact of urbanization patterns on the local climate of a tropical city, Singapore: An ensemble study. *Journal of*

Geophysical Research: Atmospheres, 121**,** 4386-4403.

Li, Y., Zhang, J., Sailor, D. J. & Ban-Weiss, G. A. 2019b. Effects of urbanization on regional meteorology and air quality in Southern California. *Atmospheric Chemistry and Physics,* 19**,** 4439-4457.

Li, Z., Zhou, Y., Wan, B., Chen, Q., Huang, B., Cui, Y. & Chung, H. 2019c. The impact of urbanization on air stagnation: Shenzhen as case study. *Science of the Total Environment,* 664**,** 347-362.

Liang, P. & Ding, Y. 2017. The long-term variation of extreme heavy precipitation and its link to urbanization effects in Shanghai during 1916–2014. *Advances in Atmospheric Sciences,* 34**,** 321-334.

Lin, C.-Y., Chen, W.-C., Liu, S. C., Liou, Y. A., Liu, G. & Lin, T. 2008. Numerical study of the impact of urbanization on the precipitation over Taiwan. *Atmospheric Environment,* 42**,** 2934-2947.

Lin, X., Wang, Y., Wang, S. & Wang, D. 2015. Spatial differences and driving forces of land urbanization in China. *Journal of Geographical Sciences,* 25**,** 545-558.

Lokoshchenko, M. 2014. Urban 'heat island' in Moscow. *Urban Climate,* 10**,** 550-562.

Lokoshchenko, M. A. 2017. Urban heat island and urban dry island in Moscow and their centennial changes. *Journal of Applied Meteorology and Climatology,* 56**,** 2729-2745.

Lowry, W. P. 1977. Empirical estimation of urban effects on climate: a problem analysis. *Journal of Applied Meteorology and Climatology,* 16**,** 129-135.

Luo, J., Pan, L. L., Honomichl, S. B., Bergman, J. W., Randel, W. J., Francis, G., Clerbaux, C., George, M., Liu, X. & Tian, W. 2018. Space–time variability in UTLS chemical distribution in the Asian summer monsoon viewed by limb and nadir satellite sensors. *Atmospheric Chemistry and Physics,* 18**,** 12511-12530.

Madala, S., Salinas, S. V., Wang, J. & Liew, S. C. 2019. Customization of the Advanced Research Weather Research and Forecasting model over the Singapore region: impact of planetary boundary layer schemes, land use, land cover and model horizontal grid resolution. *Meteorological Applications,* 26**,** 221-231.

Mahmoud, S. H. & Gan, T. Y. 2018. Long-term impact of rapid urbanization on urban climate and human thermal comfort in hot-arid environment. *Building and Environment,* 142**,** 83-100.

Marín, J. C., Pozo, D. & Curé, M. 2015. Estimating and forecasting the precipitable water vapor from GOES satellite data at high altitude sites. *Astronomy & Astrophysics,* 573**,** A41.

Masson, V., Lemonsu, A., Hidalgo, J. & Voogt, J. 2020. Urban climates and climate change. *Annual Review of Environment and Resources,* 45**,** 411-444.

Mccarthy, M., Harpham, C., Goodess, C. & Jones, P. 2012. Simulating climate change

in UK cities using a regional climate model, HadRM3. *International Journal of Climatology,* 32**,** 1875-1888.

Mcdonald, R. I., Marcotullio, P. J. & Güneralp, B. 2013. Urbanization and global trends in biodiversity and ecosystem services. *Urbanization, biodiversity and ecosystem services: Challenges and opportunities.* Springer, Dordrecht.

Mlawer, E. J., Taubman, S. J., Brown, P. D., Iacono, M. J. & Clough, S. A. 1997. Radiative transfer for inhomogeneous atmospheres: RRTM, a validated correlated-k model for the longwave. *Journal of Geophysical Research: Atmospheres,* 102**,** 16663-16682.

Morris, K. I., Chan, A., Morris, K. J. K., Ooi, M. C., Oozeer, M. Y., Abakr, Y. A., Nadzir, M. S. M. & Mohammed, I. Y. 2017. Urbanization and urban climate of a tropical conurbation, Klang Valley, Malaysia. *Urban Climate,* 19**,** 54-71.

Morris, K. I., Chan, A., Ooi, M. C., Oozeer, M. Y., Abakr, Y. A. & Morris, K. J. K. 2016a. Effect of vegetation and waterbody on the garden city concept: An evaluation study using a newly developed city, Putrajaya, Malaysia. *Computers, Environment and Urban Systems,* 58**,** 39-51.

Morris, K. I., Chan, A., Salleh, S. A., Ooi, M. C. G., Oozeer, M. Y. & Abakr, Y. A. 2016b. Numerical study on the urbanization of Putrajaya and its interaction with the local climate, over a decade. *Urban Climate,* 16**,** 1-24.

Morris, K. I., Salleh, S. A., Chan, A., Ooi, M. C. G., Abakr, Y. A., Oozeer, M. Y. & Duda, M. 2015. Computational study of urban heat island of Putrajaya, Malaysia. *Sustainable Cities and Society,* 19**,** 359-372.

Murayama, Y., Estoque, R., Hou, H., Gong, H., Simwanda, M., Subasinghe, S. & Zhang, X. 2016. Visualization of land-use/land-cover changes in major Asian and African cities. *Annual Report on the Multi Use Social and Economic Data Bank, University of Tsukuba, Japan.*

Murayama, Y., Estoque, R. C., Subasinghe, S., Hou, H. & Gong, H. 2015. Land-use/land-cover changes in major Asian and African cities. *Annual report on the multi-use social and economy data bank,* 92.

Murayama, Y., Kamusoko, C., Yamashita, A. & Estoque, R. C. 2017. *Urban Development in Asia and Africa*, Springer.

Nations, U. 2014. Probabilistic Population Projections based on the World Population Prospects: The 2012 Revision. *Popul Div Dep Econ Soc Aff.*

NCAR. 2015. "NCAR Command Language (NCL)." UCAR. doi:10.5065/D6WD3XH5.

Ncep, F. 2000. National Centers for Environmental Prediction/National Weather Service/NOAA/US Department of Commerce. 2000, updated daily. NCEP FNL Operational Model Global Tropospheric Analyses, continuing from July 1999. Research Data Archive at the National Center for Atmospheric Research,

Computational and Information Systems Laboratory.

NCEP, and DTC. 2015. "WRF-NMM Users Page | DTC." DTC. http://www.dtcenter.org/wrf-nmm/users/.

Oke, T. & Cleugh, H. GT Johnson, DG Steyn, and ID Watson, 1991: Simulation of surface urban heat islands under 'ideal'conditions at night. Part 2: Diagnosis of causation. *Bound.-Layer Meteor,* 56**,** 339-358.

Oke, T. R. 1981. Canyon geometry and the nocturnal urban heat island: comparison of scale model and field observations. *Journal of climatology,* 1**,** 237-254.

Oke, T. R. 1982. The energetic basis of the urban heat island. *Quarterly Journal of the Royal Meteorological Society,* 108**,** 1-24.

Oke, T. R. 1984. Towards a prescription for the greater use of climatic principles in settlement planning. *Energy and buildings,* 7**,** 1-10.

Oke, T. R. 2002. *Boundary layer climates*, Routledge.

Oleson, K. 2012. Contrasts between urban and rural climate in CCSM4 CMIP5 climate change scenarios. *Journal of Climate,* 25**,** 1390-1412.

Onyango, A. O. 2018. Global and regional trends of urbanization: A critical review of the environmental and economic imprints. *World Environment,* 8**,** 47-62.

Organization, W. H. 2016. Ambient air pollution: A global assessment of exposure and burden of disease.

Pachauri, R. & Meyer, L. 2014. Climate Change 2014: Synthesis Report. Contribution of Working Groups I, II and III to the Fifth Assessment Report of the Intergovernmental Panel on Climate Change.

Pachauri, R. K. & Reisinger, A. 2008. Climate change 2007. Synthesis report. Contribution of Working Groups I, II and III to the fourth assessment report.

Papangelis, G., Tombrou, M., Dandou, A. & Kontos, T. 2012. An urban "green planning" approach utilizing the Weather Research and Forecasting (WRF) modeling system. A case study of Athens, Greece. *Landscape and urban planning,* 105**,** 174-183.

Pataki, D., Xu, T., Luo, Y. Q. & Ehleringer, J. R. 2007. Inferring biogenic and anthropogenic carbon dioxide sources across an urban to rural gradient. *Oecologia,* 152**,** 307-322.

Peng, S., Piao, S., Ciais, P., Friedlingstein, P., Ottle, C., Bréon, F.-M., Nan, H., Zhou, L. & Myneni, R. B. 2012. Surface urban heat island across 419 global big cities. *Environmental science & technology,* 46**,** 696-703.

Peng, Z., Wang, Q., Kan, H., Chen, R. & Wang, W. 2017. Effects of ambient temperature on daily hospital admissions for mental disorders in Shanghai, China: a time-series analysis. *Science of the Total Environment,* 590**,** 281-286.

163

Philandras, C., Metaxas, D. & Nastos, P. T. 1999. Climate variability and urbanization in Athens. *Theoretical and applied climatology,* 63**,** 65-72.

Qiao, Z., Tian, G., Zhang, L. & Xu, X. 2014. Influences of urban expansion on urban heat island in Beijing during 1989–2010. *Advances in Meteorology,* 2014.

Ren, C., Cai, M., Li, X., Zhang, L., Wang, R., Xu, Y. & Ng, E. 2019. Assessment of local climate zone classification maps of cities in China and feasible refinements. *Scientific reports,* 9**,** 1-11.

Ren, G.-Y. 2017. Urbanization as a major driver of urban climate change. *Advances in Climate Change Research*.

Ren, W., Zhong, Y., Meligrana, J., Anderson, B., Watt, W. E., Chen, J. & Leung, H.-L. 2003. Urbanization, land use, and water quality in Shanghai: 1947–1996. *Environment international,* 29**,** 649-659.

Robaa, E.-S. 2011. Effect of urbanization and industrialization processes on outdoor thermal human comfort in Egypt. *Atmospheric and Climate Sciences,* 1**,** 100.

Rohm, W., Guzikowski, J., Wilgan, K. & Kryza, M. 2019. 4DVAR assimilation of GNSS zenith path delays and precipitable water into a numerical weather prediction model WRF. *Atmospheric Measurement Techniques,* 12**,** 345-361.

Romero, H., Ihl, M., Rivera, A., Zalazar, P. & Azocar, P. 1999. Rapid urban growth, land-use changes and air pollution in Santiago, Chile. *Atmospheric Environment,* 33**,** 4039-4047.

Rossberg, A. 2008. Part–whole relations between food webs and the validity of local food-web descriptions. *ecological complexity,* 5**,** 121-131.

Sailor, D. J. 2011. A review of methods for estimating anthropogenic heat and moisture emissions in the urban environment. *International journal of climatology,* 31**,** 189-199.

Samsonov, T. E., Konstantinov, P. I. & Varentsov, M. I. 2015. Object-oriented approach to urban canyon analysis and its applications in meteorological modeling. *Urban Climate,* 13**,** 122-139.

Schwartz, M., Heimiller, D., Haymes, S. & Musial, W. 2010. Assessment of offshore wind energy resources for the United States. National Renewable Energy Lab.(NREL), Golden, CO (United States).

Shahmohamadi, P., Che-Ani, A., Maulud, K., Tawil, N. & Abdullah, N. 2011. The impact of anthropogenic heat on formation of urban heat island and energy consumption balance. *Urban Studies Research,* 2011.

Shanghai Municipal People's Government. 2020. 2020 Shanghai Statistical Year Book [Online]. Available: http://tjj.sh.gov.cn/tjnj/zgsh/tjnj2020en.html [Accessed].

Shanghai Statistics Bureau. 2018. Statistical Yearbook of Shanghai,2018, China Statistical Press.

Shanghai Statistics Bureau. 2019. Statistical Yearbook of Shanghai,2019, China Statistical Press.

Shanghai Statistics Bureau. 2020. Statistical Yearbook of Shanghai,2020, China Statistical Press.

Shem, W. & Shepherd, M. 2009. On the impact of urbanization on summertime thunderstorms in Atlanta: Two numerical model case studies. *Atmospheric Research,* 92**,** 172-189.

Shen, L., Wang, H., Zhu, B., Zhao, T., Liu, A., Lu, W., Kang, H. & Wang, Y. 2021. Impact of urbanization on air quality in the Yangtze River Delta during the COVID-19 lockdown in China. *Journal of Cleaner Production,* 296**,** 126561.

Shi, P., Bai, X., Kong, F., Fang, J., Gong, D., Zhou, T., Guo, Y., Liu, Y., Dong, W. & Wei, Z. 2017. Urbanization and air quality as major drivers of altered spatiotemporal patterns of heavy rainfall in China. *Landscape Ecology,* 32**,** 1723-1738.

Shimadera, H., Kondo, A., Shrestha, K. L., Kitaoka, K. & Inoue, Y. 2015. Numerical evaluation of the impact of urbanization on summertime precipitation in Osaka, Japan. *Advances in Meteorology,* 2015.

Shukla, P. R., Skeg, J., Buendia, E. C., Masson-Delmotte, V., Pörtner, H.-O., Roberts, D., Zhai, P., Slade, R., Connors, S. & Van Diemen, S. 2019. Climate Change and Land: an IPCC special report on climate change, desertification, land degradation, sustainable land management, food security, and greenhouse gas fluxes in terrestrial ecosystems.

Skamarock, W. C., Klemp, J. B., Dudhia, J., Gill, D. O., Barker, D. M., Wang, W. & Powers, J. G. 2008. A description of the Advanced Research WRF version 3. NCAR Technical note-475+ STR.

Solecki, W. & Marcotullio, P. J. 2013. Climate change and urban biodiversity vulnerability. *Urbanization, biodiversity and ecosystem services: Challenges and opportunities.* Springer, Dordrecht.

Song, C. & Wu, J. 2013. Junxiang Li, Cheng Li, Feige Zhu. *Landscape Ecol,* 28**,** 1545-1565.

Souch, C. & Grimmond, S. 2006. Applied climatology: urban climate. *Progress in physical geography,* 30**,** 270-279.

Stewart, I. D. 2011. A systematic review and scientific critique of methodology in modern urban heat island literature. *International Journal of Climatology,* 31**,** 200-217.

Stocker, T. F., Qin, D., Plattner, G.-K., Tignor, M. M., Allen, S. K., Boschung, J., Nauels, A., Xia, Y., Bex, V. & Midgley, P. M. 2014. Climate Change 2013: The physical science basis. contribution of working group I to the fifth assessment report of IPCC the intergovernmental panel on climate change.

Stone Jr, B., Vargo, J., Liu, P., Habeeb, D., Delucia, A., Trail, M., Hu, Y. & Russell, A. 2014. Avoided heat-related mortality through climate adaptation strategies in three US cities. *PloS one,* 9**,** e100852.

Svirejeva-Hopkins, A., Schellnhuber, H. J. & Pomaz, V. L. 2004. Urbanised territories as a specific component of the Global Carbon Cycle. *Ecological Modelling,* 173**,** 295-312.

Takebayashi, H. & Moriyama, M. 2007. Surface heat budget on green roof and high reflection roof for mitigation of urban heat island. *Building and environment,* 42**,** 2971-2979.

Takebayashi, H. & Moriyama, M. 2009. Study on the urban heat island mitigation effect achieved by converting to grass-covered parking. *Solar Energy,* 83**,** 1211-1223.

Takebayashi, H. & Moriyama, M. 2012. Study on surface heat budget of various pavements for urban heat island mitigation. *Advances in Materials Science and Engineering,* 2012.

Tan, J. & Grimmond, S. 2016. Shanghai's Urban Integrated Meteorological Observation Network (SUIMON): Some Case Studies of Applications. *한국기상학회 학술대회 논문집***,** 390-392.

Tan, J., Zheng, Y., Tang, X., Guo, C., Li, L., Song, G., Zhen, X., Yuan, D., Kalkstein, A. J. & Li, F. 2010. The urban heat island and its impact on heat waves and human health in Shanghai. *International journal of biometeorology,* 54**,** 75-84.

Tecer, L. H. & Tagil, S. 2014. Impact of urbanization on local air quality: differences in urban and rural areas of Balikesir, Turkey. *CLEAN–Soil, Air, Water,* 42**,** 1489-1499.

Tewari, M., Chen, F., Kusaka, H. & Miao, S. 2007. Coupled WRF/Unified Noah/urban-canopy modeling system. *Ncar WRF Documentation, NCAR, Boulder.* Citeseer.

Thompson, H. L. 2009. *Modelling the impact of urbanization on the regional climate of the Greater London area.* University of Birmingham.

United Nations, 2014. Trends in urbanization. https://doi.org/10.18356/7053dedb-en

United Nations, D., 2014. World urbanization Prospects, the 2011 revision. Popul. Div. Dep. Econ. Soc. Aff. United Nations Secr.

United Nations, D., 2019. World Urbanization Prospects: The 2018 Revision, World Urbanization Prospects: The 2018 Revision. New York.

Wang, C., Chen, R., Kuang, X., Duan, X. & Kan, H. 2014. Temperature and daily mortality in Suzhou, China: a time series analysis. *Science of the Total Environment,* 466**,** 985-990.

Wang, J., Da, L., Song, K. & Li, B.-L. 2008. Temporal variations of surface water quality in urban, suburban and rural areas during rapid urbanization in Shanghai,

China. *Environmental Pollution,* 152**,** 387-393.

Wang, S., Gao, S., Li, S. & Feng, K. 2020. Strategizing the relation between urbanization and air pollution: Empirical evidence from global countries. *Journal of Cleaner Production,* 243**,** 118615.

Wilby, R. L. 2003. Past and projected trends in London's urban heat island. *Weather,* 58**,** 251-260.

Wilby, R. L. 2008. Constructing climate change scenarios of urban heat island intensity and air quality. *Environment and planning B: Planning and Design,* 35**,** 902-919.

Xia, T.-Y., Wang, J.-Y., Song, K. & Da, L.-J. 2014. Variations in air quality during rapid urbanization in Shanghai, China. *Landscape and ecological engineering,* 10**,** 181-190.

Xiao, S., Dong, H., Geng, Y., Francisco, M.-J., Pan, H. & Wu, F. 2020. An overview of the municipal solid waste management modes and innovations in Shanghai, China. *Environmental Science and Pollution Research,* 27**,** 29943-29953.

Yang, B., Yang, X., Leung, L. R., Zhong, S., Qian, Y., Zhao, C., Chen, F., Zhang, Y. & Qi, J. 2019. Modeling the impacts of urbanization on summer thermal comfort: the role of urban land use and anthropogenic heat. *Journal of Geophysical Research: Atmospheres,* 124**,** 6681-6697.

Yang, L., Niyogi, D., Tewari, M., Aliaga, D., Chen, F., Tian, F. & Ni, G. 2016. Contrasting impacts of urban forms on the future thermal environment: example of Beijing metropolitan area. *Environmental Research Letters,* 11**,** 034018.

Yang, X. L., Yang, Q. Q., Ding, J. J., Xu, Y. P. & Zhou, Y. K. Effect of Urbanization on Regional Precipitation in the Qinhuai River Area, East China. Applied Mechanics and Materials, 2012. Trans Tech Publ, 2481-2489.

Zhang, K., Wang, R., Shen, C. & Da, L. 2010. Temporal and spatial characteristics of the urban heat island during rapid urbanization in Shanghai, China. *Environmental monitoring and assessment,* 169**,** 101-112.

Zhang, K. H. & Shunfeng, S. 2003. Rural–urban migration and urbanization in China: Evidence from time-series and cross-section analyses. *China Economic Review,* 14**,** 386-400.

Zhao, M., Cai, H., Qiao, Z. & Xu, X. 2016. Influence of urban expansion on the urban heat island effect in Shanghai. *International Journal of Geographical Information Science,* 30**,** 2421-2441.

Zhou, C., Chen, J. & Wang, S. 2018. Examining the effects of socioeconomic development on fine particulate matter (PM2. 5) in China's cities using spatial regression and the geographical detector technique. *Science of the Total Environment,* 619**,** 436-445.

Zhou, S. & Wu, L. 1987. Underlying surface temperature of Shanghai and urban heat island. *Acta Scientiae Circumstantiae,* 7**,** 261-267.

Zhou, S. & Zhang, C. 1982. On the Shanghai urban heat island effect. *Acta Geographica Sinica,* 37**,** 372-381.

9 Appendix

Appendix 1. Some sections of the namelist.wps

```
&share
 wrf_core = 'ARW',
 max_dom = 3,
 start_date = '2017-07-21_00:00:00','2017-07-21_00:00:00','2017-07-21_00:00:00',
 end_date   = '2017-08-05_24:00:00','2017-08-05_24:00:00','2017-08-05_24:00:00',
 interval_seconds = 21600,
 io_form_geogrid = 2,
/

&geogrid
 parent_id         = 1,1,2,
 parent_grid_ratio = 1,3,3,
 i_parent_start    = 1,45,42,
 j_parent_start    = 1,45,42,
 e_we        = 128,118,106,
 e_sn        = 128,118,106,
 !
 !!!!!!!!!!!!!!!!!!!!!!!!!!!!! IMPORTANT NOTE !!!!!!!!!!!!!!!!!!!!!!!!!!!!!!
 ! The default datasets used to produce the HGT_M, GREENFRAC,
 ! and LU_INDEX/LANDUSEF fields have changed in WPS v3.8. The HGT_M field
 ! is now interpolated from 30-arc-second USGS GMTED2010, the GREENFRAC
 ! field is interpolated from MODIS FPAR, and the LU_INDEX/LANDUSEF fields
 ! are interpolated from 21-class MODIS.
 !
 ! To match the output given by the default namelist.wps in WPS v3.7.1,
 ! the following setting for geog_data_res may be used:
 !
 ! geog_data_res = 'gtopo_10m+usgs_10m+nesdis_greenfrac+10m','gtopo_2m+usgs_2m+nesdis_greenfrac+2m',
 !
 !!!!!!!!!!!!!!!!!!!!!!!!!!!!! IMPORTANT NOTE !!!!!!!!!!!!!!!!!!!!!!!!!!!!!!
 !
 geog_data_res = 'ld_33+default','ld_33+default','ld_33',,
 dx = 0.08333,
 dy = 0.08333,
 map_proj =  'lat-lon',
 ref_lat   = 31.206,
 ref_lon   = 121.437,
 truelat1  = 31.206,
 truelat2  = 31.206,
 stand_lon = 121.437,
```

Appendix 2. Some sections of the namelist.input

```
&time_control
run_days                = 15,
run_hours                = 0,
run_minutes               = 0,
run_seconds               = 0,
start_year              = 2017,   2017,   2017,
start_month              = 07,     07,     07,
start_day               = 21,     21,     21,
start_hour              = 00,     00,     00,
start_minute             = 00,     00,     00,
start_second             = 00,     00,     00,
end_year                = 2017,   2017,   2017,
end_month                = 08,     08,     08,
end_day                 = 05,     05,     05,
end_hour                = 24,     24,     24,
end_minute               = 00,     00,     00,
end_second               = 00,     00,     00,
interval_seconds          = 21600
input_from_file           = .true.,  .true.,  .true.,
history_interval         = 180,    60,     60,
frames_per_outfile        = 1000,   1000,   1000,
restart              = .false.,
restart_interval          = 5000,
io_form_history          = 2
io_form_restart          = 2
io_form_input            = 2
io_form_boundary          = 2
debug_level              = 0
/

&domains
time_step               = 30,
time_step_fract_num         = 0,
time_step_fract_den         = 1,
max_dom                 = 3,

e_we                 = 128,   118,  106,

e_sn                 = 128,   118,  106,

e_vert                = 34,  34,   34
eta_levels               = 1.000,  0.991,
                      0.990,  0.988 , 0.987,  0.984,  0.981,
                      0.972,  0.963 , 0.941,  0.916,  0.898,
                      0.868,  0.836,  0.802,  0.766,  0.729,
                      0.6915, 0.5536, 0.5153, 0.4773,0.454,
                      0.404,  0.3695, 0.3375, 0.3085,0.2845,
                      0.2645, 0.2465, 0.2305, 0.2165, 0.2035,
                      0.1000, 0.000,

p_top_requested           = 5000,
num_metgrid_levels          = 32,
num_metgrid_soil_levels        = 4,
dx                      = 9264.419, 3088.140,  1029.380,
dy                   = 9264.419, 3088.140, 1029.380,
grid_id               = 1,     2,     3,
parent_id              = 1,     1,     2,
i_parent_start             = 1,     45,     42,
j_parent_start            = 1,     45,     42,
parent_grid_ratio           = 1,     3,     3,
parent_time_step_ratio         = 1,     3,     3,
feedback              = 1,
smooth_option              = 0
```

Appendix 3. Some sections of the GEOGRID.TBL

```
name = HGT_M
    priority = 1
    dest_type = continuous
    smooth_option = smth-desmth_special; smooth_passes=1
    fill_missing=0.
    interp_option = gmted2010_30s:average_gcell(4.0)+four_pt+average_4pt
    interp_option =     gtopo_30s:average_gcell(4.0)+four_pt+average_4pt
    interp_option =      gtopo_2m:four_pt
    interp_option =      gtopo_5m:four_pt
    interp_option =     gtopo_10m:four_pt
    interp_option =       lowres:average_gcell(4.0)+four_pt
    interp_option =      default:average_gcell(4.0)+four_pt+average_4pt
    rel_path = gmted2010_30s:topo_gmted2010_30s/
    rel_path =     gtopo_30s:topo_30s/
    rel_path =      gtopo_2m:topo_2m/
    rel_path =      gtopo_5m:topo_5m/
    rel_path =     gtopo_10m:topo_10m/
    rel_path =       lowres:topo_gmted2010_5m/
    rel_path =      default:topo_gmted2010_30s/
===============================
name=LANDUSEF
    priority=1
    dest_type=categorical
    z_dim_name=land_cat
    dominant = LU_INDEX
    landmask_water =    nlcd2006_9s:17      # Calculate a landmask from this field
    landmask_water =   nlcd2006_30s:17       # Calculate a landmask from this field
    landmask_water =    nlcd2011_9s:17      # Calculate a landmask from this field
    landmask_water =       nlcd2006:17     # Calculate a landmask from this field
    landmask_water =       ssib_10m:16     # Calculate a landmask from this field
    landmask_water =        ssib_5m:16    # Calculate a landmask from this field
    landmask_water =      modis_15s:17     # Calculate a landmask from this field
    landmask_water = modis_15s_lake:17       # Calculate a landmask from this field
    landmask_water =      modis_30s:17    # Calculate a landmask from this field
    landmask_water = modis_30s_lake:17,21      # Calculate a landmask from this field
    landmask_water =       usgs_30s:16    # Calculate a landmask from this field
    landmask_water =     usgs_lakes:16,28   # Calculate a landmask from this field
    landmask_water =    modis_lakes:17,21    # Calculate a landmask from this field
    landmask_water =       usgs_2m:16    # Calculate a landmask from this field
    landmask_water =       usgs_5m:16    # Calculate a landmask from this field
    landmask_water =      usgs_10m:16     # Calculate a landmask from this field
    landmask_water =        lowres:17,21   # Calculate a landmask from this field
    landmask_water =       default:17,21   # Calculate a landmask from this field
```

Appendix 4. Sample of Vtable file used in this research

```
GRIB1| Level| From | To | metgrid  | metgrid | metgrid            |GRIB2|GRIB2|GRIB2|GRIB2|
Param| Type |Level1|Level2| Name   | Units   | Description        |Discp|Catgy|Param|Level|
-----+-----+----+-----+-------+------+---------------------------+-----------------+
 11 | 100 |  *  |     | TT    | K    | Temperature              | 0 | 0 | 0 | 100 |
 33 | 100 |  *  |     | UU    | m s-1 | U                       | 0 | 2 | 2 | 100 |
 34 | 100 |  *  |     | VV    | m s-1 | V                       | 0 | 2 | 3 | 100 |
 52 | 100 |  *  |     | RH    | %    | Relative Humidity        | 0 | 1 | 1 | 100 |
  7 | 100 |  *  |     | HGT   | m    | Height                   | 0 | 3 | 5 | 100 |
 11 | 105 |  2  |     | TT    | K    | Temperature      at 2 m  | 0 | 0 | 0 | 103 |
 52 | 105 |  2  |     | RH    | %    | Relative Humidity at 2 m | 0 | 1 | 1 | 103 |
 33 | 105 | 10  |     | UU    | m s-1 | U            at 10 m    | 0 | 2 | 2 | 103 |
 34 | 105 | 10  |     | VV    | m s-1 | V            at 10 m    | 0 | 2 | 3 | 103 |
  1 |  1  |  0  |     | PSFC  | Pa   | Surface Pressure         | 0 | 3 | 0 | 1|
  2 | 102 |  0  |     | PMSL  | Pa   | Sea-level Pressure       | 0 | 3 | 1 | 101 |
144 | 112 |  0  | 10  | SM000010 | fraction| Soil Moist 0-10 cm below grn layer (Up) | 2 | 0 | 192 | 106 |
144 | 112 | 10  | 40  | SM010040 | fraction| Soil Moist 10-40 cm below grn layer   | 2 | 0 | 192 | 106 |
144 | 112 | 40  | 100 | SM040100 | fraction| Soil Moist 40-100 cm below grn layer  | 2 | 0 | 192 | 106 |
144 | 112 | 100 | 200 | SM100200 | fraction| Soil Moist 100-200 cm below gr layer  | 2 | 0 | 192 | 106 |
144 | 112 | 10  | 200 | SM010200 | fraction| Soil Moist 10-200 cm below gr layer   | 2 | 0 | 192 | 106 |
 11 | 112 |  0  | 10  | ST000010 | K    | T 0-10 cm below ground layer (Upper)  | 0 | 0 | 0 | 106 |
 11 | 112 | 10  | 40  | ST010040 | K    | T 10-40 cm below ground layer (Upper) | 0 | 0 | 0 | 106 |
 11 | 112 | 40  | 100 | ST040100 | K    | T 40-100 cm below ground layer (Upper)| 0 | 0 | 0 | 106 |
 11 | 112 | 100 | 200 | ST100200 | K    | T 100-200 cm below ground layer (Bottom)| 0 | 0 | 0 | 106 |
 11 | 112 | 10  | 200 | ST010200 | K    | T 10-200 cm below ground layer (Bottom) | 0 | 0 | 0 | 106 |
 91 |  1  |  0  |     | SEAICE  | proprtn | Ice flag                   | 10 | 2 | 0 | 1 |
 81 |  1  |  0  |     | LANDSEA | proprtn | Land/Sea flag (1=land, 0 or 2=sea) | 2 | 0 | 0 | 1 |
  7 |  1  |  0  |     | SOILHGT | m    | Terrain field of source analysis   | 0 | 3 | 5 | 1 |
 11 |  1  |  0  |     | SKINTEMP | K   | Skin temperature (can use for SST also)| 0 | 0 | 0 | 1 |
 65 |  1  |  0  |     | SNOW   | kg m-2 | Water equivalent snow depth      | 0 | 1 | 13 | 1 |
    |  1  |  0  |     | SNOWH  | m    | Physical Snow Depth              | 0 | 1 |   | 1 |
-----+-----+----+-----+-------+------+---------------------------+-----------------+
#
# For SNOWH, NCEP starts with the AFWA snow depth analysis and converts it to a water-equivalent.
# For some reason, NCEP uses a different ratio in the GFS/GDAS than in the NAM and that which is assumed in WRF.
# Therefore, we need to adjust SNOW and compute SNOWH in ungrib.
```

Appendix 5. Sample of ncl scipt to output averaged results

```
load "$NCARG_ROOT/lib/ncarg/nclscripts/csm/gsn_code.ncl"      ; These two libraries are automatically
load "$NCARG_ROOT/lib/ncarg/nclscripts/wrf/WRFUserARW.ncl"    ; loaded from NCL V6.4.0 onward.
begin

 ; 1) Step-0  Setteings
 filename = "d03.nc"
 FillValue = -999.0
 Mask_need          = (/12,31,32/)  ;

 ; 2) Step-1  get data from wrfout        uvmet10_wspd_wdir
 f                  = addfile(filename,"r")
 T2                 = wrf_user_getvar(f,"T2",-1)
 RH2                = wrf_user_getvar(f,"rh2",-1)
 Wind               = wrf_user_getvar(f,"uvmet10_wspd_wdir",-1)
 Mask               = wrf_user_getvar(f,"LU_INDEX",-1)
 Times              = wrf_user_getvar(f,"times",-1)
 dims               = dimsizes(T2)

 ; 3) Step-2  process_data
 Wspd                      = Wind(0,:,:,:)
 T2@_FillValue     = FillValue
 RH2@_FillValue    = FillValue
 Wspd@_FillValue   = FillValue
 T2_need           = T2
 RH2_need                  = RH2
 Wspd_need                 = Wspd
 T2_need_ave               = new((/dimsizes(Mask_need),dims(0)/),"float")
 RH2_need_ave              = new((/dimsizes(Mask_need),dims(0)/),"float")
 Wspd_need_ave             = new((/dimsizes(Mask_need),dims(0)/),"float")
 T2_need_ave1   = new((/dimsizes(Mask_need),dims(0)/),"float")
 RH2_need_ave1  = new((/dimsizes(Mask_need),dims(0)/),"float")
 Wspd_need_ave1 = new((/dimsizes(Mask_need),dims(0)/),"float")

 ; Loop for Mask_need
 do i = 0,dimsizes(Mask_need)-1
   T2_need                 = where(Mask.eq.Mask_need(i),T2,T2@_FillValue)
   RH2_need                = where(Mask.eq.Mask_need(i),RH2,RH2@_FillValue)
   Wspd_need               = where(Mask.eq.Mask_need(i),Wspd,Wspd@_FillValue)
   ; Loop for time
   do j = 28, 75
     T2_need_ave(i,j-28)        =avg(T2_need(j,:,:)) - 273.15
     RH2_need_ave(i,j-28)       =avg(RH2_need(j,:,:))
     Wspd_need_ave(i,j-28)      =avg(Wspd_need(j,:,:))
   end do

   do q = 0, 23
     T2_need_ave1(i,q) = (T2_need_ave(i,q)+T2_need_ave(i,q+24))/2
     RH2_need_ave1(i,q) = (RH2_need_ave(i,q)+RH2_need_ave(i,q+24))/2
     Wspd_need_ave1(i,q) = (Wspd_need_ave(i,q)+Wspd_need_ave(i,q+24))/2
   end do

 ; Output
  csvname = "LU_Index_"+Mask_need(i)+".csv"
  system("rm -rf " + csvname)
  write_table(csvname,"w",[/Times(:),T2_need_ave1(i,:),RH2_need_ave1(i,:),Wspd_need_ave1(i,:)/],"%s,%5f,%5f,%5f")
 end do
end
```